
The Crystal Zero Degree Detector at BESIII as a Realistic High Rate Environment for Evaluating PANDA Data Acquisition Modules

Inaugural-Dissertation
zur Erlangung des Doktorgrades der Naturwissenschaften
der Justus-Liebig-Universität Gießen im Fachbereich 07
(Mathematik und Informatik, Physik, Geographie)

vorgelegt von

MARCEL WERNER

aus Eschenburg

II. Physikalisches Institut
der Justus-Liebig-Universität Gießen
im März 2015

Dekan: Prof. Dr. Peter Jens Klar
1. Berichterstatter: Prof. Dr. Wolfgang Kühn
2. Berichterstatter: Prof. Dr. Alfred Müller

*Jesus bleibet meine Freude,
Meines Herzens Trost und Saft,
Jesus wehret allem Leide,
Er ist meines Lebens Kraft,*

*Meiner Augen Lust und Sonne,
Meiner Seele Schatz und Wonne;
Darum lass ich Jesum nicht
Aus dem Herzen und Gesicht.*

Johann Sebastian Bach

(1685 - 1750)

aus der Kantate

“Herz und Mund und Tat und Leben”

(BWV 147)

*Für meine Eltern, meine Frau
und meine Kinder*

ABSTRACT

The BESIII experiment located in Beijing, China, is investigating physics in the energy region of the charm-quark via electron positron annihilation reactions. A small detector to be placed in the very forward/backward region around $\theta = 0^\circ$ at BESIII is foreseen to measure photons from the initial state. This is especially interesting, because it opens the door for various physics measurements over a wide range of energies, even below the experiment's designated energy threshold, which is fixed by the accelerator.

This thesis is investigating the capabilities of a crystal zero degree detector (cZDD) consisting of PbWO_4 crystals placed in that region of BESIII. Detailed Geant4-based simulations have been performed and the energy resolution of the detector has been determined to be $\sigma/\mu = 0.06 \oplus 0.025/\sqrt{E[\text{GeV}]}$.

The determination of the center-of-mass energy \sqrt{s}_{ISR} after the emission of the photon is of great importance for the study of such events. Preliminary simulations estimated the resolution of the reconstructed \sqrt{s}_{ISR} using the cZDD information to be significantly better than 10 % for appropriate photon impacts on the detector. Such events can only be investigated, when data from the cZDD and other detectors of BESIII can be correlated. A fast and powerful Data Acquisition (DAQ) capable of performing event correlation in real time is needed. DAQ modules capable of performing real time event correlation are being developed for the $\bar{\text{P}}\text{ANDA}$ experiment at the future FAIR facility in Darmstadt, Germany. Investigating these modules in a realistic high-rate environment such as provided at BESIII, offers a great opportunity to gain experience in real time event correlation before the start of $\bar{\text{P}}\text{ANDA}$. Developments for the cZDD's DAQ using prototype $\bar{\text{P}}\text{ANDA}$ DAQ modules have been done and successfully tested in experiments with radioactive sources and a beamtest with 210 MeV electrons at the Mainz Microtron.

CONTENTS

1. Introduction and Physics Motivation	1
2. $\bar{\text{P}}\text{ANDA}$ and BESIII	7
2.1. The $\bar{\text{P}}\text{ANDA}$ Project at FAIR	7
2.1.1. The $\bar{\text{P}}\text{ANDA}$ Detector	8
2.1.2. The $\bar{\text{P}}\text{ANDA}$ Readout Concept	15
2.2. The BESIII Experiment	16
2.2.1. The BESIII Detector	17
2.3. The Physics Program of BESIII and $\bar{\text{P}}\text{ANDA}$	20
2.3.1. Charmonium Spectroscopy	20
2.3.2. Open Charm Physics	23
2.3.3. Hybrids, Glueballs, and other Exotics	23
2.3.4. Hadrons in the Nuclear Medium	23
2.3.5. Hypernuclei	24
3. The Physics Of Initial State Radiation	27
3.1. ISR Physics and Its Applications	28
3.2. ISR Physics at BESIII	32
4. Zero Degree Calorimetry at BESIII	35
4.1. Spacial Considerations	35
4.2. The Zero Degree Detector (ZDD)	36
4.3. The Crystal Zero Degree Detector (cZDD)	37
4.3.1. PbWO_4 crystals	40
4.3.2. Silicon Photomultipliers	40
4.3.2.1. General Principle	40

4.3.2.2.	Properties	41
4.3.2.3.	Specific Properties of Hamamatsu S10931-050P MPPCs	44
4.3.2.4.	MPPC Preamplifier and Prototype Mechanics	45
4.3.3.	Foreseen cZDD DAQ scheme	46
5.	Simulations of the Crystal Zero Degree Detector	47
5.1.	Physics of Electromagnetic Showers	47
5.2.	Geant4-based Simulations of the cZDD	49
5.2.1.	The BESIII Offline Software System (BOSS)	49
5.2.2.	Implementation of the cZDD into BOSS	50
5.2.3.	Energy Resolution	56
5.2.4.	Position Reconstruction	58
5.2.5.	Determination of \sqrt{s}_{ISR}	63
5.3.	Conclusion	72
6.	Related DAQ Developments	73
6.1.	MPPC Coincidence Board	74
6.2.	The sampling ADC (sADC) Prototype	76
6.2.1.	ADC Linearity	77
6.3.	The Compute Node (CN)	79
6.3.1.	Workflow On The CN	80
6.3.2.	Event Builder	80
6.4.	PC-based Data Analysis	82
7.	Test Experiments and Results	85
7.1.	Tests with Radioactive Sources	85
7.1.1.	Properties of LYSO	86
7.1.2.	Experimental Setup	87
7.1.3.	Energy Calibration with ^{22}Na	89
7.1.4.	Measurements of ^{60}Co and ^{176}Lu	90
7.2.	Beamtest at MAMI	93
7.2.1.	The Prototype Detector	93
7.2.2.	The Mainz Microtron	93
7.2.3.	Geant4 Simulations	95
7.2.4.	Energy Resolution Measurements	97
7.2.5.	Measurements at Different Rates	104
7.3.	Conclusion	106
8.	Summary, Discussion and Perspectives	107
9.	Deutsche Zusammenfassung	111

A. Appendix - Simulation	115
A.1. Crystal Numbering Scheme	115
A.2. BesZddHits	115
A.3. BesZddDigis	116
A.4. cZDD Identifier	117
A.5. Fits and Parameters	118
A.5.1. Single Pixel Signals	118
A.5.2. Correlation of Charge Channel and Energy Deposition	119
A.5.3. cZDD Resolution Fits	120
A.6. \sqrt{s}_{ISR} Determination	123
B. Appendix - DAQ	127
B.1. Data Format	127
C. Appendix - Experiments	129
C.1. Radioactive Sources	129
C.1.1. Fit Functions and Parameters	129
C.2. Beamtest	131
C.2.1. Fit Parameters	131
References	141
Danksagungen	143
Eidesstattliche Versicherung	145

INTRODUCTION AND PHYSICS MOTIVATION

On the 4th of July 2012 an important announcement at CERN aroused interest around the world: A particle consistent with the long time predicted, but until then not found Higgs particle has finally been seen by both the ATLAS and CMS experiments [1, 2]. Half a year later on the 4th of March 2013 it became certainty: scientists at CERN confirmed that this particle is indeed a Higgs boson [3]. This discovery fills a very important gap in the Standard Model of particle physics (SM), a theory, which successfully describes many aspects of nature in terms of its smallest constituents, namely quarks, leptons and the gauge bosons (Fig. 1.1). Besides the general conservation laws of physics (conservation of energy, momentum, angular momentum and charge), it is based on two additional conservation laws: the conservation of baryon number \mathcal{B} and the conservation of lepton number l . \mathcal{B} is the sum of all baryons and antibaryons of the initial state, where baryons like the proton or the neutron have $\mathcal{B} = 1$, whereas antibaryons (e.g. antiproton) have $\mathcal{B} = -1$. Mesons or leptons carry baryon number zero. The conservation of lepton number follows the same principle for leptons and antileptons, respectively.

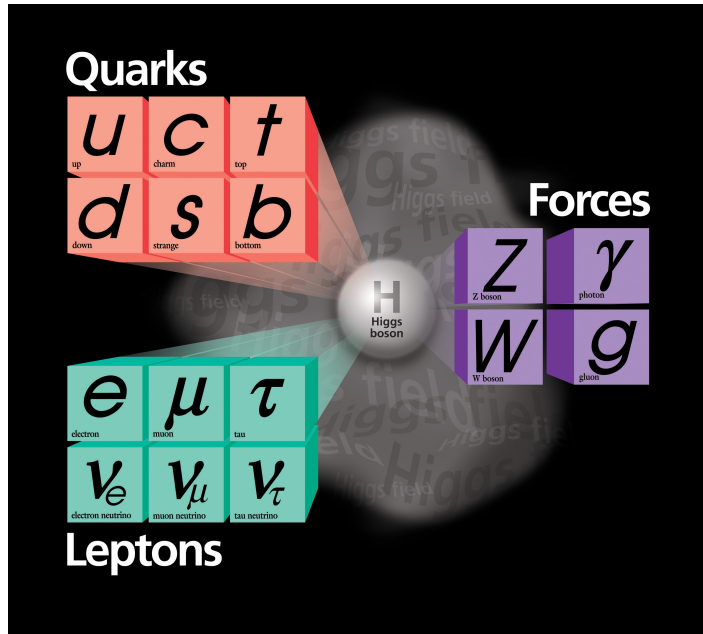


Fig. 1.1.: The Standard Model of particle physics with its three generations of matter [4]. The Higgs-field interacting with the massive particles is also shown. Since the discovery of neutrino oscillations, we know that neutrinos must have a mass unequal zero, but their coupling to the Higgs field is so weak, that one was not able to measure it yet.

The SM has shown a remarkable predictive power, which led to the discovery of many particles, including the Higgs boson itself. The Higgs mechanism is vital for the SM, since it presents the only way to introduce massive particles into a massless theory: According to this Higgs mechanism, the whole space is filled with a *Higgs field*, mediated by the Higgs boson, and by interacting with this field, quarks, leptons and the heavy W^\pm and Z bosons gain their masses. In recognition of their remarkable mass-generating mechanism [5–7], the nobel prize 2013 was awarded to François Englert and Peter W. Higgs, after whom the mechanism and the boson are named. However, the questions why some particles are heavier than others and how particles composed of light constituents can acquire large masses (e.g. pions, nucleons) are not explained by the Higgs mechanism.

Following the Standard Model of cosmology, after its creation in the Big Bang, the universe went through a stage during which matter existed as a sort of very hot and extremely dense soup, the so-called quark-gluon plasma (QGP) composed of the elementary building blocks of matter. As the universe expanded and cooled, the quarks became trapped into composite particles such as protons and neutrons, in others words: quarks became *confined*. From a theoretical point of view this is still not well understood and leaves many open questions (see e.g. [8]).

Besides the electroweak force, which describes interactions between charged particles, quark transitions and the behaviour of neutrinos, Quantum Chromodynamics (QCD) is a major part of the SM: it describes the strong interaction between quark and gluon constituents of matter, binds the nucleons within the atomic nucleus and governs the microscopic structure of matter at distances smaller than 10^{-15} m. Although QCD has been extensively studied in high energy regions, where perturbative methods are applicable, QCD calculations become very complicated in the low, non-perturbative energy region, where the distance between the quarks becomes comparable to the nucleon size. Two approaches are possible to receive a reliable theory for this region:

- the development of approximate theoretical models based on effective field theories, which are rooted in QCD symmetries and formulated in more relevant low-energy degrees of freedom or
- the more fundamental approach from basic principles using numerical calculations on a discretised space-time lattice, the so-called Lattice QCD (LQCD).

To keep control over systematic errors that may come from discretisation or computational limits, the second approach needs comparison with results of an effective field theory. Both approaches need confrontation with precise experimental data e.g. on hadron masses, hadron decay rates and information on the structure of hadrons.

Precise experimental data can be gained by the investigation of hadron physics in particle antiparticle annihilation reactions in non-perturbative energy regions, which can be performed in two different environments:

1. In **electron-positron colliders** such as BEPCII (Beijing Electron Positron Collider II) in Beijing, China, electrons and positrons are accelerated inside a ring and are brought to collision inside an onion-shell like detector, which measures the decay products of the collision. Since electrons and positrons are elementary particles with no substructure (as far as we know yet), e^+e^- annihilations create a very clean event topology inside the detector. In such reactions the initial state and the center-of-mass energy are well known, providing an ideal environment for charmonium spectroscopy and precision measurements of the hadron masses, decay rates and the structure measurements mentioned above. Nevertheless, there are two drawbacks, which need to be considered at e^+e^- machines:
 - a) Electrons and positrons annihilate into virtual photons, which have quantum numbers $J^{PC} = 1^{--}$. Since J^{PC} is conserved in all electromagnetic reactions, the virtual photon can only create states with quantum numbers $J^{PC} = 1^{--}$. Therefore all states with different quantum numbers can only be populated by higher order processes (which are very rare) or via a decay of higher mass hadrons with quantum numbers $J^{PC} = 1^{--}$.

- b) Electrons as well as positrons suffer from high energy losses due to synchrotron radiation ($\Delta E \propto 1/m^4$), when they are forced to circulate inside the ring of an accelerator. This sets an upper limit for the maximum center-of-mass energy of such ring accelerators.

Intriguingly, the second drawback also opens up a scenario for a relatively novel and interesting physics approach: Since electrons and positrons easily lose part of their energy due to electromagnetic fields, it is possible that one or even both of the particles radiate some of their energy immediately before the annihilation process, so-called Initial State Radiation (ISR). This reduces the center-of-mass energy of the reaction and changes the event topology because of an additional Lorentz-boost coming from the now asymmetric initial energies of the particles. Since e^+e^- reactions are calculable inside quantum electrodynamics, the probability for and the properties of such ISR events can be determined very precisely. Such events can be studied at the Beijing Electron Spectrometer III (BESIII) located at the institute for high energy physics (IHEP) in Beijing, China, and allow for very elegant and powerful physics measurements of important QCD parameters explained in more detail in chapter 3.

2. **Hadron-hadron machines** such as the future FAIR (Facility for Antiproton and Ion Research) facility with the $\bar{\text{P}}\text{ANDA}$ (Antiproton Annihilations at Darmstadt) experiment in Darmstadt, Germany, are complementary to e^+e^- machines for studies of particle-antiparticle annihilations. Hadron-hadron machines like $\bar{\text{P}}\text{ANDA}$ are capable of producing states with any non-exotic quantum number directly. This opens the door for direct production of states with non $J^{PC} = 1^{--}$ quantum numbers like the X(3872) [9] ($J^{PC} = 1^{++}$ [10]). Precision measurements of these states will reveal their hadronic structure and may give answers to yet unsolved questions of QCD. The drawback of hadron-hadron reactions is the lack of knowledge of the initial state, because protons and antiprotons have an internal structure and one never knows, which partons participate in the reaction.

The $\bar{\text{P}}\text{ANDA}$ experiment is a fixed-target experiment, where antiprotons are shot onto frozen hydrogen pellets. The experiment is designed in a way that the antiproton beam will not get lost after the reaction with the target, allowing for high beam intensities and luminosities. Since the conserved baryon number at $\bar{\text{P}}\text{ANDA}$ is zero ($\mathcal{B} = 0$), energy scans for e.g. width measurements of the exotic X(3872) state can be performed with high precision. $\bar{\text{P}}\text{ANDA}$ is going to study interactions between antiprotons and fixed target protons / nuclei in the momentum range of 1.5–15 GeV/c. Using a high energy storage ring (HESR), it is designed for precision measurements in the non-perturbative region of QCD. The scientific program of $\bar{\text{P}}\text{ANDA}$ is focused on fundamental questions of (mostly non-perturbative) QCD [11], which is explained

in more detail in chapter 2. One big challenge of the $\overline{\text{PANDA}}$ experiment is the data acquisition (DAQ) of huge amounts of data (several 100 Gb/s). Since events of interest are not easily distinguishable from background events with fixed hardware triggers, software triggers operated on Field Programmable Gate Arrays (FPGAs) will make the trigger decision in real time, allowing a high degree of flexibility for the trigger algorithms.

This thesis will contribute to both the BESIII and the $\overline{\text{PANDA}}$ experiments: A small calorimeter located in the very forward/backward region of BESIII is estimated to measure ISR photons and to improve the capabilities for ISR studies at BESIII. Corresponding simulations investigating the detector's capabilities and boundaries have been performed (see chapter 5). For proper functionality this ISR detector needs a fast DAQ, which is capable of correlating events from the ISR detector and the rest of the BESIII detectors in real time, thus the demands on its DAQ are very similar to those on the $\overline{\text{PANDA}}$ DAQ. A prototype DAQ for the ISR calorimeter has been developed using prototype $\overline{\text{PANDA}}$ DAQ modules (see chapter 6). The future installation of this detector at BESIII and the integration of its DAQ into the BESIII DAQ will improve the capabilities for ISR studies at BESIII and provide a unique and realistic high-rate environment for testing $\overline{\text{PANDA}}$ DAQ developments and gaining experience before the start of $\overline{\text{PANDA}}$.

This thesis will be structured as follows: Chapter 2 will give a brief overview of the $\overline{\text{PANDA}}$ and BESIII experiments and their physics programs, explaining this thesis's contribution to these experiments. A short introduction into ISR physics is given in chapter 3, while chapter 4 contains a description of the foreseen ISR calorimeter investigated in this thesis. Chapter 5 explains a Geant4 based simulation of the ISR detector simulated in the BESIII Offline Software System (BOSS) framework and describes the obtained results. The description of related developments for the detector's DAQ can be read in chapter 6, followed by a chapter containing results from test experiments with radioactive sources, cosmic rays and from a testbeam measurement with electrons at MAMI (Mainz Microtron, Mainz, Germany) using the DAQ described in chapter 6. In the final chapter of this thesis, results are summarized and conclusions and future perspectives are derived.

$\bar{\text{P}}\text{ANDA}$ AND BESIII

This thesis' work will cover topics and developments in close connection to the $\bar{\text{P}}\text{ANDA}$ and the BESIII experiment. At first an overview of the respective experimental detector setups will be given. Following this the overlapping physics program of both experiments will be outlined.

2.1. The $\bar{\text{P}}\text{ANDA}$ Project at FAIR

The Facility for Antiproton and Ion Research (FAIR) will be an accelerator facility with several experiments investigating atomic, plasma, nuclear and hadron physics at GSI in Darmstadt, Germany. It will include an extensive upgrade of the GSI facility with several new synchrotron- and storage rings and experiments, see Fig. 2.1.

FAIR will provide intense beams of antiprotons and rare isotopes, depending on the purpose of the different experiments. $\bar{\text{P}}\text{ANDA}$ will be using antiprotons created by shooting protons on a nickel target: With the help of a magnetic separator antiprotons will be filtered and transferred into the Collector Ring (CR), where the antiprotons get pre-cooled. After a compression to single bunches, the antiprotons are transferred to the Accumulator Ring (RESR), where stochastic cooling will further compress each bunch's phase space until the bunches are injected into the high energy storage ring (HESR), which hosts $\bar{\text{P}}\text{ANDA}$ [12]. At the first stage of acceleration the HESR serves as a slow synchrotron to bring the antiprotons to the desired energy. After that it will be used as a storage ring. It can be operated in two modes: high luminosity mode (HL) with beam intensities up to 10^{11} antiprotons in the HESR, allowing a luminosity of $\mathcal{L} = 2 \cdot 10^{32} \text{ cm}^{-2}\text{s}^{-1}$ and a high resolution mode (HR) with a relative momentum spread of 3 to $4 \cdot 10^{-5}$ [13]. The HESR at $\bar{\text{P}}\text{ANDA}$ is designed to store a beam of antiprotons in the momentum range of 1.5 to 15 GeV/c, which is shot on a hydrogen target, giving access to a center-of-mass energy range from 2.2 to 5.5 GeV/c².

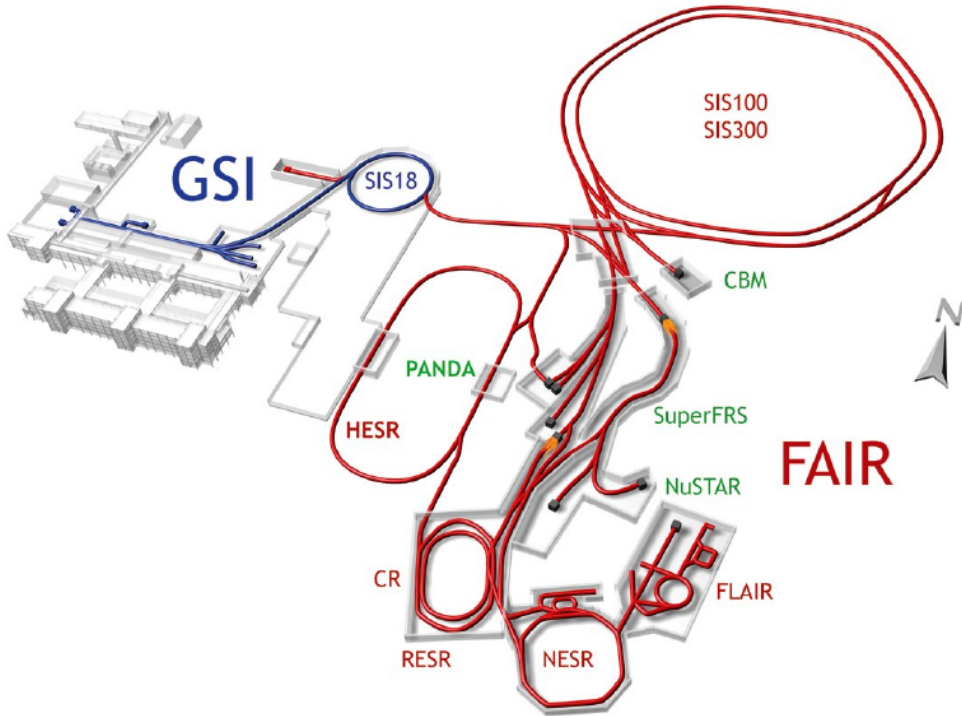


Fig. 2.1.: The GSI facility (blue) and all extensions for FAIR (red): Shown is the accelerator infrastructure with several synchrotron- and storage-rings of dedicated purpose and the location of the planned experiments. $\bar{\text{P}}\text{ANDA}$ will be located at the HESR [12].

2.1.1. The $\bar{\text{P}}\text{ANDA}$ Detector

The $\bar{\text{P}}\text{ANDA}$ physics objectives demand challenging requirements for the $\bar{\text{P}}\text{ANDA}$ detection system, which read as follows [14]: $\bar{\text{P}}\text{ANDA}$ needs a full 4π coverage of the solid angle and the capability to handle very high rates ($2 \cdot 10^7$ annihilations/sec). Furthermore a very good particle identification and momentum resolution for γ , e , μ , π , K , p , a good vertex reconstruction and an excellent calorimeter are needed.

The asymmetric $\bar{\text{P}}\text{ANDA}$ detector is subdivided into the target spectrometer (TS), consisting of a 2 T solenoid magnet around the interaction region, and a forward spectrometer (FS), based on a 2 T dipole magnet for the tracking of forward-traveling particles (see Fig. 2.2). The relativistic boost and the combination of both detector parts allow a nearly 4π coverage of the solid angle. Tracking, charged particle identification, electromagnetic calorimetry and muon detection are available in both spectrometer parts, allowing the detection of all final states relevant for the $\bar{\text{P}}\text{ANDA}$ physics objectives. Arranged in an onion-shell like structure $\bar{\text{P}}\text{ANDA}$ consists of several sub-detectors. Parts of the muon detector and the backward endcap calorimeter can be replaced by a dedicated nuclear target station and some additional photon detectors

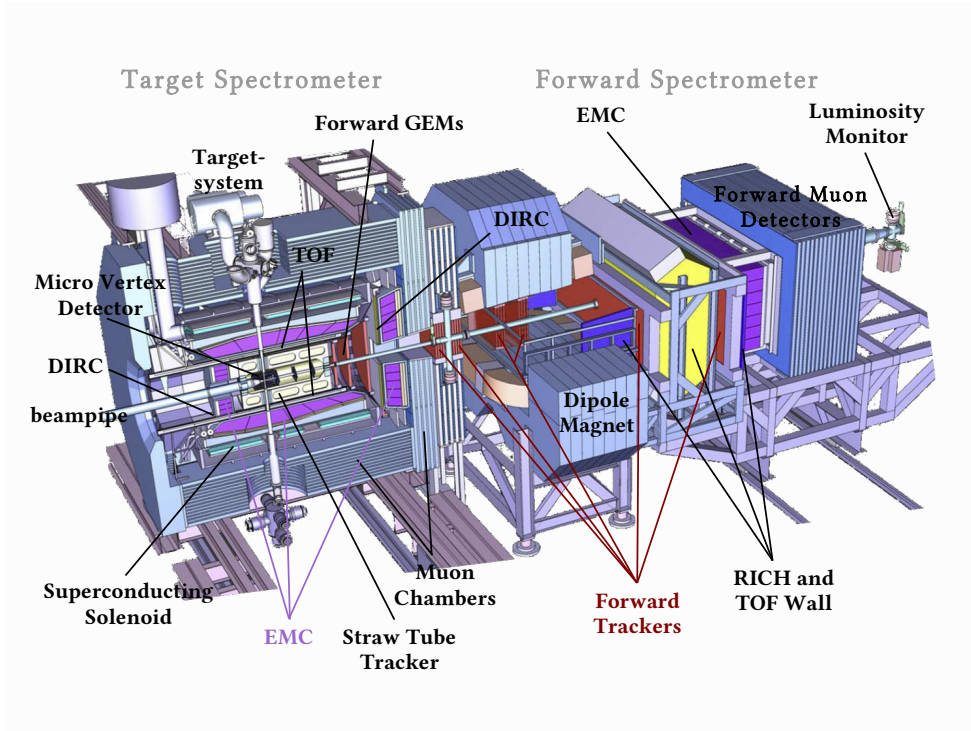


Fig. 2.2.: Schematic overview of the \bar{P} ANDA detector with its main modules.

in order to study hypernuclei. The next sections will briefly describe the main subdetectors, whereas the EMC will be explained in more detail since it is directly linked to the topic of this thesis.

Target Spectrometer

The Targetsystem

In order to reach the design luminosity a target thickness of about $4 \cdot 10^{15}$ hydrogen atoms per cm^2 is required [12]. Considering that the reaction shall take place inside the HESR without losing the antiproton beam, this is a real challenge. Two possible options are being developed:

Cluster-Jet Target Jets of hydrogen clusters can be formed by the expansion of pressurised cold hydrogen gas into vacuum through a Laval-type nozzle. With cluster sizes from 10^3 to 10^6 hydrogen molecules, such a cluster-jet would act as a very diluted target, allowing the antiprotons to pass without great losses.

Pellet target Frozen hydrogen micro-spheres with a size of 25-40 μm traverse the antiproton beam perpendicularly with a velocity of about 60 m/s. It is foreseen that the pellets have a lateral spread of $\sigma \approx 1$ mm and an interspacing between 0.5 and 5 mm.

The target densities are rather high, leading to high number of interactions in every pellet per antiproton bunch crossing. A resolution in the vertex position of 50 μm will be possible [12]. Other gases (e.g. Ar, N₂, Xe) can also be used as a frozen pellet target.

Studies for experiments comprising primary and secondary targets (hyper-nuclear studies) and liquid helium and a polarised ³He target are being undertaken. For the studies of antiproton-nucleus interactions a wire target may be employed [12].

The Micro-Vortex Detector

Being optimized for maximum acceptance and the detection of secondary vertices from *D* and hyperon decays, the micro-vertex detector (MVD) is placed close to the interaction point (IP) and plays an important role for the transverse momentum resolution. It consists of four layers of radiation-hard silicon pixel detectors with individual pixel readout circuits (inner two layers) and silicon strip detectors (outer two layers) arranged in a barrel layout with an inner radius of 2.5 cm and an outer radius of 13 cm. Another eight layers of silicon pixels (inner four layers) and silicon strip detectors (outer two layers, the other two layers are a combination of pixels and strips) are placed perpendicular to the beam direction in the forward region.

The Straw Tube Tracker

The Straw Tube Tracker (STT) consists of 4200 aluminized mylar tubes called *straws*, operated at 1 bar overpressure and positioned around the beam pipe at radial distances between 15 cm and 42 cm and an overall length of 150 cm [13]. All straws have a diameter of 10 mm and are arranged in 24 layers, of which the 8 central ones are tilted to achieve an acceptable *z*-resolution of 3 mm. The gas mixture used will be Argon based with CO₂ as quench gas. A gas gain of no greater than 10⁵ warrants long term operation. The resolution in *x* and *y* coordinates is expected to be less than 150 μm [15]. The design results in a material budget of only 1.3% of a radiation length, allowing precise calorimetry in the EMC.

Forward GEM Detectors

Three Gas Electron Multipliers (GEMs) placed 1.1 m, 1.4 m and 1.9 m downstream the target will track particles emitted at angles below 22°, which cannot be fully covered by the STT. The chambers have to sustain particle fluxes up to $3 \cdot 10^4 \text{ cm}^{-2}\text{s}^{-1}$ in close vicinity to the beam pipe. Gaseous micro-pattern detectors based on GEM foils as amplification stages are chosen [12].

Cherenkov Detectors

A good particle identification (PID) of hadrons and leptons is essential for any physics analysis to be done with $\overline{\text{PANDA}}$. Cherenkov detectors will cover the main part of the momentum spectrum above 1 GeV/ c . Below the Cherenkov threshold PID can be done by dE/dx measurements from the tracking detectors.

The **Barrel DIRC** (DIRC – Detection of Internally Reflected Cherenkov light) uses fused silica with a refractive index of 1.47 to perform PID at polar angles between 22° and 140° : particles with a velocity above the cherenkov threshold will radiate cherenkov photons under a certain, velocity-specific angle. Together with the momentum information of the tracking detectors, the mass of the traversing particle can be determined. The Barrel DIRC will consist of 1.7 cm thick quartz slabs surrounding the beam line at a radial distance of 45 - 54 cm providing pion/kaon separation between 800 MeV/ c and 5 GeV/ c [13]. It will be read out by micro-channel plate photomultiplier tubes (MCP PMTs), which can work in the strong magnetic field of the $\overline{\text{PANDA}}$ solenoid. The **Forward Endcap DIRC** uses similar concepts in the forward direction for particles between 5° and 22° .

Time-of-Flight

The **Barrel Time-of-Flight** detector will provide PID for slow particles at large polar angles. Since the flight path in the target spectrometer is only 50 - 100 cm, the detector is designed to have a time resolution of 100 ps [16]. For that purpose a Scintillator Tile Barrel with tiles of $28.5 \times 28.5 \text{ mm}^2$ size, individually read out by two Silicon Photomultipliers (SiPMs) per tile, is positioned just outside the DIRC and can also detect photon conversions in the DIRC radiator.

Electromagnetic Calorimeter

The performance of the electromagnetic calorimeter is of great importance for the success of $\overline{\text{PANDA}}$. It must be capable of measuring electrons, positrons and photons with high precision in the energy range from a few MeV up to several GeV. Lead tungsten scintillators with a sufficiently small radiation length ($X_0 = 0.89 \text{ cm}$) and Molière radius ($R_M = 2.00 \text{ cm}$) are chosen as material for the $\overline{\text{PANDA}}$ EMC. An overview of the most important properties of PbWO_4 to be used in $\overline{\text{PANDA}}$ is given in Tab. 2.1. The crystals of the EMC will be 20 cm long, corresponding to 22 X_0 , allowing an energy resolution better than 2% at 1 GeV with a tolerable longitudinal shower leakage.

The front sides of the tapered crystals have a size of $2.1 \times 2.1 \text{ cm}^2$, the barrel consists of 11360 crystals, the forward end cap has 3600 crystals, whereas the backward endcap

density ρ	8.28 g/cm ³
radiation length X_0	0.89 cm
Molière radius R_M	2.00 cm
τ_1 (fast component)	6.5 ns
τ_2 (slow component)	30.4 ns
ratio τ_1/τ_2	97/3
wavelength (at peak) λ_{max}	420 nm
energy loss dE/dx (MIP)	10.2 MeV/cm
relative lightyield (compared to NaI)	0.6 % (at 20°C) 2.5 % (at -25°C)

Tab. 2.1.: Important properties of PbWO_4 crystals to be used in $\overline{\text{PANDA}}$.

consists of only 592 crystals to accommodate the expected relatively low particle flux in the backward region. The design of the EMC barrel and forward end cap part can be seen in Fig. 2.3. The inner radius of the EMC is 57 cm and the crystals are arranged and tapered in a way that all particles from the IP enter the EMC crystals head-on. The readout of the crystals will be accomplished by large area avalanche photo diodes (LAAPDs) and vacuum photo-triodes (VPTs) [13]. Although LAAPDs have a larger gain and a better quantum efficiency, VPTs provide advantages such as radiation hardness and lower dark currents for an operation in very high rate environments such as the most forward region of the target EMC. Therefore LAAPDs will be used for the barrel EMC of $\overline{\text{PANDA}}$, whereas the endcap EMC readout will be accomplished by VPTs.

The EMC will be operated at a temperature of -25 °C in order to increase the lightyield of the lead tungsten crystals by a factor of 4 compared to an operation at room temperature (20 °C). Cooling the whole volume of the EMC down to -25 °C is a great challenge for the mechanical design of the EMC and its cooling and thermal insulation concepts, but this is necessary to meet the requirements for a successful execution of the $\overline{\text{PANDA}}$ physics program (see [13] for details).

Solenoid and Muon Chambers

With an inner radius of 90 cm and a length of 2.8 m, a superconducting solenoid coil will provide a homogeneous magnetic field of 2 T with a field homogeneity better than 2%. The magnetic return yoke of the solenoid hosts a range tracking system for a proper separation of muons and pions and decay muons. It works as an absorber and is interleaved with tracking detectors of 3 cm thickness in order to distinguish the particles by their specific energy loss in the absorber and the tracking devices. 2,600 rectangular aluminium drift tubes arranged in 13 sensitive layers with addi-

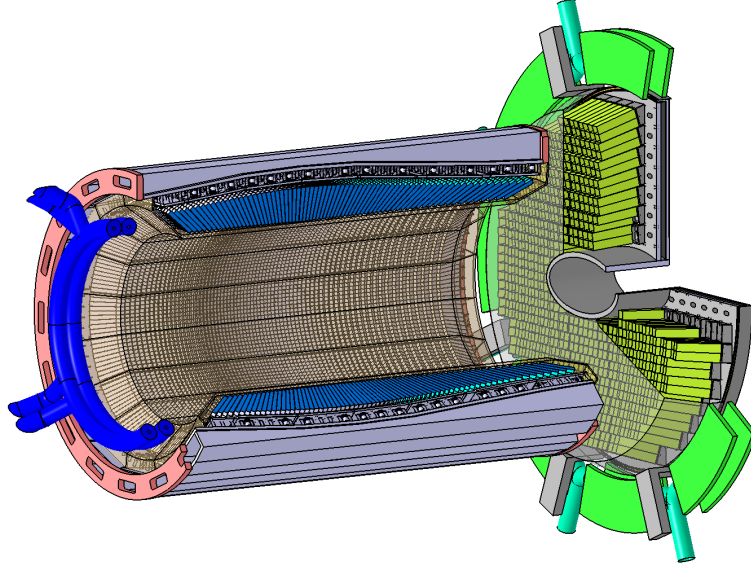


Fig. 2.3.: Layout of the \bar{P} ANDA electromagnetic calorimeter consisting of in total 15552 PbWO_4 crystals [12]. In order to maximize the EMC performance, the crystals have a different tapering in the different subparts of the detector.

tional capacitively coupled strips read out on both ends are used as detectors in the gaps between the absorber layers. The longitudinal coordinate can be extracted by comparing the signals of both ends of the strips.

Forward Spectrometer

The forward spectrometer covers the entire angular acceptance of the target spectrometer for all particles emitted in the angular region $5^\circ \leq |\theta| \leq 10^\circ$. It consists of several devices for particle tracking and PID.

Dipole Magnet

The dipole magnet with maximum bending power of 2 Tm will be used for the momentum analysis of charged particles in the forward spectrometer. It is placed 4 m downstream the target and it not only deflects particles coming from $p\bar{p}$ reactions, but also the \bar{p} beam itself (deflection of 2.2° at a momentum of 15 GeV/c). This beam deflection will be compensated by two correction dipole magnets [12].

Forward Trackers

Three pairs of tracking drift detectors will measure the deflection of particle trajectories in the field of the dipole magnet, where one unit will be placed in front, the second

within and the third behind the dipole magnet. All pairs consist of two autonomous detectors with each having four double layers of straw tubes: two with vertical wires and two with wires inclined by a few degrees for optimal tracking performance [16]. This design allows the separate track reconstruction in each pair, improving the detector performance for multi-track events.

Forward Particle Identification

A Ring Imaging Cherenkov (RICH) detector is proposed to be used for π/K and K/p separation at highest momenta. With two radiators, namely silica aerogel (refraction index 1.0304) and C_4F_{10} gas (refraction index 1.00137) the detector allows for $\pi/K/p$ separation between 2 and 15 GeV/c . Since the photodetectors are placed outside the active volume, the amount of material in front of the forward EMC is only $\sim 10.8\%$ of X_0 .

7 m from the target a wall of slabs made of plastic-scintillators serves as a time-of-flight stop counter. It is read out on both ends by fast photo-tubes, has an expected time resolution in the order of 50 ps and therefore allows for a π/K and K/p separation up to momenta of 2.8 GeV/c and 4.7 GeV/c , respectively [16]. A similar detector is placed inside the dipole magnet in order to measure low momentum particles not exiting the dipole magnet.

Forward Electromagnetic Calorimeter

Photons and Electrons will efficiently be detected by a high resolution Shashlyk-like calorimeter consisting of lead scintillator sandwich modules read out by incorporated wavelength-shifting fibers coupled to photo-multipliers. 351 of such modules are arranged in 13 rows and 27 columns at a distance of 7.5 m from the target, each module is subdivided into four channels independently read out by a PMT. The calorimeter length of 680 mm corresponds to $20 X_0$ aiming at an design energy resolution of $4\%/\sqrt{E}$ [16].

Forward Muon Detectors

In the very forward part of the detector a tracking system build of interleaved absorber layers and rectangular aluminium drift tubes is installed for the detection of muon with highest momenta. This system not only allows for the π/μ separation, but also for the detection of pion decays and the approximate energy determination of neutrons and antineutrons. This system will be placed about 9m from the interaction point [12].

Luminosity Monitor

For the measurement of any cross section, the knowledge of the time integrated luminosity L for the reactions at the IP is vital. The concept of $\overline{\text{PANDA}}$'s luminosity

measurement is based on the reconstruction of the angle of scattered antiprotons at very small polar angles of 3-8 mrad, measuring elastic antiproton-proton scattering as a reference channel for cross section normalization of a given process. For that purpose \bar{P} ANDA will use a sequence of four double-sided silicon strip detectors placed as far downstream (between $z = 10$ m and $z = 13$ m) and as close to the beam axis as possible.

2.1.2. The \bar{P} ANDA Readout Concept

\bar{P} ANDA must be capable of handling at least 2×10^7 events per second. One major difficulty in the data acquisition of such huge amounts of data (several 100 Gb/s) at \bar{P} ANDA is the lack of hardware triggers, since potentially high contributions from background events are not easily distinguishable from rather rare events of interest. Therefore a new readout concept based on algorithms processed on Field Programmable Gate Arrays (FPGAs) is being developed, allowing a high degree of flexibility in the choice of trigger algorithms: every sub-detector system is an autonomous self-triggering entity with noise-suppression, hit-detection and signal preprocessing units. During preprocessing the most important information is extracted and marked with a precise timestamp, thus substantially reducing the data which is then buffered for further processing. All subdetectors are connected to a versatile optical network called SODA (Synchronization of Data Acquisition), which monitors data acquisition modules and data flow control. It also delivers a common reference time and allows for the determination of detector signal timings with high precision [17], providing the foundation for subdetector correlation and event building. The data is then buffered on Compute Nodes (CN), which finally deliver the trigger decision based on the data from all subdetectors, allowing trigger conditions, which are outside the capabilities of standard approaches [12]. The accepted events are then transmitted to a computer farm for mass storage. A schematic view of the EMC's readout chain is shown in Fig. 2.4.

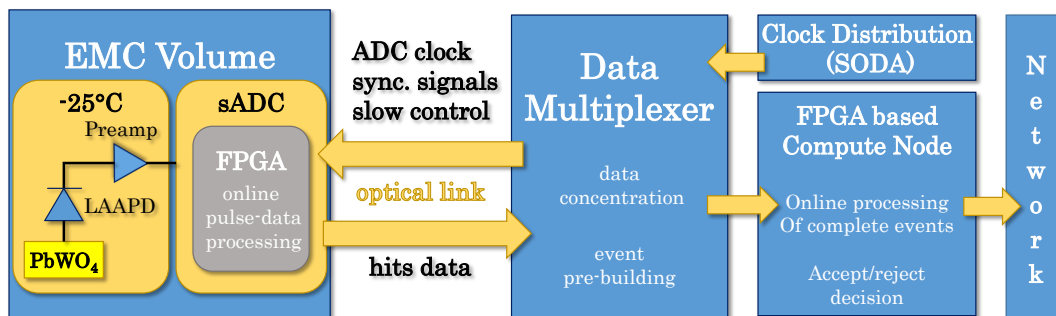


Fig. 2.4.: The logic scheme of the trigger-less readout of the \bar{P} ANDA EMC. Lead tungsten crystals will be read out by LAAPDs followed by shaping preamplifiers. These signals go into an sampling ADC (sADC), where a FPGA does on-line pulse-data processing. Via an optical link the extracted data is sent to a data multiplexer, where all signals from all digitizer modules are gathered and concentrated and time stamp-based event pre-building is done via SODA. The concentrated event data is then sent to a FPGA based Compute Node (CN), where eventbuilding is performed. Based on programmable criteria the events are accepted or rejected and the accepted events are sent to the network fabric for mass storage.

2.2. The BESIII Experiment

The BESIII experiment is located at the BEPCII collider at IHEP, which is a symmetric e^+e^- collider covering the energy region for physics investigations of *charm*-quarks and τ -leptons. BEPCII is following the BEPC electron-positron collider operated from 1989 to 2004 at IHEP, which was a single ring operated in a single bunch mode with maximum luminosity being $\sim 1 \cdot 10^{31} \text{ cm}^{-2}\text{s}^{-1}$ [18]. BEPCII is a double ring multi-bunch collider and a major upgrade compared to BEPC, almost all components have been replaced in order to meet the design parameters for a successful execution of the BESIII physics program. The main design parameters of the BEPCII collider are summarized in Tab. 2.2. Its high luminosity of $10^{33} \text{ cm}^{-2}\text{s}^{-1}$ allows for the collection of large data samples and thus high precision studies in an energy region at the boundary of the perturbative and non-perturbative regime of QCD ($\sqrt{s}_{\text{BESIII}} = 2.0 - 4.6 \text{ GeV}$). BESIII has already collected the world's largest data sets in the charmonium region (see Tab. 2.3) allowing for precision measurements in the τ -charm sector.

\sqrt{s} [GeV]	2 - 4.6
Circumference [m]	237.5
RF frequency [MHz]	499.8
Number of bunches	2 · 93
Beam current [mA]	910
Bunch length σ_z [cm]	1.5
Bunch size ($\sigma_x \times \sigma_y$) [μm]	$\sim 380 \times \sim 5.7$
Crossing angle [mrad]	± 11
luminosity [$\text{cm}^{-2}\text{s}^{-1}$]	$1 \cdot 10^{33}$

Tab. 2.2.: Design parameters of the BEPCII collider [19].

Resonance	J/ψ	$\psi(2S)$	$\psi(3770)$	$\psi(4040)$
	$1.3 \cdot 10^9$ events	$0.5 \cdot 10^9$ events	2.9 fb^{-1}	$\sim 0.5 \text{ fb}^{-1}$
Energy [MeV]	4260 [Y(4260)]	4360 [Y(4360)]	4260 - 4360 [†]	3850 - 4590 [‡]
	$\sim 1.9 \text{ fb}^{-1}$	$\sim 0.5 \text{ fb}^{-1}$	$\sim 0.5 \text{ fb}^{-1}$	$\sim 0.8 \text{ fb}^{-1}$

Tab. 2.3.: Some BESIII data sets collected in the charmonium region until August 2014 [20] ([†] energy scan, [‡] R-scan).

The BEPCII accelerator is also operated as a synchrotron radiation facility, where high current electron beams with energy 2.5 GeV are used as a source for high flux synchrotron radiation.

2.2.1. The BESIII Detector

The detector design of BESIII has been optimized for best performance regarding the BESIII physics program. The most probable particle momentum in typical hadronic final states is approx. 0.3 GeV/c and most of all produced particles have a momentum smaller than 1 GeV/c. The most probable photon energy is around 100 MeV, the expected average multiplicity for charged particles and photons is in the order of four per event [21]. Like every currently operating detector for high energy physics measurements, BESIII has an onion-shell like design with several subdetectors for measuring specific particle properties: its main components are a drift chamber for measuring momenta of charged particles, a time-of-flight detector for particle identification and an electromagnetic calorimeter for electron and photon energy measurements. A big 1 Tesla superconducting solenoid magnet contains resistive plate chambers for muon measurements. Fig. 2.5 shows a schematic overview of the BESIII detector.

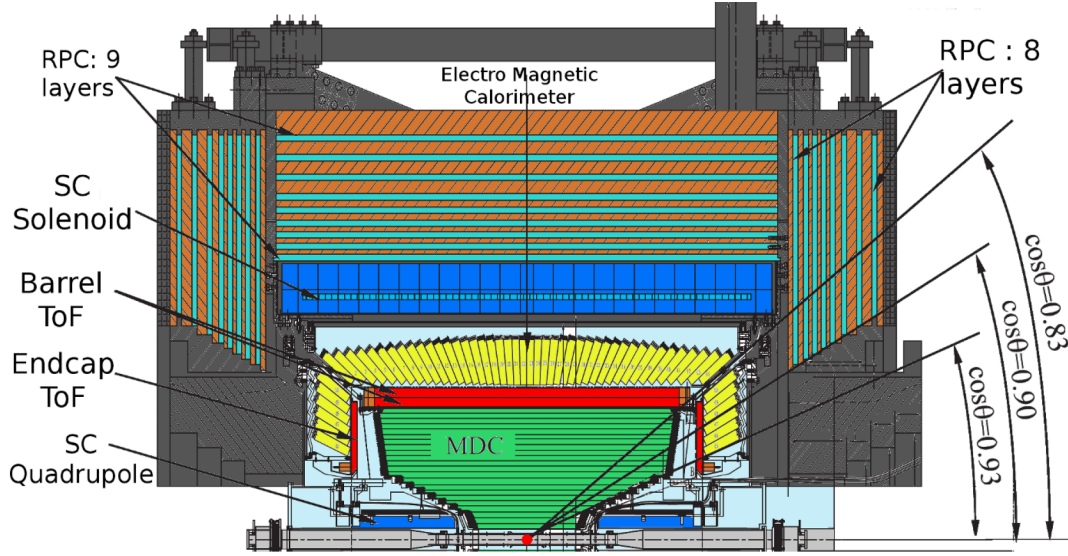


Fig. 2.5.: Schematic overview of the BESIII detector [22].

Mini Drift Chamber (MDC)

The MDC is the innermost detector of BESIII and one of the most important subdetectors, since it can precisely determine the momentum of charged particles by measuring the particle trajectory in a well known magnetic field. With an inner radius of 60 mm, outer radius of 800 mm and a maximum length of 2400 mm, the MDC covers a polar angle $|\cos\theta| < 0.93$. The MDC consists of 43 cylindrical layers of drift cells with 8 inner stereo chambers, and a total of 35 outer chambers, of which 16 stereo layers are interleaved with 19 axial layers. In total, 6796 gold-plated tungsten signal wires lead to an average drift cell with a half-width of 6 mm in the inner chamber and 8.1 mm in the outer chamber. The MDC uses a helium-based gas mixture ($\text{He}/\text{C}_3\text{H}_8 = 60/40$) as working gas, which has proven to be a good compromise to reduce multiple Coloumb scattering, but maintaining a good dE/dx resolution. The MDC has a single-wire resolution of $120 \mu\text{m}$ in the $R-\phi$ plane and 2 mm in the z -direction, the dE/dx resolution is better than 6% and the corresponding momentum resolution is better than $\sigma_{p_t}/p_t = 0.32\%p_t \oplus 0.37\%/\beta$. The first term originates from trajectory measurements and the second term from multiple Coulomb scattering.

Time-Of-Flight System (TOF)

The TOF is cylindrically placed around the MDC and consists of plastic scintillator bars read out by fine-mesh photomultiplier tubes (PMT). The TOF not only measures the flight time of the particles in order to perform particle identification, but also delivers fast trigger signals. It consists of a barrel and an endcap part, where the barrel part covers the angular region $|\cos\theta| < 0.83$, while the endcap covers $0.85 <$

$|\cos\theta| < 0.95$. The barrel part consists of two layers of 88 plastic scintillators, which are arranged in a cylinder around the MDC with a mean radius ~ 870 mm. Each bar has a length of 2380 mm and a thickness of 50 mm. The barrel counters are read out at both ends, providing a total time resolution of 100 ps. The endcap TOF with inner radius of 410 mm and an outer radius of 890 mm is located behind the MDC's endplate and consists of a single layer of 48 fan-shaped elements, each read out from one end by a single fine-mesh PMT. The design time resolution of 110 ps has only been reached for dimuon events, but for electrons the time resolution is around 150 ps, due to interactions with the MDC's endcap plate [23]. π/K separation at a 2σ level is possible up to 1 GeV/c momenta.

Electromagnetic Calorimeter (EMC)

Outside the TOF, the BESIII EMC is placed to measure position and energy of electrons and photons and to provide trigger signals. The calorimeter itself consists of 6272 CsI(Tl) crystals, arranged in a barrel part of 44 rings, each holding 120 crystals and an endcap part and each consisting of 6 rings that are split into two tapered half-cylinders in order to achieve head on particle impacts. Each crystal has a length of 28 cm, which corresponds to 15 radiation lengths (X_0), the front face of each crystal is a square of side length 5.2 cm. The barrel has an inner radius of 940 mm and a length of 2750 mm, providing an energy measurement range for electrons and photons from 20 MeV to 2 GeV [24]. The energy resolution is about $2.3\%/\sqrt{E(\text{GeV})} \oplus 1\%$, the design position resolution for electromagnetic showers is $\sigma_{xy} \leq 6 \text{ mm}/\sqrt{E(\text{GeV})}$. The angular coverage of the barrel EMC is $|\cos\theta| < 0.82$, the endcap covers the region $0.83 < |\cos\theta| < 0.93$.

Muon Identifier

Characteristic hit patterns when penetrating the return yoke of the solenoid magnet measured by resistive plate chambers (RPC) provide distinction of muons and hadrons. The barrel part has nine layers of steel plates with a total thickness of 41 cm, interleaved with nine layers of RPCs with the first layer placed in front of the steel. As muons lose 160 MeV of energy in the crystals of the EMC, the muon identifier becomes effective at momenta above 0.4 GeV/c.

Luminosity Determination

The determination of the integrated luminosity is crucial for achieving the physics goals of BESIII. The luminosity is determined by measuring the three main QED process $e^+e^- \rightarrow e^+e^- \mu^+\mu^-$ and $\gamma\gamma$ using information from all subdetectors of BESIII. For monitoring the luminosity, fused silica blocks read out by PMTs are used, which are placed in the very forward/backward region 3.35 m from the interaction point.

The luminosity determination is done by measuring photons from radiative Bhabha scattering events on a bunch-by-bunch basis [21]. One of the luminosity monitors was already replaced by a zero degree detector (ZDD) for additional initial state radiation measurements, explained in more detail in chapters 3 and 4.

DAQ System and Event Filter

Based on VME and an online computer farm, the BESIII DAQ is designed to read out data from the front-end electronics system (FEE) and record valid data on permanent storage devices. After Level 1 triggers are received, the DAQ system transfers all subdetector data to the online computer farm. The computer farm not only does event reconstruction, event filtering and background suppression, but also controls and monitors the DAQ operation. The maximum data rate for writing on permanent storage is about 40 MB/s [21].

2.3. The Physics Program of BESIII and PANDA

The aim of BESIII and PANDA is the study of fundamental questions of QCD, aiming to connect the perturbative and the non-perturbative QCD regions, see Fig. 2.6. This includes the physics of gluonic excitations, hybrid and exotic states, strange- and charm quark physics, and in case of PANDA also hyperon-nucleon, hyperon-hyperon interactions and spin-structure functions of the proton [25]. Both experiments have set their focus according to the strengths of their approach: PANDA is very good at measuring states with $J^{PC} \neq 1^{--}$, therefore this is the emphasis of its physics program, whereas BESIII takes full advantage of its clean e^+e^- environment and therefore focuses on precision measurements of decays of states with $J^{PC} = 1^{--}$. Both approaches are complementary to each other and allow for broad physics investigations in the charm region.

Since both experiments investigate the same energy region, their physics programs have much in common, a few of the main topics are described in the next sections.

2.3.1. Charmonium Spectroscopy

Lower-lying bound $c\bar{c}$ states can be described fairly well in terms of non-relativistic heavy-quark potential models. An often used Ansatz is the phenomenologically derived *Cornell*-potential [26], which reads as

$$V(r) = -\frac{4\alpha_s}{3r} + \sigma r \quad , \quad (2.3.1)$$

with r being the distance between quark and antiquark, α_s being the strong coupling constant and σ being a string tension introduced to account for confinement of the quarks.

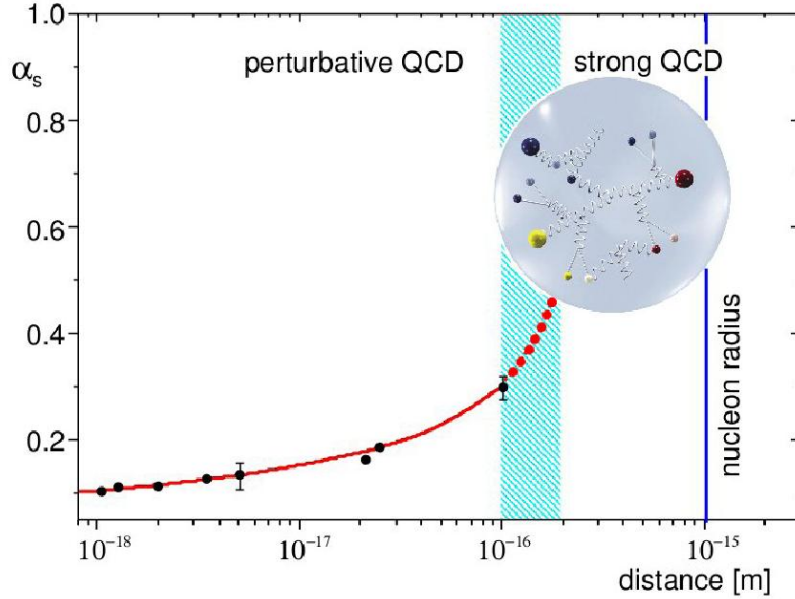


Fig. 2.6.: The strong coupling constant as function of the distance between the partons. When it comes to values close to the nucleon size, QCD becomes highly non-perturbative (graphic taken from [12]). $\bar{\text{P}}\text{ANDA}$ and BESIII are aiming to investigate physics in this region.

The first term describes a Coulomb-like force at short distances dominated by a one-gluon exchange. Solving the *Schrodinger*-equation with that potential and a few additional corrections to account for spin-spin, spin-orbit and tensor interactions arising from the magnetic dipoles of the quarks (see [27] for details), one achieves predictions in good agreement with the observed charmonium states below the $D\bar{D}$ threshold, see Fig. 2.7.

$\bar{\text{P}}\text{ANDA}$ and BESIII are capable of performing precision measurements of charmonium transitions and of the mass and width of charmonium(-like) states below and above the $D\bar{D}$ threshold allowing further investigation of the confinement potential of QCD. Measurements of the ψ states with $J^{PC} = 1^{--}$ have extensively been performed at BESIII, where the states can directly be formed via coupling to a virtual photon. Thanks to the huge data sets that have already been collected very rare decay channels can be investigated, where any deviation to SM predictions would be a hint for new physics beyond the SM. States with other quantum numbers than that of the virtual photon can only be populated via higher order processes or indirectly via particle decays. In contrast, $\bar{p}p$ annihilation reactions like those at $\bar{\text{P}}\text{ANDA}$ offer the possibility to form excited charmonium states of all non-exotic quantum numbers directly. The resolution in mass and width is only limited by the resolution of the phase-space cooled beam momentum distribution, which is significantly better than the detector resolution. Investigations on the yet somehow inconsistent properties of

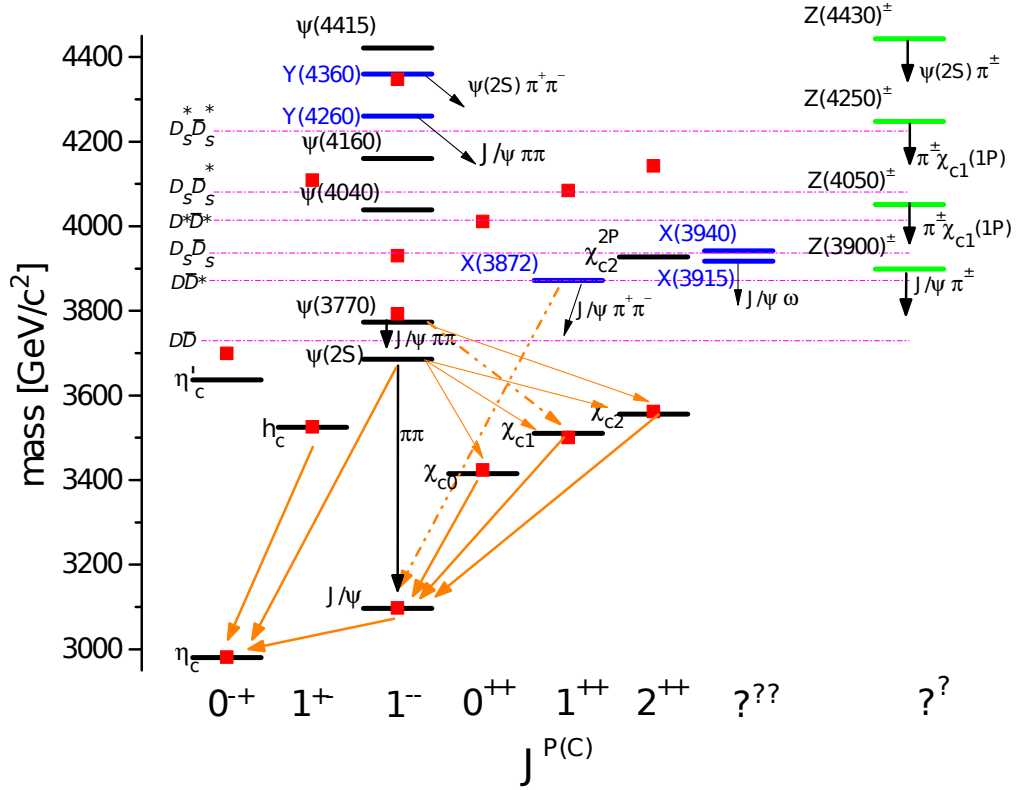


Fig. 2.7.: Spectrum of experimentally measured states in the charmonium region with respective quantum numbers, taken from [22]. The black lines indicate states, which are well described in the $c\bar{c}$ picture whereas the blue lines represent experimentally measured neutral states, which do not fit in the ordinary $c\bar{c}$ model. The charged resonances described by the green lines cannot be simple $q\bar{q}$ states and their hadronic structure is not clear yet. The arrows and their labels show some observed decays, radiative γ transitions are drawn in orange. The important $D\bar{D}$ thresholds are represented by the purple lines. The red squares are results coming from the Schroedinger equation using the Cornell potential and respective perturbative corrections [27]. Even this simple model is able to describe the charmonium spectrum below the $D\bar{D}$ thresholds pretty well.

the η_c ground state (see e.g. [28–32]), the spin-dependence of the $q\bar{q}$ potential and the understanding of states above the $D\bar{D}$ threshold are further examples of the broad charm physics program $\overline{\text{PANDA}}$ and BESIII cover.

The last decade was full of discoveries of charmonium-like states, which do *not* fit in the simple $c\bar{c}$ picture, e.g. the $X(3872)$ [9] ($J^{PC} = 1^{++}$ [10]) discovered by Belle or the charged charmonium-like state $Z(3900)^\pm$ [33] discovered at BESIII . Recently,

further discovered states of yet unknown structure in the charmonium region (see e.g. [34–38]) promise an interesting and enlightening future of charmonium spectroscopy at $\overline{\text{PANDA}}$ and BESIII.

2.3.2. Open Charm Physics

D-mesons (D^\pm , D^0 , D_s) can be produced via decays of $\psi(3770)$ (D^\pm , D^0) and $\psi(4040)$ (D^\pm , D^0 , D_s). Measurements of the decay constants f_D and f_{D_s} can be performed as well as measurements of the CKM matrix elements V_{cs} and V_{cd} and tests of various other theoretical predictions for the decay of those mesons. The high luminosities of both experiments also allow for studies of rare or SM-forbidden D-decays, for measurements of the $D\overline{D}$ mixing, and search for CP-violation in the $D\overline{D}$ system.

2.3.3. Hybrids, Glueballs, and other Exotics

The self-coupling of the gluons in QCD leads to interesting phenomena: hadronic systems exclusively made of gluons, so-called *glueballs* and bound $q\bar{q}$ systems with a strong gluon component (*hybrids*). The additional degrees of freedom carried by the gluon allow these states to have spin-exotic quantum numbers i.e. quantum numbers, which are not allowed for usual fermion-antifermion systems. States with exotic quantum numbers provide the best opportunity to distinguish between gluonic hadrons and $q\bar{q}$ states. Glueballs and hybrids do not necessarily need to carry exotic quantum numbers, gluonic hadrons with conventional quantum numbers can be identified by measuring their properties and comparing them to predictions from theory e.g. LQCD calculations.

At BESIII the anomalous near-threshold mass enhancement seen in various baryonic channels [39–42], which has various theoretical interpretations, can be studied using the ISR technique explained in more detail in the next chapter.

BESIII is also capable of investigating τ -physics, which is not possible at $\overline{\text{PANDA}}$, whereas $\overline{\text{PANDA}}$ has the capability to study hyperons and hadrons in the nuclear medium, when the hydrogen target is replaced by a target consisting of higher mass nuclei. Since this is an important part of the $\overline{\text{PANDA}}$ physics program, it will be outlined in the next sections.

2.3.4. Hadrons in the Nuclear Medium

When hadrons are embedded in a nuclear many-body system, their properties such as masses and widths can change [43–46]. The study of medium modifications of hadrons is aimed at understanding the origin of hadron masses in the context of spontaneous chiral symmetry breaking in QCD and its partial restoration in a hadronic environment [13]. Since $\overline{\text{PANDA}}$ is capable of examining $\bar{p}A$ reactions, $\overline{\text{PANDA}}$ can not only

study in-medium modifications of the light π , K and ω mesons, but also of mesons containing heavy quarks such as the D meson. For instance, a modification of the energy threshold for the production of D mesons could be observed, if the D meson mass would be modified by in-medium effects. A lowering of the D mass may also lead to changes in the width of charmonium states, which usually lie just below the $D\bar{D}$ production threshold: It could cause these states to reside above the $D\bar{D}$ threshold and increase their width drastically, which could be experimentally verified [25]. The in-medium masses of such states are expected to be affected primarily by the gluon condensate [11].

2.3.5. Hypernuclei

Nuclei in which one or more nucleons are replaced by a hyperon, a nucleon containing at least one strange quark, are called hypernuclei. While protons and neutrons inside a nucleus are restricted by the Pauli-principle, the interesting thing about a hyperon bound in a nucleus is that it can populate all possible nuclear states and therefore offers a selective probe of the hadronic many-body problem [11]. Single and double Λ -hypernuclei were discovered 50 [47] and 40 [48] years ago, but only 6 double Λ -hypernuclei are presently known [25]. An important goal is the measurement of level spectra and decay properties of hypernuclei in order to test microscopic structure models [11]. \bar{P} ANDA will allow the efficient production of hypernuclei with more than one hyperon by shooting a 3 GeV/c \bar{p} on a primary target in order to produce $\Xi^- \bar{\Xi}$ pairs:

$$\bar{p} + N \rightarrow \Xi^- \bar{\Xi} \quad . \quad (2.3.2)$$

The process of implanting a $\Lambda\Lambda$ pair inside a nucleus proceeds via 7 steps [49]:

1. Reaction (2.3.2) occurs quasi free in a nucleus.
2. The Ξ^- rescatters in the residual nucleus and gets strongly decelerated. Both steps happen in the primary target.
3. Inside a secondary target, the Ξ^- slows down to stop and
4. is then captured by an atom.
5. After an atomic cascade,
6. the Ξ^- gets captured into the nucleus and
7. then makes the conversion reaction

$$\Xi^- + p \rightarrow \Lambda \Lambda \quad . \quad (2.3.3)$$

With an energy excess of only 28 MeV, the probability of both Λ 's getting stuck in the nucleus is rather high [49]. The (double) hypernucleus can then be examined using Germanium detectors for high resolution γ spectroscopy.

The hypernuclei program of PANDA will open new perspectives for the studying of hyperon-nucleon and hyperon-hyperon interactions and therefore for the study of the nuclear structure.

THE PHYSICS OF INITIAL STATE RADIATION

The physics of Initial State Radiation (ISR) is well understood and calculable within QED. When speaking about ISR physics, one usually does not refer to the physics behind ISR, but to the application of ISR physics for measurements in different energy regions. This chapter will briefly outline and explain the physics behind ISR and some of its applications in modern physics experiments, including possible ISR measurements at BESIII.

The upgrade of the existing Zero Degree Detector (ZDD) at BESIII (see section 4.2) will improve the capabilities for studying events, where one or both primary particles (e^+/e^-) radiate a photon before the annihilation process happens. This process is referred to as *Initial State Radiation* (ISR) or *Radiative Return*, a Feynman diagram of such a process is shown in Fig. 3.1. The energy of the radiating electron/positron will be diminished by the photon's energy, and the initially symmetric e^+e^- system at BESIII will get a Lorentz-boost and the event's structure becomes asymmetric. The study of such events offers a number of interesting investigation possibilities described in the next sections.

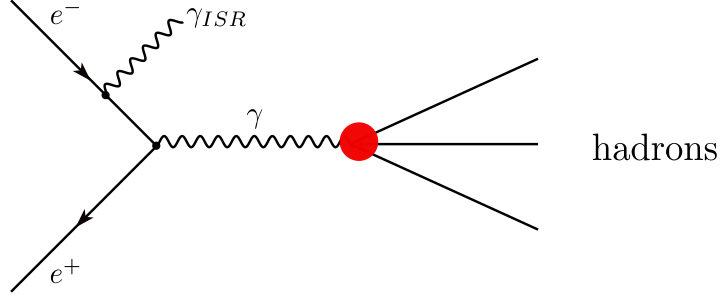


Fig. 3.1.: Feynman diagram of initial state radiation: In this case the electron emits a photon γ_{ISR} before the annihilation occurs.

3.1. ISR Physics and Its Applications

Using relativistic kinematics and the Lorentz-invariant Mandelstam s variable ($s = (p_1 + p_2)^2$) and assuming primary particles e^\pm with initial four-momenta $p_{e^+/e^-} = (\sqrt{s}/2, 0, 0, \pm p_z)^T$, $p_z = \sqrt{s/4 - m_e^2}$, of which one radiates a photon with energy $E_{\gamma_{\text{ISR}}}$ in z -direction, then s_{ISR} becomes

$$\begin{aligned}
 s_{\text{ISR}} &= \left(\left(\begin{array}{c} \frac{\sqrt{s}}{2} - E_{\gamma_{\text{ISR}}} \\ 0 \\ 0 \\ \sqrt{\left(\frac{\sqrt{s}}{2} - E_{\gamma_{\text{ISR}}}\right)^2 - m_e^2} \end{array} \right) + \left(\begin{array}{c} \frac{\sqrt{s}}{2} \\ 0 \\ 0 \\ -p_z \end{array} \right) \right)^2 = \left(\begin{array}{c} \sqrt{s} - E_{\gamma_{\text{ISR}}} \\ 0 \\ 0 \\ \sqrt{\left(\frac{\sqrt{s}}{2} - E_{\gamma_{\text{ISR}}}\right)^2 - m_e^2} - p_z \end{array} \right)^2 \\
 &= s^2 - 2E_{\gamma_{\text{ISR}}} \sqrt{s} + E_{\gamma_{\text{ISR}}}^2 \\
 &\quad - \left(\frac{s^2}{4} - E_{\gamma_{\text{ISR}}} \sqrt{s} + E_{\gamma_{\text{ISR}}}^2 - m_e^2 - 2 \cdot p_z \cdot \sqrt{\left(\frac{\sqrt{s}}{2} - E_{\gamma_{\text{ISR}}}\right)^2 - m_e^2} + p_z^2 \right),
 \end{aligned}$$

which finally yields the available center of mass energy

$$\sqrt{s_{\text{ISR}}} = \sqrt{\frac{1}{2}s - E_{\gamma_{\text{ISR}}} \cdot \sqrt{s} + 2m_e^2 + 2 \cdot \sqrt{\left(\frac{s}{4} - m_e^2\right) \left(\frac{s}{4} - E_{\gamma_{\text{ISR}}} \cdot \sqrt{s} + E_{\gamma_{\text{ISR}}}^2 - m_e^2\right)}} \quad (3.1.1)$$

by exploiting the ISR process

$$e^+e^- \rightarrow e^+e^- + \gamma_{\text{ISR}} \rightarrow \text{hadrons} + \gamma_{\text{ISR}} \quad .$$

Although Eq. (3.1.1) is derived from the simplest case, when the photon is radiated in z -direction, it is also valid for any other photon direction, since $\sqrt{s_{\text{ISR}}}$ is Lorentz-invariant and only dependent on the initial CMS energy \sqrt{s} and the energy of the radiated photon $E_{\gamma_{\text{ISR}}}$. When the photon's emission angle changes, the resulting Lorentz

boost of the system changes, but \sqrt{s}_{ISR} remains the same. For later calculations it is important to keep in mind that as soon as $E_{\gamma_{\text{ISR}}}$ is fixed, \sqrt{s}_{ISR} is also fixed.

Using the same calculation scheme and the upper limit for $E_{\gamma_{\text{ISR}}}$, which is given by the kinetic energy of the radiating particle, the calculation yields $\sqrt{s}_{\text{ISR}} = \sqrt{2m_e^2 + m_e \cdot \sqrt{s}}$ for the lower limit of \sqrt{s}_{ISR} . In such a case all kinetic energy of the initial particle is carried away by the photon. Fig. 3.2 shows Eq. (3.1.1) plotted as a function of $E_{\gamma_{\text{ISR}}}$ for $\sqrt{s} = 3770 \text{ MeV} = E_{\psi(3770)}$.

Even such simple calculations show the great potential of ISR physics, since the radiation of an ISR photon diminishes the available center-of-mass energy, allowing for measurements in energy regions below the experiment's designated energy threshold, which is fixed by the accelerator.

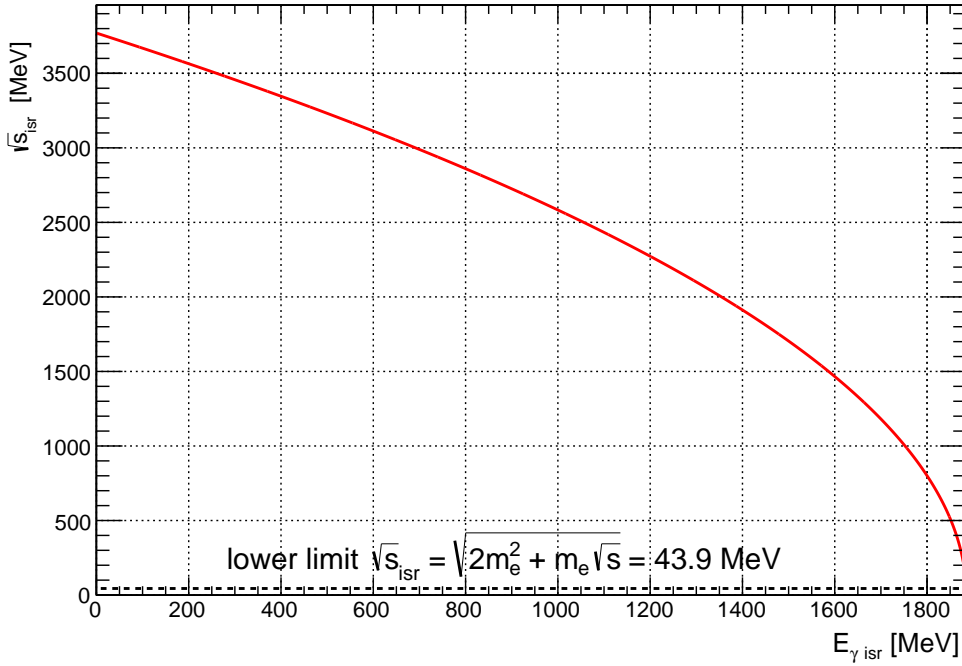


Fig. 3.2.: Initial state radiation: A photon with energy $E_{\gamma_{\text{ISR}}}$ is emitted by an electron or positron before the annihilation occurs. This plot shows the available CMS energy \sqrt{s}_{ISR} in dependence of $E_{\gamma_{\text{ISR}}}$ according to formula (3.1.1) (initial CMS energy $\sqrt{s} = 3770 \text{ MeV} = E_{\psi(3770)}$, both particles have initial energy $E_{e\pm} = \frac{\sqrt{s}}{2}$ and $p_z = \pm\sqrt{s/4 - m_e^2}$). The higher the energy of the emitted photon, the more energy will “get lost” in the motion of the CMS. The lower limit for \sqrt{s}_{ISR} is derived from the scenario of the photon carrying away all the particle’s kinetic energy in which case the particle basically becomes a fixed target.

Fig. 3.2 shows that measurements of the hadronic cross section and the R ratio, which is defined as

$$R(\sqrt{s}_{\text{ISR}}) = \frac{\sigma(e^+e^- \rightarrow \text{hadrons})_{\text{exp.}}}{\sigma(e^+e^- \rightarrow \mu^+\mu^-)_{\text{theo.}}} \Big|_{\sqrt{s}_{\text{ISR}}} \quad (3.1.2)$$

are accessible via ISR from threshold up to nominal energy. An impressive example of R ratio measurement results obtained with the help of ISR techniques can be seen in Fig. 3.3 taken from [50].

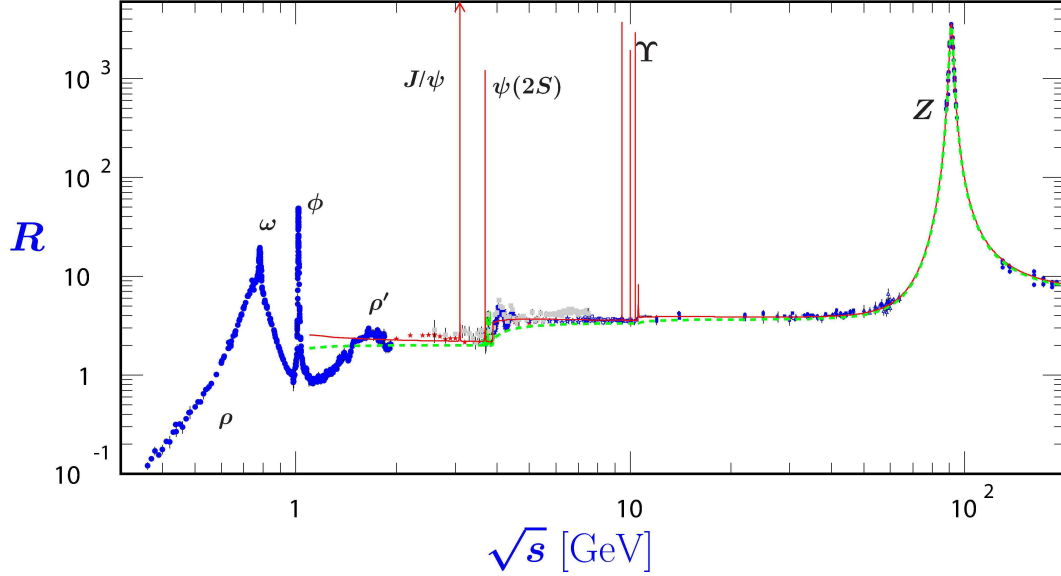


Fig. 3.3.: R value measurements combining standard energy scan and ISR techniques [50]

In lowest order QED the probability density of the initial state radiation of a photon with energy $E_{\gamma_{\text{ISR}}} = x \cdot E_0$, $0 \leq x \leq 1$, emitted into a polar angle θ can be written as [51–53]

$$w_0(\theta, s, x) = \frac{\alpha}{\pi x} \cdot \left[\frac{\left(1 - x + \frac{x^2}{2}\right) \sin^2 \theta - \frac{x^2}{2} \sin^4 \theta - \frac{4m_e^2}{s} \left((1 - 2x) \sin^2 \theta - x^2 \cos^4 \theta\right)}{\left(\sin^2 \theta + \frac{4m_e^2}{s} \cos^2 \theta\right)^2} \right], \quad (3.1.3)$$

with α being the fine structure constant. Integrating Eq. (3.1.3) over the whole polar angle one arrives at [53]

$$W(s, x) = \int_{\theta=0}^{\pi} w_0(\theta, s, x) \sin \theta \, d\theta = \frac{2\alpha}{\pi x} \left(2 \ln \left(\frac{\sqrt{s}}{m_e} \right) - 1 \right) \left(1 - x + \frac{x^2}{2} \right), \quad (3.1.4)$$

which is the probability density of emitting a photon at \sqrt{s} with energy $E_{\gamma_{\text{ISR}}} = x \cdot E_0$. Fig. 3.4 shows Eq. (3.1.4), plotted for $\sqrt{s} = 3770 \text{ MeV} = E_{\psi(3770)}$.

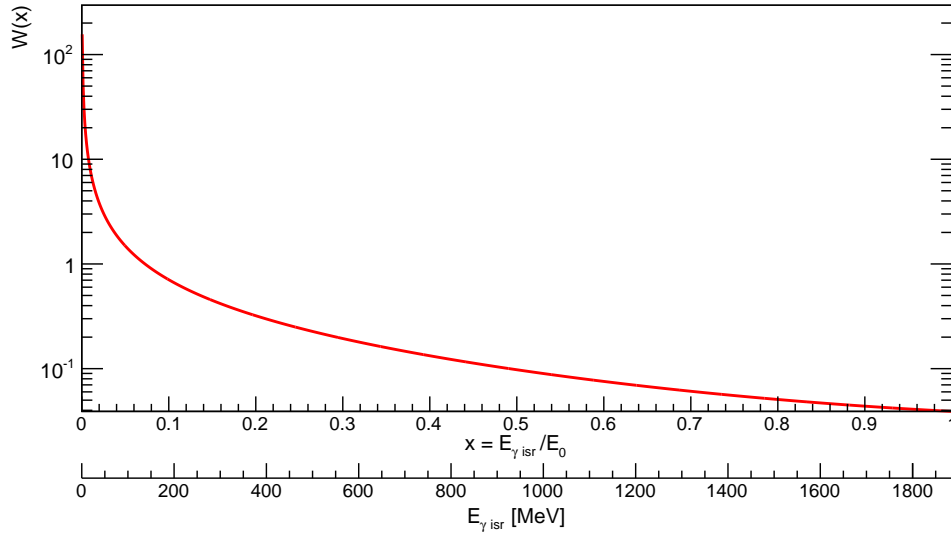


Fig. 3.4.: Logarithmic plot of the overall probability density for emitting a photon at $\sqrt{s} = 3770 \text{ MeV} = E_{\psi(3770)}$ with energy $E_{\gamma_{\text{ISR}}} = x \cdot E_0$ for all possible x values (Eq. (3.1.4)). The probability density decreases with increasing $E_{\gamma_{\text{ISR}}}$. Nevertheless, it is noticeable that even very large photon energies occur with a significant non-zero probability density. This allows measurements of the R -value for a wide energy range without changing the beam energies.

ISR has been known and used for radiative corrections on hadronic cross section measurements since the early seventies, but using ISR as a tool for certain measurements is a relatively novel approach. Originally thought to be an alternative to energy scans and very successfully proven as such in several experiments (e.g. BELLE, CLEO, BABAR, OPAL (CERN), KLOE), it also helps to clarify reaction mechanisms and to reveal substructures in terms of intermediate states and their decay mechanisms [54].

ISR techniques have furthermore been used for measurements of the hadronic contribution to the anomalous magnetic moment of the muon a_{μ}^{had} . Also the recently discovered $Y(4260)$ state was first seen by BABAR in an ISR process [55] via the reaction

$$e^+e^- \rightarrow Y(4260) \gamma_{\text{ISR}} \rightarrow J/\Psi \pi^+ \pi^- \gamma_{\text{ISR}} \quad . \quad (3.1.5)$$

The advantage of the ISR method over the direct energy scan method lies in the determination of systematic errors: In a direct energy scan the collider with all its electric and magnetic fields has to be adjusted for every scan point, even minor changes in the setup lead to changes in the systematic errors for the luminosity, the energy of

the electrons and positrons and the detection efficiencies. For the ISR method the error estimation only has to be done once for the whole spectrum at the cost of luminosity for each desired energy (see Eq. (3.1.4) and Fig. 3.4), keeping much better control over the systematics. Thus, the very high luminosity charm- and bottom-factories make ISR physics even more promising and exciting, since they still achieve high luminosities for processes involving photons from the initial state.

3.2. ISR Physics at BESIII

There are two possible approaches in order to analyze ISR events:

1. an *untagged* approach, where the ISR photon is not detected and the event is selected by requiring the recoil mass against the hadronic system to be close to zero and a
2. *tagged* approach, where the photon radiated from the initial state is detected inside a detector.

Because of systematic uncertainties arising from a strong sensitivity of the detection efficiencies to hadron angular distributions, the *untagged* approach is rather suitable for the measurement of events with well defined dynamics, in contrast to the *tagged* approach, where such correlations are rather small [53].

Remembering Eq. (3.1.3), the ISR photon distribution is peaked in the very forward region around $\theta = 0^\circ$ ($w_0(\theta, s, x) \propto \cos^4(\theta)$). In order to *tag* the photon, one either has to select rare events, where the ISR photon is emitted at a large angle and is detected in the EMC or one needs a calorimeter at a small angle in order to tag ISR photons emitted along the beam axis, a *zero degree calorimeter* (ZDC). This approach allows for much higher statistics, but also has to deal with huge background from Bremsstrahlung photons originating from elastic e^+e^- scattering.

One important part of the BESIII ISR program is the determination of R . The R value defined in Eq. (3.1.2) basically consists of measurements of the total cross section for e^+e^- annihilation into hadrons at different center-of-mass energies. These total hadronic cross sections are an important input for the determination of the non-perturbative hadronic contribution to the running of the QED fine structure constant, and thus, an essential input parameter in precision electroweak measurements [24]. R can be measured exclusively, which means every kinematically allowed channel is directly measured, R is then basically determined by the sum of all exclusive cross sections. For exclusive measurements, the ISR photon does not need to be tagged, since \sqrt{s}_{ISR} can directly be determined by measuring the energies of all particles. In view of the many channels in the BESIII energy region, an inclusive measurement seems advantageous. The ISR approach allows simultaneous measurement of the total

hadronic cross section at all energies up to \sqrt{s} with the accelerator running at a fixed \sqrt{s} . The huge luminosity of BEPCII provides data samples, which are large enough for precise R measurements. For inclusive measurements the determination of \sqrt{s}_{ISR} is of great importance. A ZDC measuring the energy of the ISR photon could be used for this purpose.

Measurements of the timelike nucleon form factors using ISR techniques are another major part of the BESIII ISR program, its great importance is repeatedly emphasized in the literature (e.g. [56–58] and references therein). A further physics goal of the BESIII ISR program is the cross section measurement at the $p\bar{p}$ threshold, where some experiments see an anomalous near threshold enhancement [39–42] in certain channels, often designated as the $X(1860)$, whereas other experiments do not observe such a behaviour [59–61]. Theoretical interpretations range from final state interactions between the proton and antiproton [62, 63], proton-antiproton bound states (baryonium) [64, 65] to exotic multiquark states [66] and glueballs [67]. Fig. 3.5 shows one measurement with and another without cross section enhancement at the $p\bar{p}$ threshold. At symmetric colliders like BESIII such measurements can only be done via ISR, because the additional Lorentz-boost will allow the nucleons to fly away from the vertex and be detected by BESIII. In an energy scan around the threshold the nucleons would be produced at rest and therefore would not be measurable.

Beside ISR physics the exclusive measurement of the $\gamma\gamma^* \rightarrow \pi^0$ transition form factor in the process $e^+e^- \rightarrow e^+e^-\pi^0$, similar to that done at BaBar [68], is another interesting physics measurement which could be done with a ZDC.

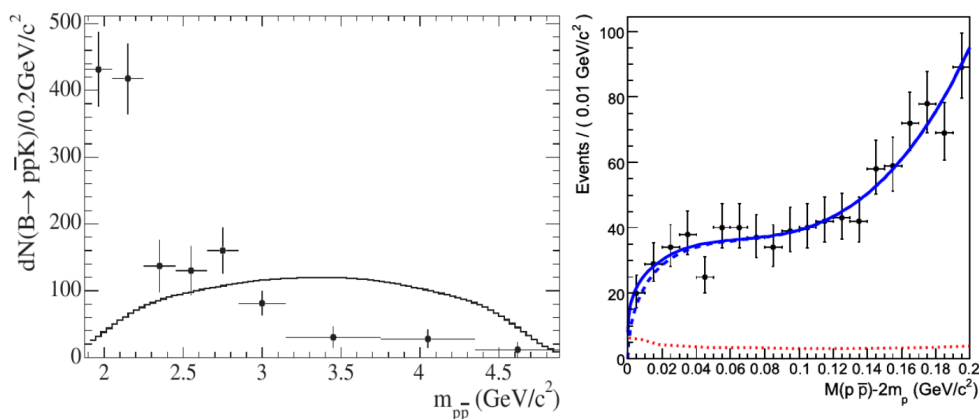


Fig. 3.5.: $p\bar{p}$ threshold measurements: The left plot shows an enhancement of $p\bar{p}$ at the mass threshold in B decays ($B \rightarrow p\bar{p}K$) measured by BaBar [41], whereas in the right plot J/ψ decays measured by BESII do not observe a corresponding mass threshold enhancement ($J/\psi \rightarrow p\bar{p}\omega$)[60], although it was seen in the $J/\psi \rightarrow p\bar{p}\gamma$ channel [39, 40].

ZERO DEGREE CALORIMETRY AT BESIII

Physics measurements including a photon from the initial state are rare, when the photon needs to be tagged at large angles in the EMC. If we could tag the photons at angles near $\theta = 0^\circ$, the measured ISR event rate would significantly increase by several orders of magnitude. This chapter contains a description of the current Zero Degree Detector (ZDD), the design of the future Crystal Zero Degree Detector (cZDD) upgrade including properties of the detector material and its readout, and the foreseen DAQ scheme for the cZDD.

4.1. Spatial Considerations

The region around the beam-axis $\theta = 0^\circ$ is covered with lots of structures, either beampipes, magnets or respective support structures. The only available space for a ZDC is located ± 3.35 m away from the interaction point, where the lead glass luminosity monitor is placed. This space is very limited (see Fig. 4.1), thus is the size of any ZDC. Therefore, an electromagnetic shower in the ZDC induced by an ISR photon might not be fully captured by the ZDC. From this point of view it is obvious that the resolution of any ZDC will be determined and limited mostly by the detector's geometry. Hence, any ZDC will more be like a sampling calorimeter with rather limited capabilities. Simulations investigating the capabilities of the cZDD will be explained in chapter 5.

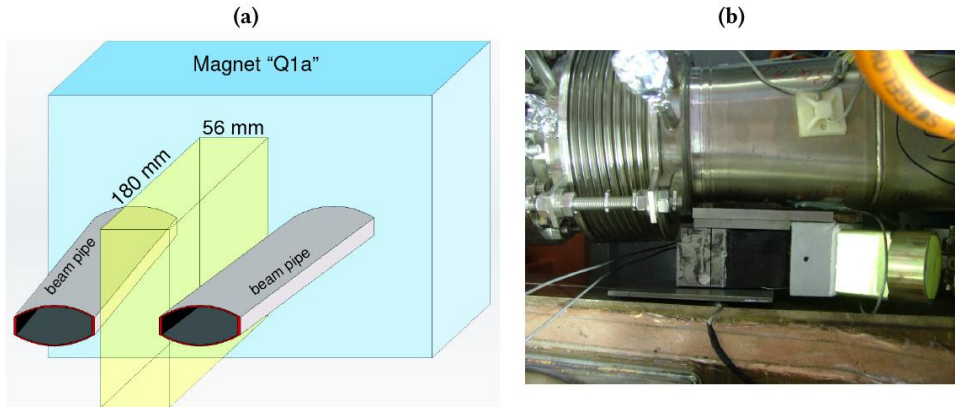


Fig. 4.1.: Spatial limitations for a ZDC [69]: (a) shows the available space for a zero degree calorimeter, which is confined by the beam pipes and a magnet. (b) provides a topview of the old lead-glass luminometer at the dedicated position.

4.2. The Zero Degree Detector (ZDD)

As explained in chapter 3, the angular distribution of ISR photons is peaked at very small angles around $\theta = 0^\circ$. The ZDD at BESIII [70] was installed in 2012 by the Italian INFN group in order to measure ISR photons and is placed at $\theta = 0^\circ$ in that very forward region of BESIII outlined above. The ZDD has been designed as a small sized Pb-SciFi calorimeter readout by several PMTs, placed outside the detector volume. Its structure consists of an alternating stack of 1 mm fibers glued between thin grooved Pb foils [70]. The detector is splitted into two identical modules with a 1 cm gap in between in order to reduce contamination from Bremsstrahlung photons from $e^+e^- \rightarrow e^+e^-\gamma$ reactions, which are much more peaked in the forward region than ISR photons (see [52, 70, 71]). A picture and a schematic view of one ZDD module showing the detectors segmentation can be seen in Fig. 4.2. The mechanical support structure of the ZDD allows for adjustments of the y -position of both modules, where y is the vertical coordinate perpendicular to the z -beam axis. It has been validated that the ZDD can clearly identify single bunches for luminosity monitoring, but offline correlation of ZDD data with BESIII data has not been possible yet since the BESIII trigger basically works as a random trigger, because events measured in the ZDD need not necessarily trigger an event in BESIII (e.g. Bremsstrahlung photons) and vice versa [72]. Additionally, for each BESIII trigger there are several ISR candidates and it is a highly non-trivial task to find the right one. The cZDD DAQ is planned to perform real time event correlation based on programmable algorithms running on FPGAs, which could solve this problem. Another drawback of the ZDD is the use of scintillating fibers, which are rather sensitive to radiation and probably will have

to be exchanged after a relatively short time of operation. The cZDD will consist of radiation hard lead-tungsten crystals, in which possible radiation damages can be recovered during operation by the use of ultrared light emitting diodes, which will not produce signals in the photodetectors [73].

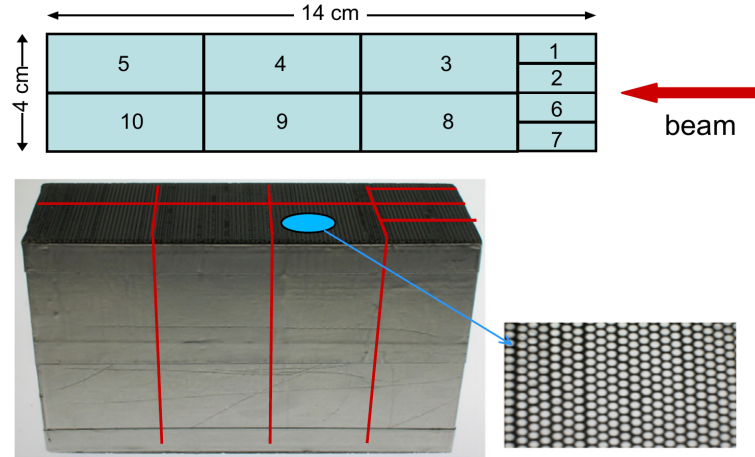


Fig. 4.2.: A schematic and a picture of a ZDD module showing its dimensions and longitudinal and transversal segmentation [70]. Each segment is read out by a PMT.

4.3. The Crystal Zero Degree Detector (cZDD)

The cZDD is planned as an upgrade of the current ZDD with an improved DAQ and improved capabilities for ISR studies. The cZDD design is based on crystals made of PbWO_4 arranged in two arrays of 4×3 crystals, each of 14 cm length with a quadratic end face of side length 1 cm, divided by a 1 cm gap for the same reason as mentioned in section 4.2. Fig. 4.3 shows the detector design and the center position of the crystals used for the simulation explained in chapter 5. Fig. 4.4 shows the energy distributions of several ISR photons and the corresponding angular region, which will be covered by the cZDD. Each crystal is read out by two Silicon Photomultipliers (SiPMs), whose signals will be digitized by a sampling ADC. Corresponding developments for its DAQ will be discussed in greater detail in chapter 6. Fig. 4.5 (a) shows a 400 MeV photon hitting the detector in a Geant4-based simulation in the BESIII Offline Software System (BOSS), explained in chapter 5, and the ISR angular distribution at the cZDD (b) for a given photon energy, calculated from Eq. (3.1.3). The position of the cZDD at BESIII can be seen in Fig. 4.6.

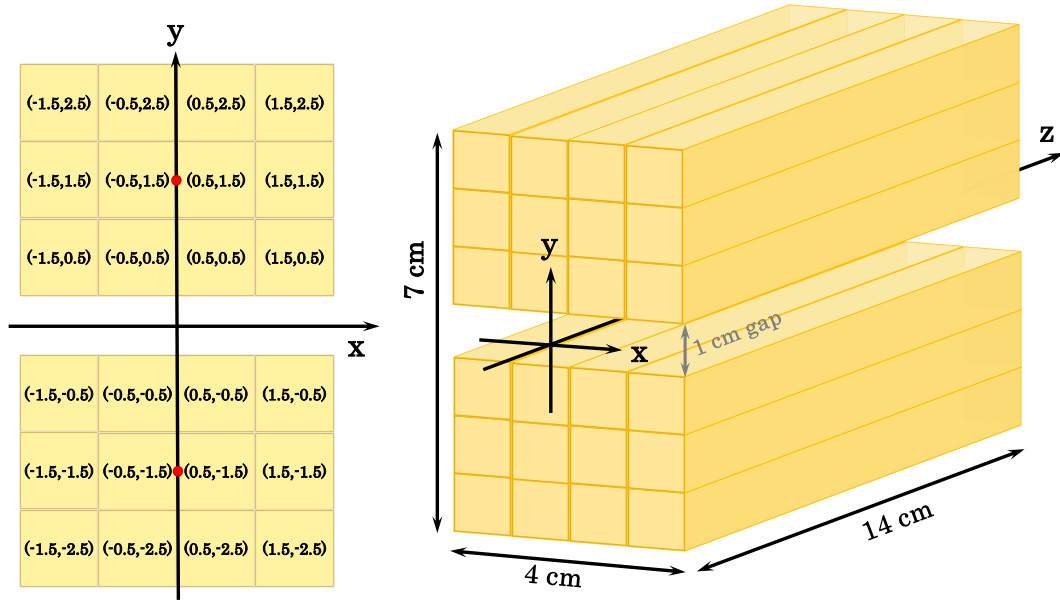


Fig. 4.3.: The foreseen design of the Crystal Zero Degree Detector to be installed as an upgrade of the existing Zero Degree Detector at BESIII. The picture on the left depicts a front view of the detector with (X,Y) coordinates of each crystal's center. The red dots mark the center of upper and lower detector part.

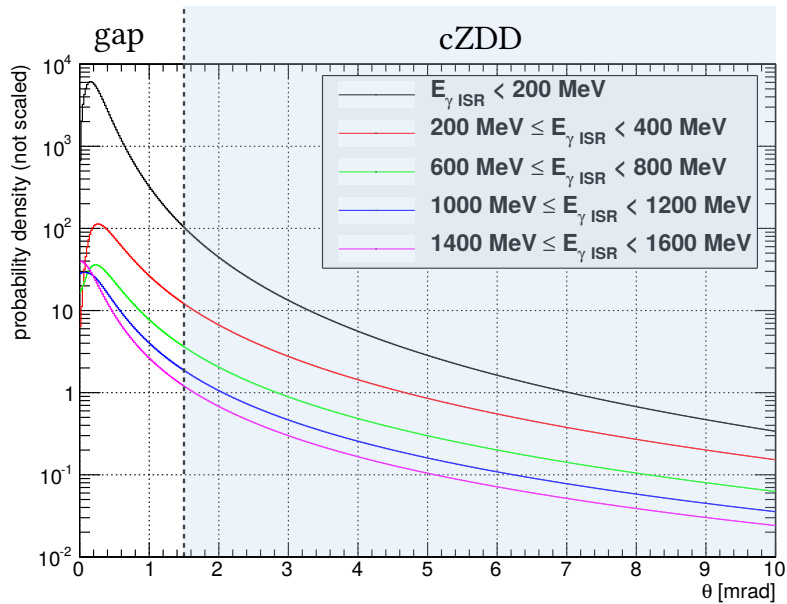


Fig. 4.4.: Eq. (3.1.3) from chapter 3 plotted in dependence of θ for several $E_{\gamma \text{ ISR}}$ regions ($\sqrt{s} = 3770 \text{ MeV}$). All distributions are peaked around 0° . The region, which is covered by the cZDD, is colored.

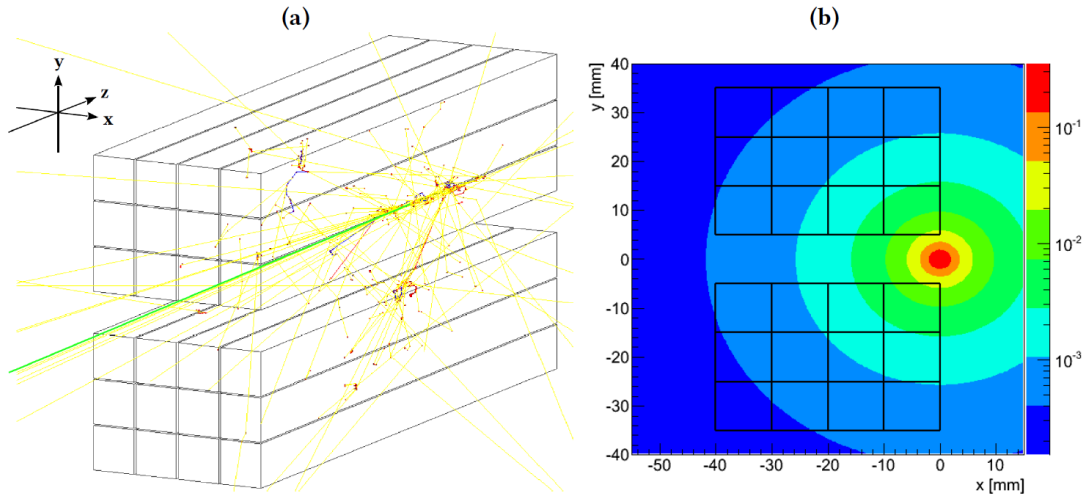


Fig. 4.5.: (a) The cZDD detector being hit by a 400 MeV photon simulated in Geant4. The green line represents the trajectory of the primary photon, red dots mark hits with non-zero energy deposition, blue and red lines indicate secondary electrons (red) and positrons (blue), yellow lines mark the trajectory of secondary photons. Plot (b) shows the angular distribution of ISR photons with given energy at the cZDD (derived from Eq. (3.1.3)), $(x,y) = (0,0)$ corresponds to the maximum of the photon distribution (and not the z -axis of the detector). The right-shift comes from the non-zero crossing angle and the resulting boost of the center-of-mass frame.

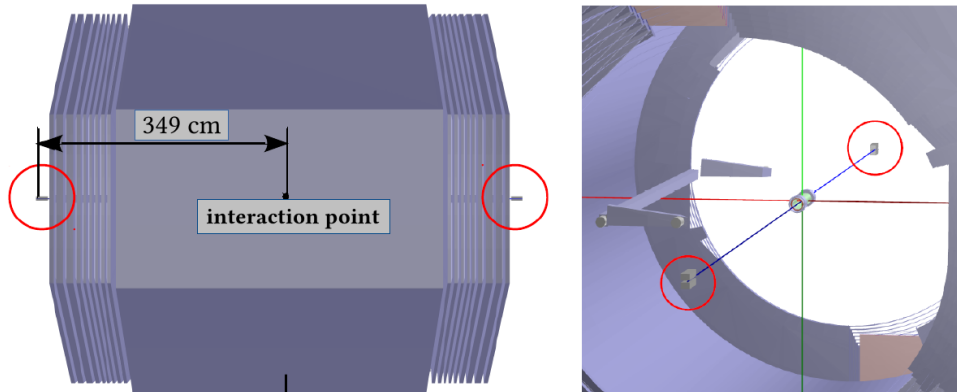


Fig. 4.6.: View of the cZDD geometry implemented into BOSS. Two cZDD modules are placed ± 349 cm in each direction from the interaction point. The picture on the right also shows the implementation of the beam pipe, which is not done for the very forward/backward region. This has to be implemented for studies of beam pipe influences on the cZDD's capabilities. Inner detectors have been switched off in order to get a clearer illustration.

4.3.1. PbWO₄ crystals

The lead tungsten crystals to be used for the cZDD have not been produced yet. For first tests of a prototype detector, a crystal similar to those of the cZDD has been used. It has the same properties as the $\bar{\text{P}}\text{ANDA}$ EMC crystals described in chapter 2.1, but has a different geometry. For getting an idea which crystal sizes can be produced from $\bar{\text{P}}\text{ANDA}$ EMC prototype crystals, some have been cut into smaller crystals. The crystal chosen for the prototype setup has a quadratic cross section of $1.5 \times 1.5 \text{ cm}^2$ and a length of 15 cm (see Fig. 4.7). It is slightly bigger and longer than the crystals foreseen in the cZDD design. The crystal is wrapped in teflon and reflecting aluminum foil in order to minimize the scintillation light loss due to photon escape. Shrinking hoses are used for sealing the crystal off from ambient light. Two SiPMs are diagonally mounted on the crystal's endface for readout. The next section will summarize the main properties of SiPMs.



Fig. 4.7.: (a) A prototype $\bar{\text{P}}\text{ANDA}$ EMC crystal cut into several smaller crystals. As can be seen, the smaller crystals easily break, therefore a bigger one (b) has been chosen for the prototype detector .

4.3.2. Silicon Photomultipliers

4.3.2.1. General Principle

In order to allow count rates in the order of several *MHz*, very fast SiPMs are chosen as photodetectors for the scintillator readout. A SiPM basically consists of many parallelly wired, reverse-biased avalanche photopixels operated in Geiger mode: Each pixel of the SiPM is operated with a reversed bias voltage slightly above the pixel's breakdown voltage. If a scintillation photon creates an electron-hole pair (EHP) in the depletion region of a pixel, the carriers will be accelerated by the bias voltage and create an avalanche of secondary EHPs. This process only depends on the applied bias voltage and is (almost) independent from the photon's or particle's initial energy,

resulting in a defined signal output for one firing pixel. Any pixel traversing photon or particle creating an EHP will produce the same signal output. When a pixel is firing, the pixel will be discharged by a serially connected quenching resistor lowering the bias voltage and stopping the avalanche process. Therefore each pixel has an intrinsic dead-time, also named as *recovery time*, where the pixel is not sensitive to incoming photons or particles until all charge is collected and the bias voltage is reset to its initial value. The principal structure of a SiPM can be seen in Fig. 4.8. With this principle, very high intrinsic amplifications ($10^5 - 10^7$) are achievable [74]. By operating many parallelly-wired pixels inside one SiPM, the output signal will consist of a superposition of all firing single pixel signals, allowing for an output signal proportional to the number of scintillation photons and therefore proportional to the energy deposited in the scintillator.

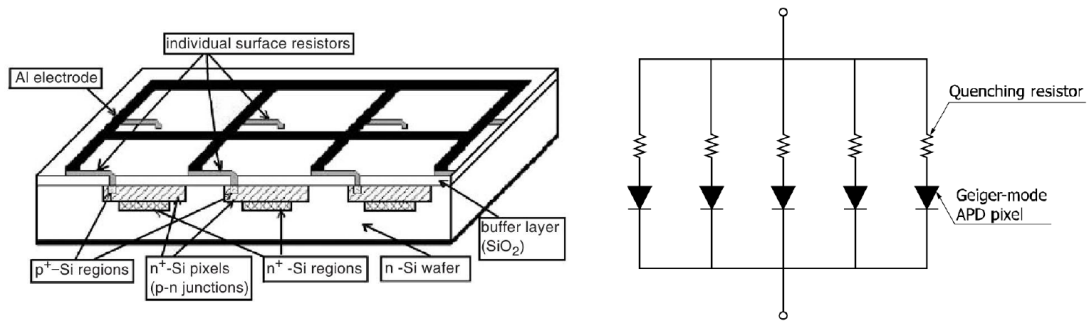


Fig. 4.8.: Principal structure of a SiPM: Many pixels are operated in Geiger-mode parallelly, each pixel has its own serially connected quenching resistor. The left picture shows the basic technical structure of a SiPM [75]. The principal electric circuit of a SiPM can be seen in the right picture [76]. The output signal consists of a superposition of all firing pixel signals allowing for an output proportional to the number of incoming photons.

4.3.2.2. Properties

Silicon photomultipliers have several properties, which make their use advantageous compared to standard photomultipliers:

SiPMs require low voltages to operate (< 100 V) and are insensible to magnetic fields up to 15 T. Furthermore they have a great quantum efficiency of 25 - 75% (depending on purpose and type of SiPM) and very good timing properties (500 - 600 ps FWHM). They allow for single photon counting, have a low response to passing ionizing particles, e.g. protons or heavy ions, are radiation hard and mechanically robust and can be produced by mass production technology, which potentially makes them cheap.

Nevertheless, SiPMs also have some undesired properties which need to be considered during operation. The next sections will summarize undesired effects caused by the SiPM's intrinsic structure and operation principle.

Dark Counts

Since SiPMs are operated with a bias voltage above the breakdown voltage, EHPs can also be generated thermally or by tunneling effects (field-assisted generation). This results in so-called *dark counts* with rates from 100 *kHz* up to several *MHz* per mm^2 sensitive area [74]. Thermally generated free carriers can be reduced by cooling, the field-assisted generation can only be diminished by decreasing the bias voltage. Since the dark counts are randomly distributed over time, a large amount of this noise can be filtered out by using at least two SiPMs and creating a logic, which only passes on the signals when more than one SiPM is outputting a signal above an adjustable threshold. See section 6.1 for details.

Optical Crosstalk

During an avalanche breakdown an average of 3 photons above $E_\gamma = 1.14 \text{ eV}$ (band gap of silicon) per 10^5 carriers are emitted [74]. These photons can propagate within the device and might get absorbed in the sensitive volume of a different cell, thus triggering another breakdown [77]. This process is known as *optical crosstalk* and is depicted in Fig. 4.9. Eventually, optical crosstalk acts like shower fluctuations introducing an excess noise factor like in a regular Avalanche Photodiode (APD). Since the number of carriers and therefore the production of secondary photons is gain dependent, the effect can be reduced by diminishing the bias voltage. Another advantageous approach uses designs with grooves between individual cells, which act as optical barriers [74, 77].

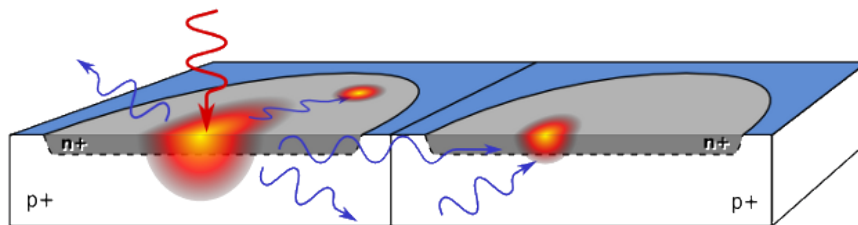


Fig. 4.9.: Optical cross talk inside a SiPM: A secondary photon created in an avalanche of a cell propagates through the device and triggers another pixel breakdown [78].

Afterpulses

During an avalanche some of the carriers can get trapped inside the lattice structure of the detector and be released with a delay. When such a trapped carrier is released and triggers a pixel breakdown with no incident photon hitting the cell, we speak of an *afterpulse*. Afterpulses are caused by impurities, which can trap the carriers inside the sensitive volume of the detector. Afterpulses can only be diminished by reducing the impurities inside the device during the manufacturing process.

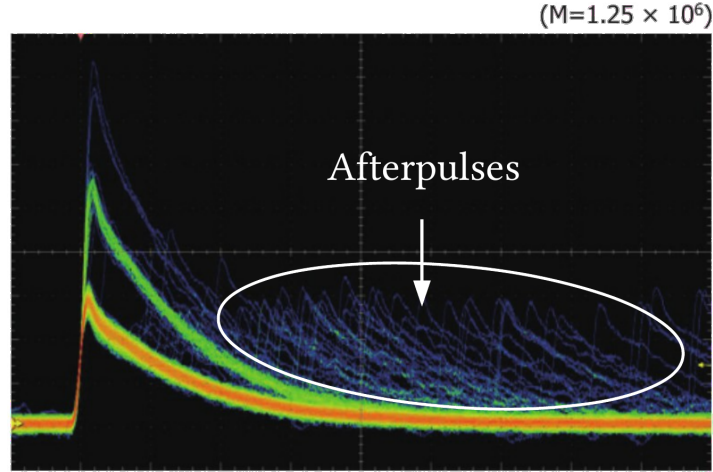


Fig. 4.10.: Afterpulses of a SiPM: The main signal is followed by a series of afterpulses, which are caused by the delayed release of trapped carriers, which then trigger a pixel breakdown [76].

Dynamic Range

As mentioned before, a SiPM produces a signal proportional to the number of incoming photons. This is only true as long as the number of incident photons N_{photons} is significantly smaller than the number of pixels N_{total} inside the SiPM. The reason is that the probability of multi-hits per cell increases with increasing number of incident photons, leading to an output signal

$$A \approx N_{\text{fired cells}} = N_{\text{total}} \cdot \left(1 - \exp \left[-\frac{N_{\text{photons}} \cdot \text{PDE}}{N_{\text{total}}} \right] \right) , \quad (4.3.1)$$

with PDE being the photodetection efficiency of a single cell. Using a SiPM with 3600 pixels and a PDE of 50%, there is more than 10% deviation from linearity, when N_{photons} is exceeding 50% of N_{total} . This intrinsic saturation effect leads to a logarithmic compression for large signals, increasing the dynamic range of the detector at the cost of signal resolution. The response function showing the logarithmic compression of different SiPMs can be seen in Fig. 4.11.

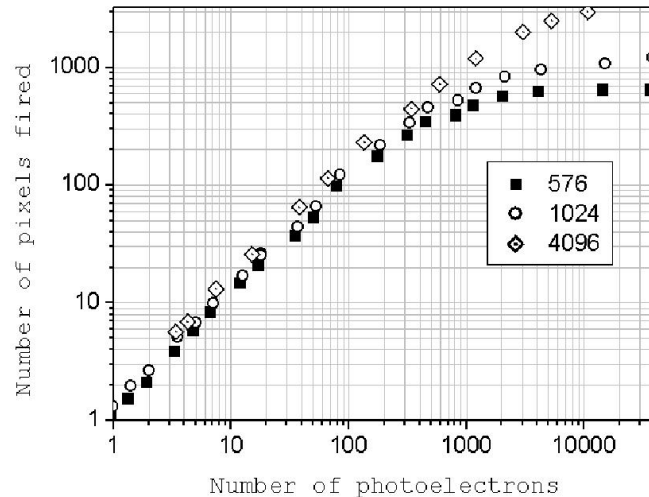


Fig. 4.11.: Plot showing response functions of three different SiPMs with 576, 1024 and 4096 pixels as a function of the number of produced photoelectrons (from [79]). The SiPM with the least number of pixels shows logarithmic compression much earlier than the one with 4096 pixels.

All mentioned effects worsen the signal resolution of the SiPMs, resulting in an effective resolution below the theoretically expectable values.

4.3.2.3. Specific Properties of Hamamatsu S10931-050P MPPCs

For the readout of the lead-tungsten crystal, Hamamatsu MPPCs from the S10931 series have been chosen. Their effective active area, which is the area occupied by the pixels, is $3 \times 3 \text{ mm}^2$, the number of pixels on the device needs to be chosen for the specific application. When dealing with low photon fluxes, the single pixels should be large in order to increase the fill factor, which is the true photon sensitive part of the effective area. For scintillator readout one should use more and smaller pixels in order to reduce the multi-hit probability of a cell. The MPPC S10931 series consists of SiPMs with three different pixel sizes: $25 \times 25 \mu\text{m}^2$ (S10931-025P), $50 \times 50 \mu\text{m}^2$ (S10931-050P) and $100 \times 100 \mu\text{m}^2$ (S10931-100P). In order to optimize the performance of our setup, the S10931-050P model which has a good balance between number of pixels and fill factor was chosen. The main properties of the S10931-050P model are summarized in Tab. 4.1. Fig. 4.12 shows that the properties of lead tungsten and of the MPPCs fit together well regarding scintillation light spectrum and wavelength sensitivity, making the MPPC a suitable photodetector for the PbWO_4 crystal readout.

Effective active area	$3 \times 3 \text{ mm}^2$
Number of pixels	3600
Pixel size	$50 \times 50 \mu\text{m}^2$
Fill factor	61.5 %
Spectral response range	320 - 900 nm
Peak sensitivity wavelength	440 nm
Dark counts	6 - 10 Mcps
Time resolution	500 - 600 ps
Gain	7.5×10^5

Tab. 4.1.: Important properties of the Hamamatsu S10931-050P MPPC at room temperature ($T=25^\circ \text{ C}$) [80].

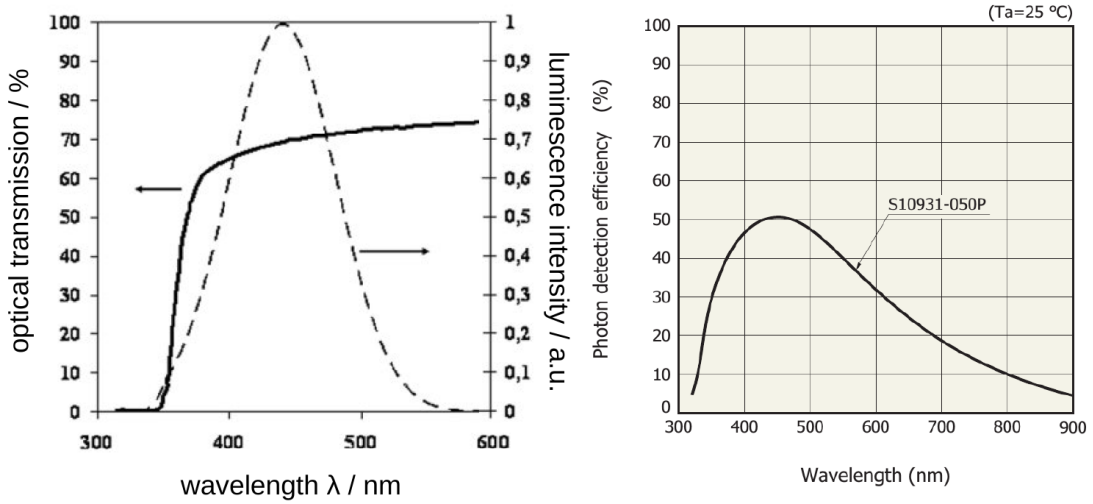


Fig. 4.12.: Scintillation light spectrum of PbWO_4 [13] and photon detection efficiency of S10931-050P MPPC [80]. Important is the peak sensitivity wavelength of the MPPC, which is near the spectral maximum of the PbWO_4 scintillation light (also see Tab. 2.1 and Tab. 4.1).

4.3.2.4. MPPC Preamplifier and Prototype Mechanics

The MPPCs are coupled to the readout surface of the crystal with silicone oil, which has a refractive index of about 1.5, reducing the amount of scintillation light, which gets lost due to reflection at the material surfaces. The MPPCs are mounted on a small board and each is directly connected to a preamp (AMP 0604 manufactured by Photonique), which delivers the bias voltage and the readout circuit for the SiPMs. The amplification can be adjusted by altering the supply voltage of the board. The preamps are installed inside a little aluminum box, which was constructed and built by the technical workshop. During measurements, the box is fixed on the crystal with a

shrinking tube, which allows for mechanical stability of the setup. The fully assembled box containing the MPPCs and the preamps is shown in Fig. 4.13.

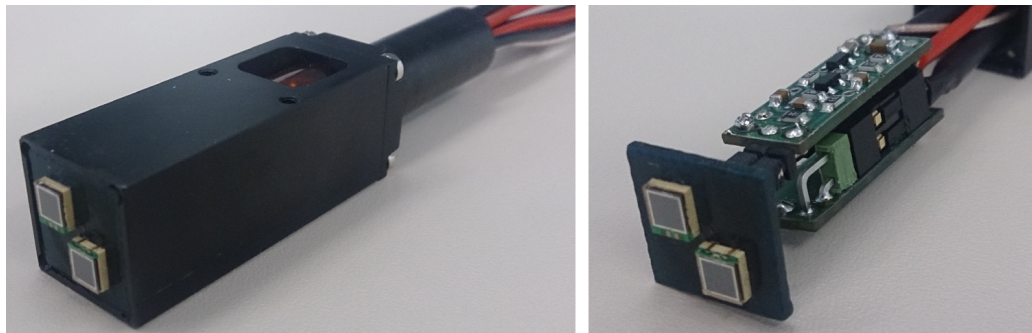


Fig. 4.13.: Hamamatsu MPPCs and the fully assembled box containing the preamps.

4.3.3. Foreseen cZDD DAQ scheme

As already mentioned, the cZDD DAQ is supposed to provide correlation between cZDD and BESIII data in real time. For this purpose the data from the cZDD is gathered for subevent building on the ADC. The subevent data is sent to the CN and buffered until information from the BESIII trigger is available. Based on programmable event selection criteria, the Compute Node (CN) can then filter out background and assign unique event numbers to correlated events. If correlated events have been found, the data can be sent to the BESIII DAQ for further processing. A scheme for the cZDD DAQ can be seen in Fig. 4.14. The details of the event correlation algorithms need to be worked out on a basis of what the BESIII trigger can provide. The hardware foreseen to be used for the DAQ is described in the chapter 6.

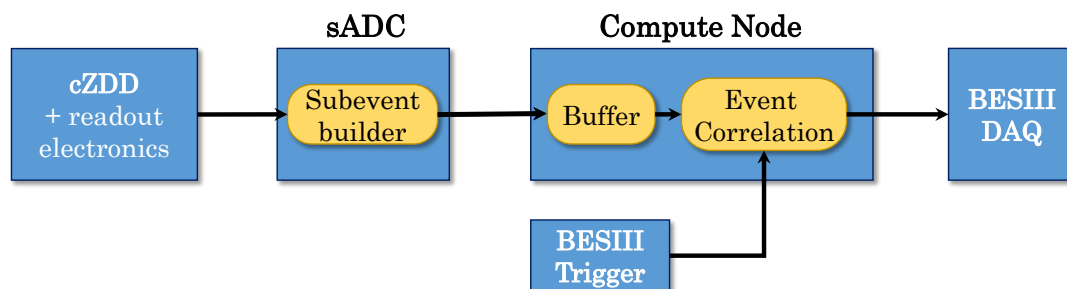


Fig. 4.14.: Schematic DAQ chain for the cZDD readout.

SIMULATIONS OF THE CRYSTAL ZERO DEGREE DETECTOR

Simulations of the cZDD's capabilities concerning energy resolution and determination of \sqrt{s}_{ISR} are described in this chapter. For this purpose the geometry and the properties of the cZDD explained in chapter 4 have been implemented into the Geant4-based BESIII Offline Software System (BOSS) in order to simulate ISR events measured with the cZDD.

Since the cZDD is a calorimeter measuring electromagnetic showers induced by ISR photons, the physics of electromagnetic showers and the interaction of photons with matter is briefly outlined.

5.1. Physics of Electromagnetic Showers

First observed in cosmic ray interactions in 1933, the reconstruction of electromagnetic showers has become a common task in medium and high energy physics. Photons have three options to interact with matter:

1. **Photo effect:** The photon is absorbed by an electron, which further interacts inside the medium.
2. **Compton effect:** The incident photon transfers part of its energy to an electron. Photon and electron can further interact with the medium.
3. **Pair production:** In presence of an atomic nucleus, and if the photon's energy is bigger than $2 \cdot m_e c^2$, the photon can create an electron-positron pair, which again strongly interact with matter.

As Fig. 5.2 (a) shows, pair production becomes the dominating process for energies above a few MeV, which is mostly the case for high energy physics calorimetry. When

electrons/positrons are created, they mainly interact with surrounding matter by ionisation processes, or if their energy exceeds the critical energy [81]

$$E_c \approx \frac{800 \text{ MeV}}{Z + 1.2} \quad , \quad (5.1.1)$$

by the emission of Bremsstrahlung photons, which are a source of additional electron-positron pairs. Thus, a whole cascade of secondary electrons and positrons with decreasing energy will build up until the energy falls below $2m_e c^2$. The evolution of an electromagnetic shower can be described by a circular diagram depicted in Fig. 5.1.

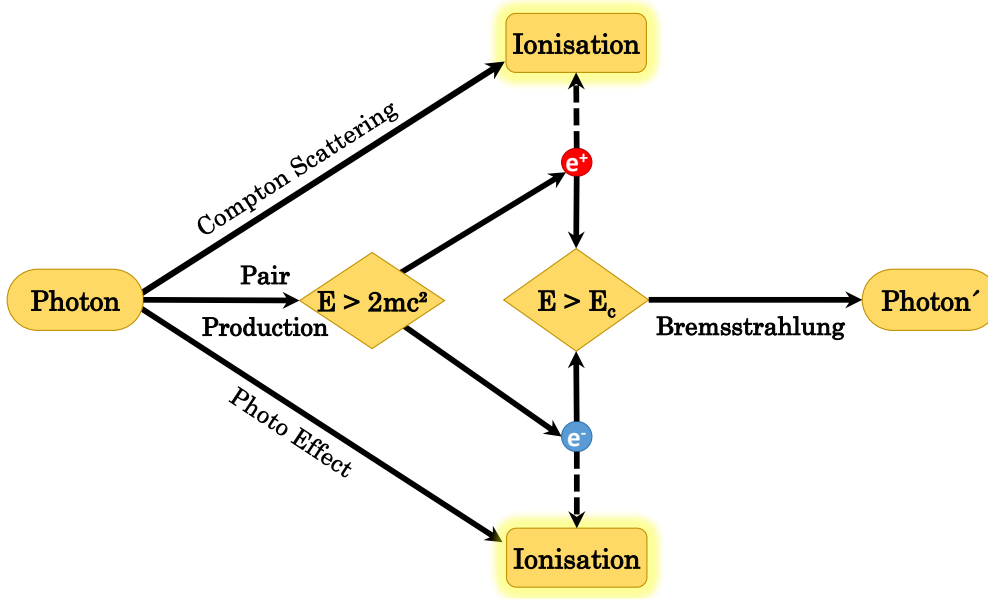


Fig. 5.1.: Circular diagram of the evolution of an electromagnetic shower. In a first approximation the shower stops, when the electron/positron energy drops below the critical energy [81].

Fig. 5.2 (b) shows the different sources for the fractional energy loss of electrons/positrons in lead per radiation length X_0 , which is the mean path length, after which the particle has only $1/e$ of its initial energy. It can be calculated for electrons in a material of atomic number Z and mass number A using

$$X_0 = \frac{716.4 \cdot A}{Z(Z + 1) \ln \left(\frac{287}{\sqrt{Z}} \right)} \left[\frac{\text{g}}{\text{cm}^2} \right] \quad , \quad (5.1.2)$$

an analogue parameter for high energetic photons, where only pair production is considered, can be defined as

$$\Lambda = \frac{9}{7} \cdot X_0 \quad , \quad (5.1.3)$$

which is called the interaction length, after which the number of incoming photons has been reduced by a factor of $1/e$. From the Z dependence of E_c it is obvious that a high

Z detector material corresponds to a low E_c , which makes the detector more sensitive to a full energy deposition. X_0 and Λ can then be used as scaling factors determining the size of the absorber volume, which completely contains the electromagnetic shower. Unfortunately it can not be applied to the ZDD geometry, since the available space in the very forward/backward region of BESIII (see Fig. 4.1) is the limiting factor for the detector volume.

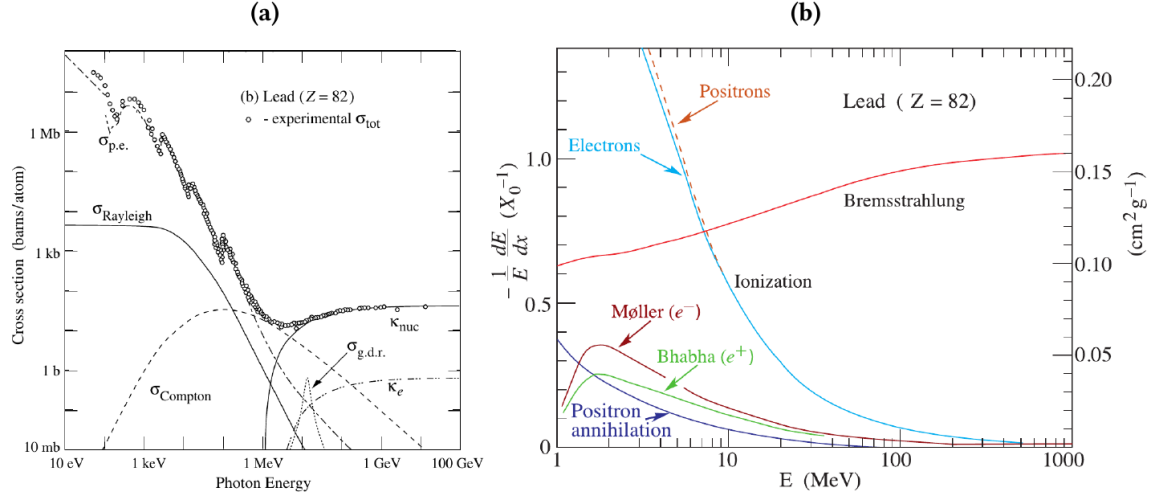


Fig. 5.2.: (a) Cross sections for the different photon interaction processes in dependence of the photon energy. Pair production (depicted as κ_{nuc} and κ_e) becomes dominating above a few MeV [82]. (b) Fractional energy loss per radiation length (X_0) in lead as a function of electron/positron energy [82].

5.2. Geant4-based Simulations of the cZDD

5.2.1. The BESIII Offline Software System (BOSS)

The BESIII Offline Software System (BOSS) [83] is the framework in which all relevant BESIII detectors, mechanics and support structures are fully implemented for simulation purposes. It contains various physics generators for simulating charmonium production and subsequent decays, algorithms for simulating accurate detector responses and reconstruction algorithms (e.g. dE/dx measurements in the MDC, track finding with MDC hits, track matching with hits from outer lying detectors, etc.). Furthermore, several analysis tools for kinematic fitting, vertex determination and particle identification (PID) are available. BOSS is based on C++, GAUDI [84] and the Geant4 simulation toolkit [85], parts of its source code were taken from existing CERN, BaBar and Belle code. For simulation purposes the cZDD has been implemented into BOSS, which is described in the next sections.

5.2.2. Implementation of the cZDD into BOSS

Geant4 takes care of all particle interactions with magnetic and electric fields, detector material and also of interactions with those supporting structures, which have been implemented into the BOSS framework. If a volume is declared as sensitive, then all relevant information of the particle's interactions inside the volume (e.g. energy deposition, particle trajectories, secondaries, etc.) is stored in so-called *hits*. The user decides, which information is relevant for the further simulation, each hit stores the Monte Carlo truth (MC truth) of the relevant parameters. These hits build the base for the *digitization* process, where the MC truth of the hits is converted into realistic detector signals, so-called *digis*, taking into account material properties, photodetectors and the signal generating electronics. An *identifier* module then converts these digis into a raw-data format, equal to that of real data. From this point on, reconstruction and analysis algorithms can be used for data evaluation. The geometry of the cZDD as described in section 4.3 has been implemented into BOSS, the numbering scheme of the crystals, the relevant classes providing the information of the detector hits and digis and the identifier module have been defined, see Appendix A. Since the cZDD had been a completely new detector module in BOSS (and not a replacement of an existing detector), the interface to the BOSS framework and its datahandling services also had to be implemented. The process of digitization mentioned above is outlined in the next section.

Digitization - From MC Truth To Realistic Detector Output

Digitization is the most complicated part of the simulation, since it needs to include all physically relevant processes to create a realistic detector output, but also needs to be sufficiently fast to allow a smooth simulation procedure and an appropriate simulation duration.

The implementation of the digitizer module is based on a description found in [86], where a digitizer module for a plastic TOF scintillator is explained. The simulation creates objects called "photons" whenever energy is deposited in the sensitive volume of the detector. These are not photons in a physical sense, but objects with certain properties as production time, scintillation time, trapping angle θ and an origin position, further explained later. These photons need to be propagated through the crystals and then be converted into an electric current by a photosensitive detector. Fig. 5.3 shows a block diagram of the digitization program.

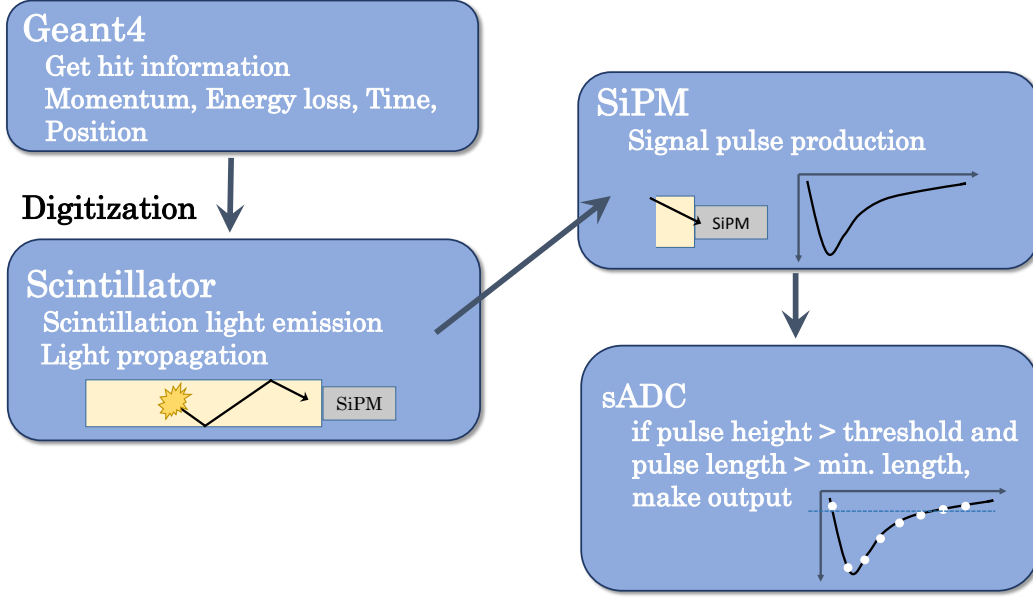


Fig. 5.3.: Block diagram of the simulation program, based on [86].

As described in [85], Geant4 calculates particle interactions in terms of energy loss, secondary generation, etc. step by step. The energy deposited between preStep- and postStep-point is assumed to be uniformly distributed along the track path, this is done by throwing uniformly distributed random numbers $\xi \in [0; 1]$. The difference between postStep-point \vec{X}_{post} and preStep-point \vec{X}_{pre} is $\vec{\Delta} = \vec{X}_{\text{post}} - \vec{X}_{\text{pre}}$, the time difference is $\Delta t = t_{\text{post}} - t_{\text{pre}}$ respectively. The photon is created at the position

$$\vec{X}_{\text{prod}} = \vec{X}_{\text{pre}} + \xi \cdot \vec{\Delta} \quad \text{with production time} \quad (5.2.1)$$

$$t_{\text{prod}} = t_{\text{pre}} + \xi \cdot \Delta t \quad . \quad (5.2.2)$$

The number of created photons p_c is proportional to the energy deposition and needs to be tuned in a way that the number of photons generating the signal in the SiPM is almost the same as in a realistic experimental setup. For the simulation it was chosen to be 200 (before any cuts are applied), this number needs to be tuned to experimental data, which is not available yet. It was chosen by estimation and would leave ~ 13 photons/MeV in a PMT with quantum efficiency of 22%, which is a rather conservative definition for p_c .

In order to get a realistic photon timing, the photon gets another property: the emission time of the photon t_{emit} , which is the scintillation decay time of PbWO_4 . PbWO_4 has fast and slow scintillation components. For the simulation the following parameters were chosen: $\tau_{f_1} = 6.4$ ns, $\tau_{f_2} = 6.5$ ns (97%) and $\tau_s = 30.4$ (3%).

t_{emit} is distributed as

$$f(t) = \frac{1}{1+R} \left(\frac{e^{-t/\tau_{f2}} - e^{-t/\tau_{f1}}}{\tau_{f2} - \tau_{f1}} + \frac{R}{\tau_s} e^{-t/\tau_s} \right) , \quad (5.2.3)$$

where $R = 3/97$ is the ratio between the slow and fast components. Practically, the t_{emit} variable was generated using a random variable following the distribution function of Eq. (5.2.3).

Once the photons have been created they need to be propagated through the scintillator. Some of the photons reach the SiPM, some are trapped because of endless reflection and subsequent attenuation, some escape from the scintillator and others get absorbed in the material, since the transmission probability for scintillation light is not 100%. An overview of these processes can be seen in Fig. 5.4. The θ angle of the photon is determined by shooting an uniformly distributed random variable between 0 and 90. By assuming perfect internal reflection on each of the four surfaces of the PbWO_4 crystals, the light propagation length

$$l_{\text{prop}} = \frac{d}{\cos \theta} \quad (5.2.4)$$

can be calculated, where d is the distance from the light emission position to the end surface of the scintillator and θ is the polar angle of the emitted photon (see Fig. 5.4).

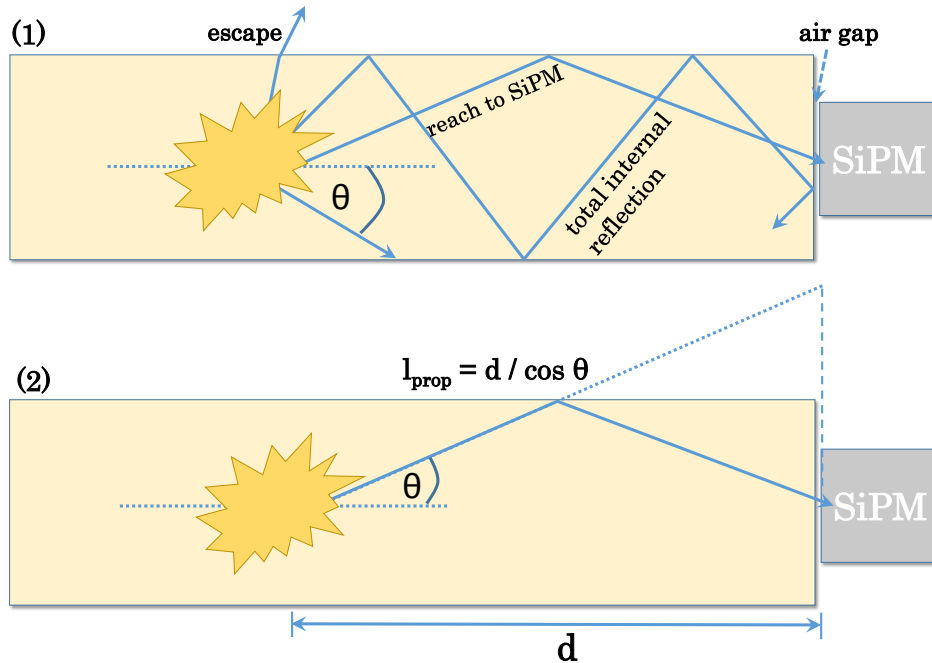


Fig. 5.4.: Photon propagation in a scintillator, based on a description found in [86]. (1) shows different sources of scintillation photon loss, (2) shows the derivation of the photon propagation length.

It was assumed that photons with an emission angle smaller than the trapping angle

$$\theta_{\text{trap}} = \sin^{-1} \left(\frac{n_{\text{air}}}{n_{\text{PbWO}_4}} \right) = \sin^{-1} \left(\frac{1.0003}{2.2} \right) \approx 27.04^\circ \quad (5.2.5)$$

can traverse the air gap between scintillator and SiPM, while all other photons get lost by escape or total internal reflection. l_{prop} , which can be derived from Fig. 5.4, determines the attenuation probability inside the scintillator material, which is simulated according to

$$R(l_{\text{prop}}) = e^{-l_{\text{prop}}/\lambda_{\text{prop}}} \quad (5.2.6)$$

with $\lambda_{\text{prop}} = 400$ cm being the characteristic length, after only $1/e$ of all photons have survived. In the simulation this is done by calculating $R(l_{\text{prop}})$ and then shooting a uniformly distributed random variable $\Xi \in [0; 1]$. If $\Xi > R(l_{\text{prop}})$, the photon is lost by attenuation. Given the propagation length l_{prop} , the light propagation time

$$t_{\text{prop}} = \frac{l_{\text{prop}}}{v_{\text{PbWO}_4}} = \frac{l_{\text{prop}}}{c/n_{\text{PbWO}_4}} \quad (5.2.7)$$

can be calculated.

Another source of photon loss is the mismatch of read-out surface and detector area of the SiPMs. The last photon reducing factors are the SiPM's fill factor, which describes the ratio of photosensitive area to total detector area and was set to 61.5% [80], and the quantum efficiency of the SiPM, which is $\sim 50\%$ [80], based on Tab. 4.1 already shown in chapter 4. Table 5.1 shows a summary of all important photon reducing parameters of the simulation.

Variable	Remaining photons after cut [%]
θ	30 (= 27°/90°)
$R(l_{\text{prop}})$	$e^{-l_{\text{prop}}/\lambda_{\text{prop}}} \cdot 100$
SiPM active Area	$2 \times 0.09 \text{ cm}^2 / 1 \text{ cm}^2 = 18$
SiPM Fill Factor	~ 61.5
SiPM Quantum Efficiency	~ 50

Tab. 5.1.: Summary of all important photon-reducing parameters used for the simulation.

Important for the resulting pulse of the SiPM is the arrival time of the photons

$$t_{\text{photon}} = t_{\text{prod}} + t_{\text{emit}} + t_{\text{prop}} \quad (5.2.8)$$

The single spectra of the times in Eq. (5.2.8) for one event and crystal can be seen in Fig. 5.5.

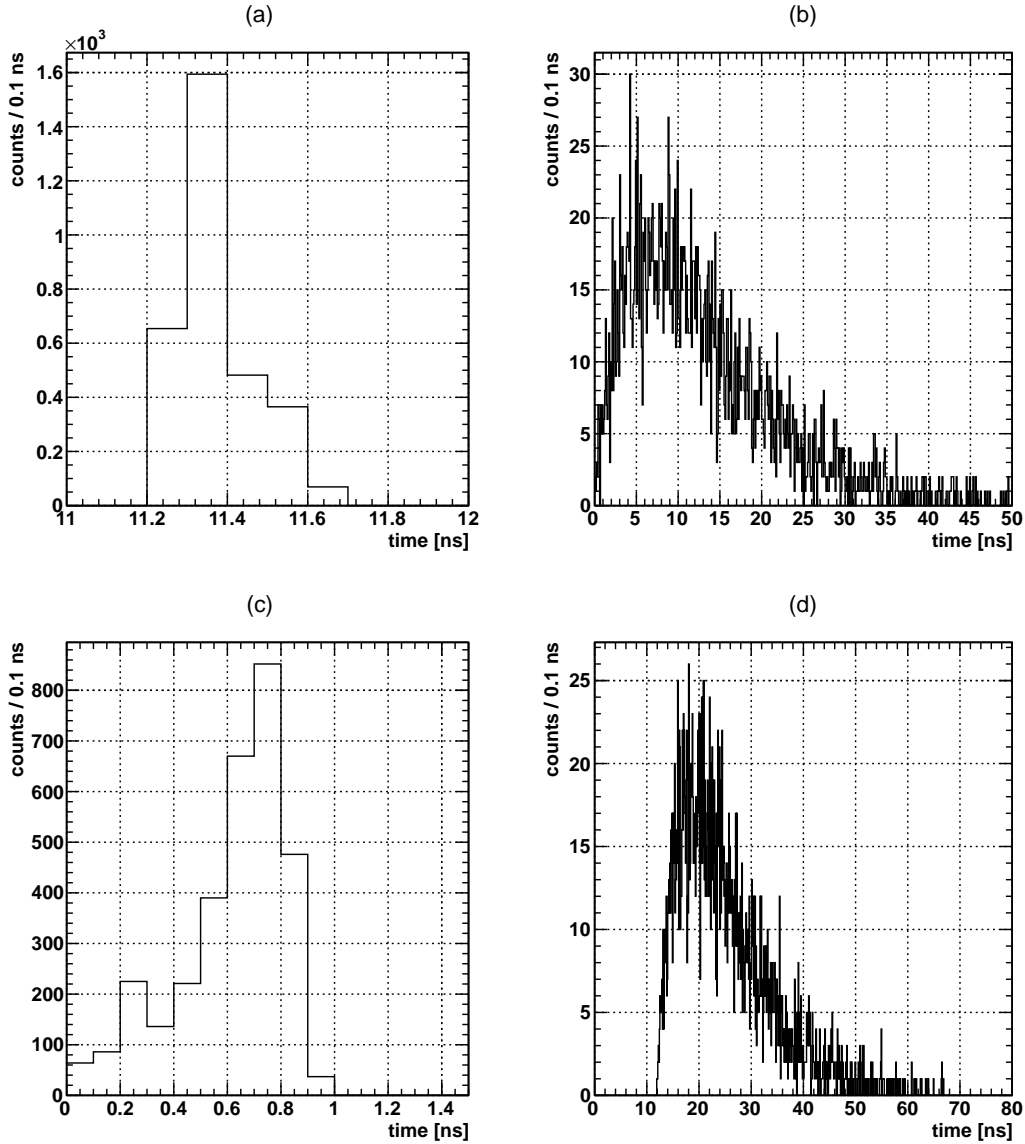


Fig. 5.5.: Plots showing the corresponding times from the simulation: **(a)** shows the distribution of t_{prod} (t_0 is the time, when the photon is created at the vertex), **(b)** depicts the spectrum of t_{emit} . The propagation time spectrum t_{prop} is plotted in **(c)**. Finally, the arrival time of the photons at the scintillator's endface, which is the sum of all times, is depicted in **(d)**. Each of the arriving photons can trigger a pixel breakdown, the resulting signal is the time-ordered superposition of all firing single pixel signals (see Fig. 5.6).

According to Eq. (4.3.1), not every incident photon triggers a pixel breakdown. This depends on the number of incoming photons, because of a rising probability for multihits per sensitive cell when increasing the number of incident photons. The

properties of SiPMs have already been explained in chapter 4. The SiPM output pulse was generated by a time-ordered linear superposition of single pixel signals triggered by the remaining photons. The underlying single pixel signal can be seen in Appendix A.2, which was parameterized with two exponential functions, similar to those for charging and discharging of a capacity. The simulated output pulse can be seen in Fig. 5.6, as well as the sampling points the sADC would see for this pulse. The resulting charge channel is consequently the addition of all sample points, which corresponds to the integral (=charge) of the pulse. At this point it should be mentioned that a simple linear superposition of single pixel signals will not really result in a realistic detector output. It is a first approximation, but the internal structure and the physical principle of the SiPMs introduce nonlinearities, which were not taken into account in this simulation.

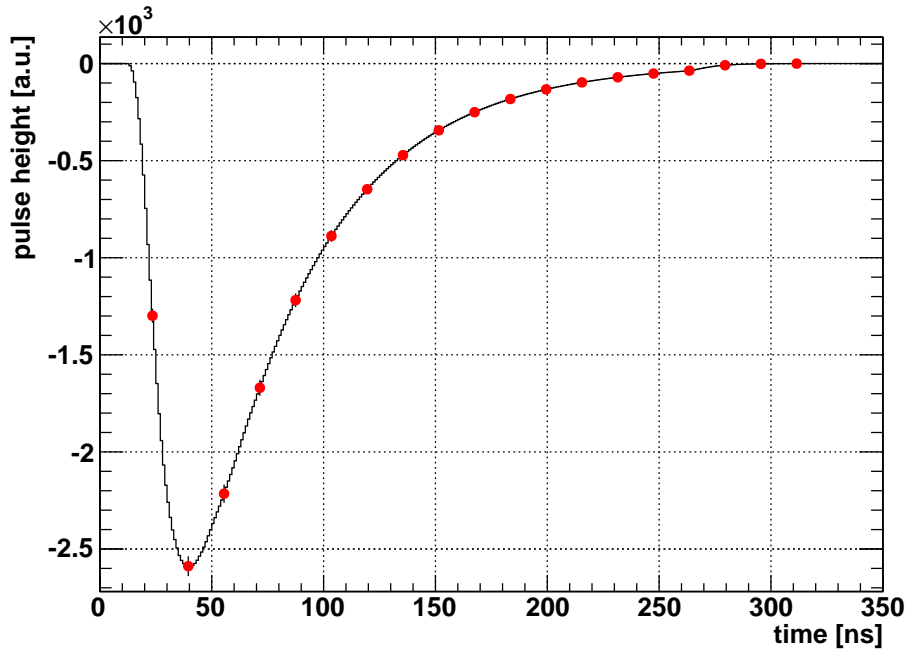


Fig. 5.6.: The resulting SiPM output pulse generated from the photon distribution shown in Fig. 5.5(d). The red dots represent the sampling points seen by the sADC.

In order to determine the detector's resolution, the charge channels have to be reconverted into energies. This is done by correlating the resulting charge channel with the MC-truth of the deposited energy from the simulation (see Fig. 5.7).

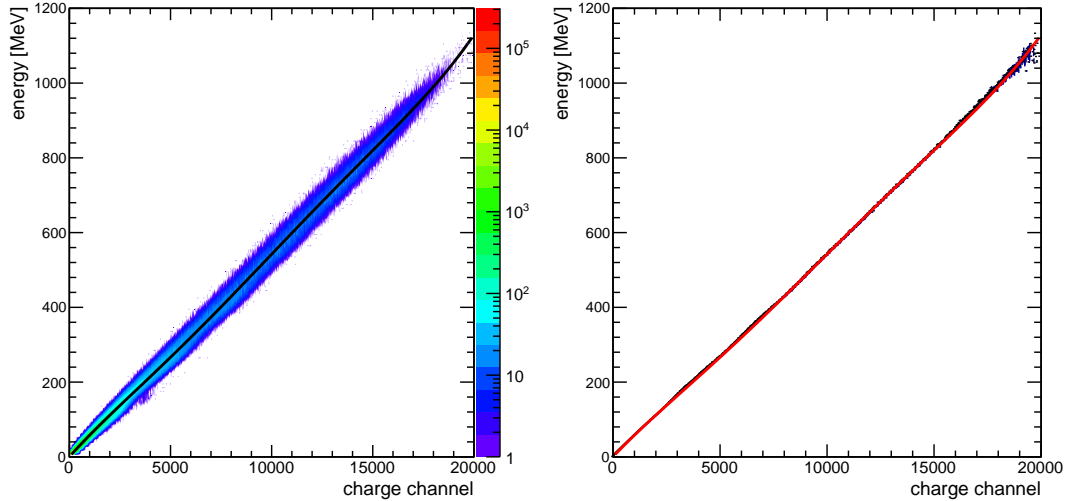


Fig. 5.7.: Correlation of charge channel and deposited energy from 1.754 million events, generated with the PHOKHARA generator using photons from 7 different energy regions. The left plot shows a scatter plot of both variables with a logarithmic z -axis in order to show the corresponding densities. The plot on the right is a profile histogram, where the average contents of the bins are fitted with a fifth order polynomial. The resulting fit function is drawn in black in the scatter plot, the fit parameters can be found in Tab. A.2 .

5.2.3. Energy Resolution

The simulation was done using the PHOKHARA [87] physics generator (version 7.0), which precisely delivers the physics of electron-positron annihilations into hadrons with photons from the initial state (ISR). Since the energy distribution of ISR photons is channel dependend, the photon energies have been fixed. 7 different ISR photon energy data sets have been simulated (1515 MeV, 1385 MeV, 1250 MeV, 985 MeV, 720 MeV, 455 MeV, 190 MeV), each containing 220000 events. The resolution of the detector can be determined by plotting the ratio

$$\frac{\text{measured photon energy}}{\text{photon energy from generator}} \quad , \quad (5.2.9)$$

fitting the obtained spectrum with a gaussian(-like) function and calculating σ/μ from the fit. This is shown for a photon energy of 1250 MeV in Fig. 5.8, fits for the other photon energies can be found in App. A.5.3.

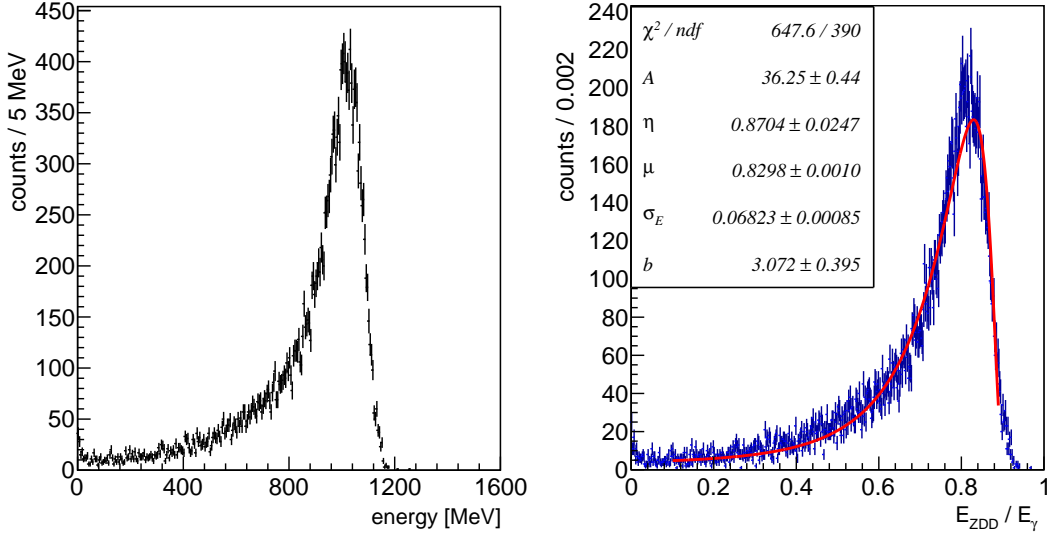


Fig. 5.8.: The plot on the left side shows the reconstructed energy deposition in the cZDD from an incident 1250 MeV photon. The histogram on the right side shows the corresponding measured energy to photon energy from generator ratio fitted with a logarithmic normal distribution.

The histogram on the right is fitted with a logarithmic normal distribution

$$f(E) = A \cdot \frac{\eta}{\sqrt{2\pi} \sigma_E \sigma_0} \cdot \exp \left\{ -\frac{1}{2} \left[\frac{\ln^2 \left(1 - \left(\frac{\eta(E-\mu)}{\sigma_E} \right) \right)}{\sigma_0^2} + \sigma_0^2 \right] \right\} + b \quad (5.2.10)$$

$$\sigma_0 = \frac{2}{2.35} \ln \left[\eta \frac{2.35}{2} + \sqrt{1 + \left(\eta \frac{2.35}{2} \right)^2} \right], \quad \sigma_E = \frac{\text{FWHM}}{2.35},$$

the ratio of σ_E to E corresponds to the detector resolution, which is summarized for the different photon energies in Tab. 5.2. The overall cZDD resolution was derived from Fig. 5.9 and determined to be

$$\frac{\sigma_E}{\mu} = c_1 \oplus \frac{c_2}{\sqrt{E_\gamma [\text{GeV}]}} = 0.06 \oplus \frac{0.025}{\sqrt{E_\gamma [\text{GeV}]}}. \quad (5.2.11)$$

The first term is caused by geometrical issues, amount of dead material and leakages caused by insufficient detector volume and is approximately energy independent. The second term depends on the effective light yield of the scintillator crystals measured by the SiPMs. Therefore, mainly the second term is affected by changings in the scintillator and SiPM properties. The energy resolution of the ZDD currently installed at BESIII was determined to be [70]

$$\frac{\sigma_E}{\mu} = 0.05 \oplus \frac{0.07}{\sqrt{E_\gamma [\text{GeV}]}}. \quad (5.2.12)$$

The first term is approximately the same as for the cZDD, supporting the assumption that this term is mainly caused by geometrical issues. The second term differs significantly, which is due to different detector materials and properties.

Although the obtained results presented here need to be considered as preliminary and the simulation parameters need to be tuned to real experimental data, the cZDD's capabilities prove to be competitive to those of the currently installed ZDD.

photon energy [MeV]	σ_E/μ [%]
1515	7.9
1385	8.3
1250	8.2
985	8.7
720	9.0
455	9.9
190	11.5

Tab. 5.2.: cZDD resolution for different photon energies (see App. A.5.3).

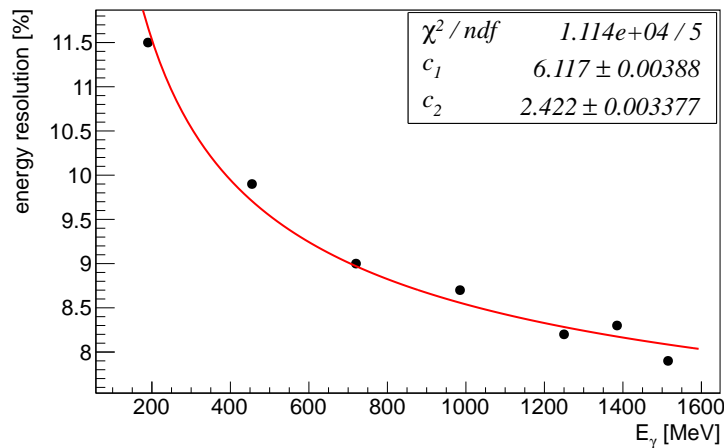


Fig. 5.9.: Overall cZDD resolution from Tab. 5.2 fitted with Eq. (5.2.11)

5.2.4. Position Reconstruction

The deposited energy strongly depends on the photon's impact on the detector: A photon with given energy centrally hitting the detector will create a bigger signal than the same photon hitting the outer edge of the detector. For the reconstruction of $E_{\gamma_{\text{ISR}}}$ this impact must be taken into account.

The simplest position reconstruction algorithm uses the linear energy-weighted superposition of all crystal positions (X_i, Y_i) (see Fig. 4.3) to reconstruct the center of gravity (X_{cg}, Y_{cg}) of the induced electromagnetic shower:

$$X_{cg} = \frac{\sum_i w_i X_i}{\sum_i w_i}, \quad Y_{cg} = \frac{\sum_i w_i Y_i}{\sum_i w_i}, \quad w_i = E_i \quad . \quad (5.2.13)$$

Because of the gap in the detector's design only crystals of the upper or lower detector part should be taken into account for position reconstruction. The selection criterium here is the crystal with the highest measured energy.

However, as pointed out in [88], this algorithm delivers a systematic shift towards the crystal center leading to hot spots in the obtained position spectra. These hotspots do not have a physical meaning, but are an effect of the algorithm. This effect is even augmented by the small design of the detector, where almost every crystal sits at an outer edge of the calorimeter.

An algorithm, which intrinsically delivers an impact with minimum systematic shift has been presented in [89]. This algorithm takes into account the lateral shower profile inside the detector, which is rather narrow. The positions of the single crystals are then not linearly weighted anymore, but a logarithmic weighting of the individual crystal energy depositions is chosen, taking into account the exponential falloff of the shower energy distribution [89]. The weighing factors w_i from Eq. (5.2.13) now become

$$w_i = \begin{cases} 0 & , \text{ when } W_0 + \ln\left(\frac{E_i}{E_T}\right) \leq 0 ; \\ W_0 + \ln\left(\frac{E_i}{E_T}\right) & , \text{ else .} \end{cases}$$

$$E_T = \sum_i E_i \quad (5.2.14)$$

W_0 is a free parameter, which should be set high enough to deliver a Gaussian-like distribution of X_{cg} , but should also be low enough to avoid degradation in position resolution [90]. For the cZDD, large variations of incident photon energy are expected, a non-constant value of $W_0(E_T)$, moderately rising with increasing cluster energy E_T , could have a beneficial influence on the position response linearity and resolution [90].

Starting with a $\sqrt{s} = 3770 \text{ MeV} = E_{\psi(3770)}$, where BEPCII has its peak luminosity, 1.1 million ISR events have been simulated in BOSS for four different ISR photon energies (200 MeV, 600 MeV, 1000 MeV and 1400 MeV). Fig. 5.10 shows the reconstructed impacts for each photon energy using the linear energy weighting from Eq. (5.2.13). Using a fixed $W_0 = 3.9$, which has been determined as a good compromise between reasonable shape and narrow width, Fig. 5.11 shows the corresponding impacts using the weight factors from Eq. (5.2.14). The energy deposition threshold for each crystal has been set to 10 MeV, smaller values can not be accurately measured by the lead tungsten crystals.

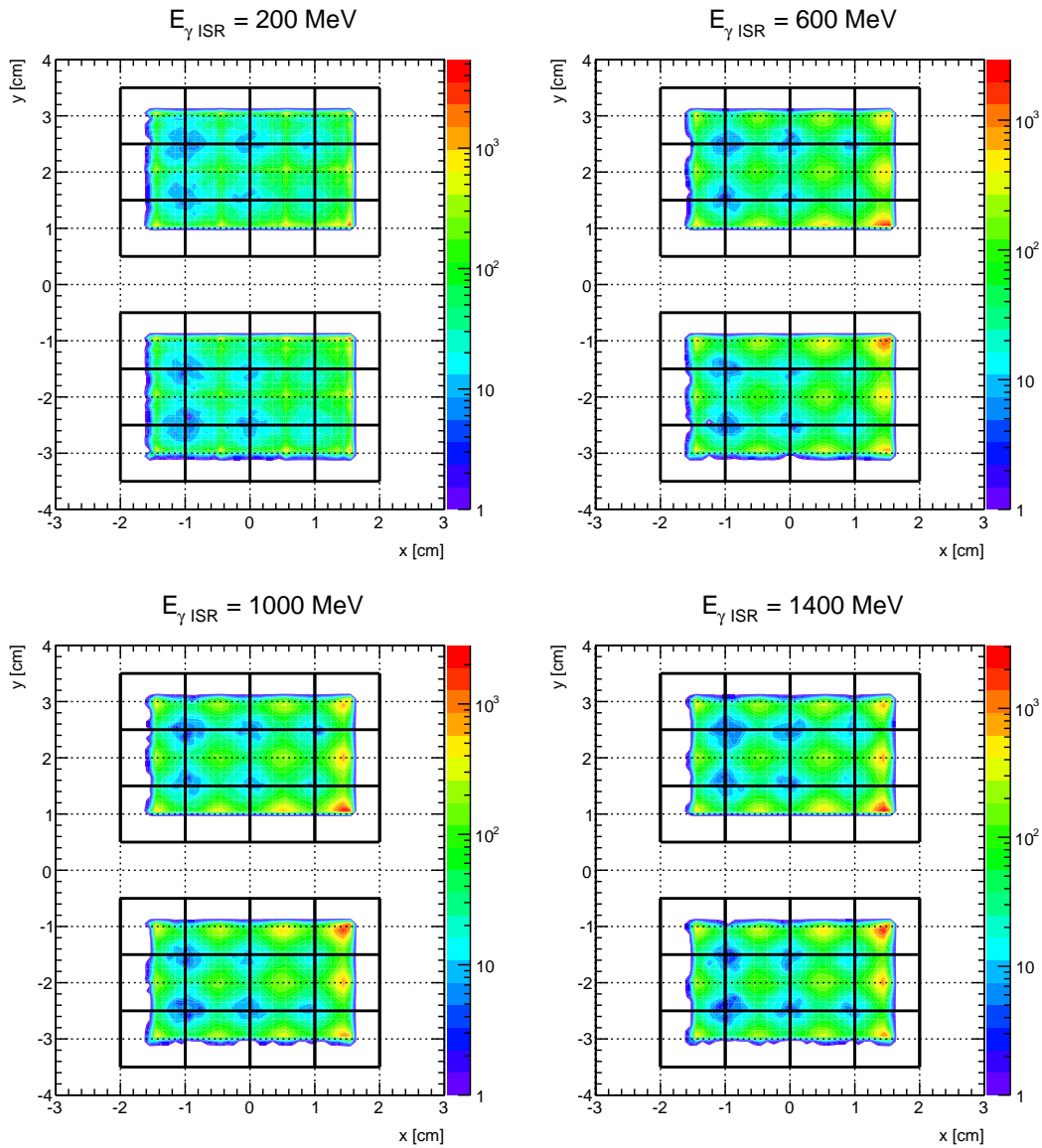


Fig. 5.10.: Reconstructed ISR photon impact positions for different photon energies using the linear energy weighting from Eq. (5.2.13). For each energy 1.1 million events have been simulated in BOSS with the Phokhara event generator. The hot spots arise from the algorithm’s systematic shift towards the crystal center. The angular distribution of the ISR photons can be seen in Fig. 4.5, which explains why the hot spots are more intense on the right side of the detector.

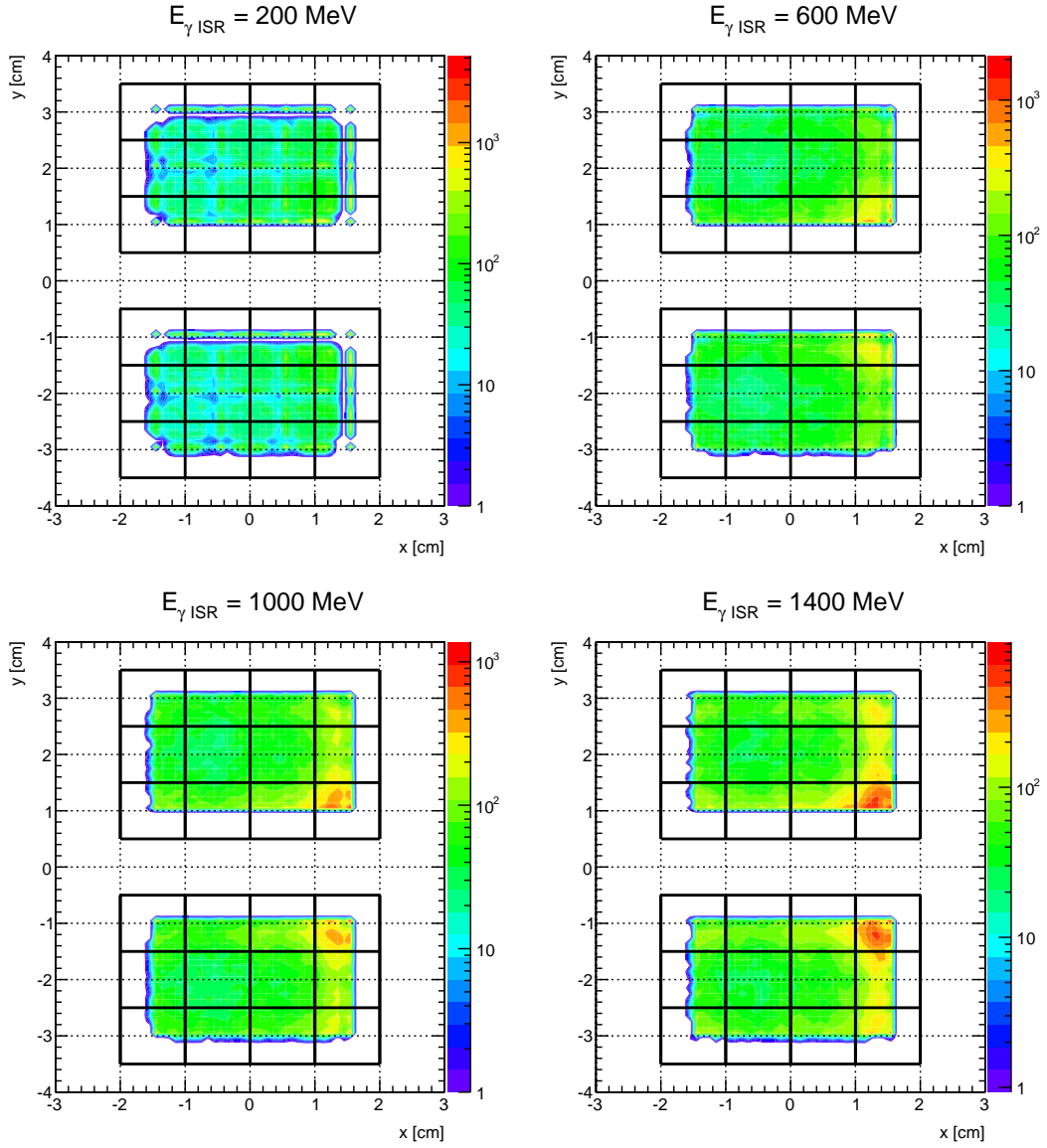


Fig. 5.11.: Reconstructed ISR photon impact positions for different photon energies using the logarithmic energy weighting from Eq. (5.2.14). For each energy 1.1 million events have been simulated in BOSS with the Phokhara event generator. The reconstructed impacts look far more smooth and realistic than those in Fig. 5.10. The segmentation in the position spectrum for 200 MeV photons is caused by the threshold for the minimum energy deposition per crystal, which has been set to 10 MeV. For higher photon energies, this threshold does not effect the spectra very much.

Both algorithms cannot precisely reconstruct impacts which lie at the very edges of the detector, because only the crystal's center positions enter the algorithm. This explains the empty areas at the outer edges in the obtained spectra of the detector. The spectra obtained with the linear weighting shows the expected hot spots caused by the systematic shifts of the algorithm. The corresponding spectra using the logarithmic weighing looks much more smooth and realistic. The difference of the radial distance from MC-truth and reconstructed radial distance is depicted in Fig. 5.12.

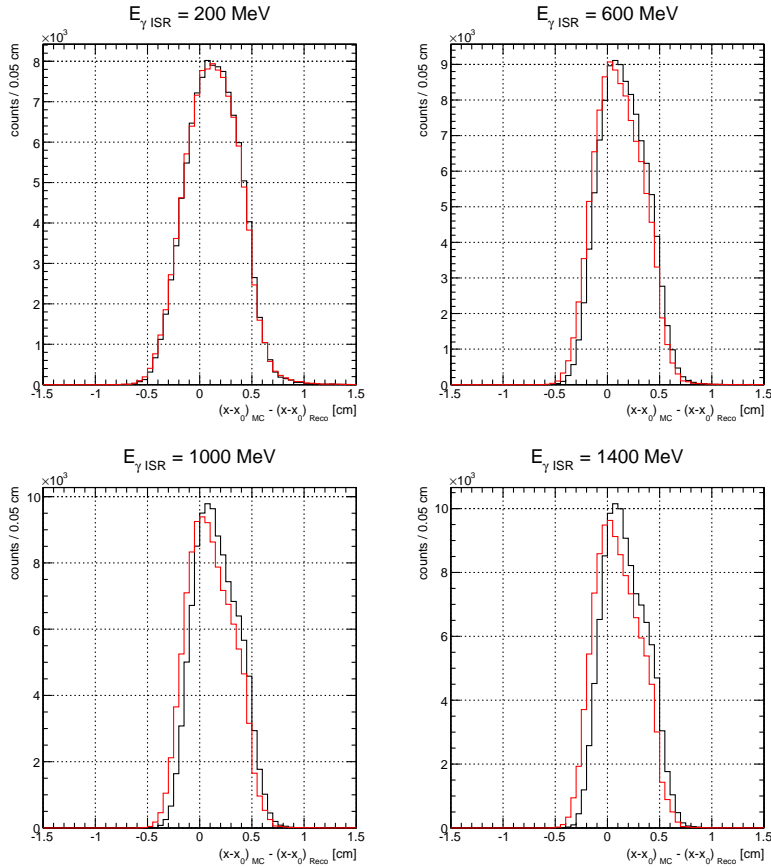


Fig. 5.12.: The difference of the radial distance from MC-truth and reconstructed radial distance using the linear weighting algorithm (black) and the logarithmic weighting algorithm (red). The resolution for the latter one is slightly better. In both algorithms the distance to the detector center tends to be too small, which is caused by the algorithm's inability to reconstruct impacts at the very edges of the detector.

It shows that the algorithm with logarithmic energy weighting delivers a slightly better position resolution than the one with linear weighting. Hence, the algorithm with the logarithmic weighting has been used for the determination of \sqrt{s}_{ISR} .

5.2.5. Determination of \sqrt{s}_{ISR}

The most important purpose of the cZDD is the determination of \sqrt{s}_{ISR} . This is especially true for inclusive measurements, where it is not possible to measure all hadrons of the final state e.g. in the $n\bar{n}$ channel. By measuring the deposited energy in the detector volume, $E_{\gamma_{\text{ISR}}}$ can be determined. Looking at the detector's design we expect the best energy resolution for photons, which enter the detector in the center ($x_0 = (X_0, Y_0) = (0 \text{ cm}, \pm 2 \text{ cm})$, see the red dots in Fig. 4.3). The radial distance to this center

$$x - x_0 = \sqrt{(X_{\text{cg}} - X_0)^2 + (Y_{\text{cg}} - Y_0)^2} \quad (5.2.15)$$

should be the determining factor for the quality of the photon energy measurement. X_{cg} and Y_{cg} are the coordinates of the reconstructed impact using the algorithm with logarithmic energy weighting mentioned above.

This radial distance can be plotted against the ratio of the measured energy to the MC-truth of the photon's energy. The same ratio with MC-truth of the photon impact as an input, can be studied for comparison. The reconstructed photon energy can then be used for the calculation of \sqrt{s}_{ISR} using Eq. (3.1.1). The ratio of reconstructed \sqrt{s}_{ISR} to \sqrt{s}_{ISR} from MC-truth displays the quality of the \sqrt{s}_{ISR} determination using the cZDD. All these calculations have been performed for the four former photon energies and can be seen in Fig. 5.13, 5.14, 5.15 and 5.16.

Since the fraction of measured- to real photon energy is always smaller than 1, \sqrt{s}_{ISR} will always be determined too high. That is the reason why the energy distributions in Fig. 5.13, 5.14, 5.15 and 5.16 **(a)** and **(b)** are slightly falling with increasing radial distance, whereas the corresponding \sqrt{s}_{ISR} distributions are rising with increasing radial distance to the center. Although the energy resolution of the cZDD increases with increasing photon energy, the determination of \sqrt{s}_{ISR} worsens. Looking back at Fig. 3.2 from chapter 3 this becomes clear: At small photon energies the derivative of \sqrt{s}_{ISR} is relatively flat, therefore a change in the photon energy hardly affects the value of \sqrt{s}_{ISR} . But the higher the photon energy, the steeper the derivative of \sqrt{s}_{ISR} , which means that any change in the measured photon energy strongly affects \sqrt{s}_{ISR} . We should also mention that the quality of the \sqrt{s}_{ISR} determination is not only determined by the photon energy, but also by the initial \sqrt{s} : The initial \sqrt{s} determines the steepness of the derivative of \sqrt{s}_{ISR} for a given photon energy.

For the concrete \sqrt{s}_{ISR} determination Fig. 5.13, 5.14, 5.15 and 5.16 (c) have been projected onto the y -axis for given radial distance bins and fitted with the *Novosibirsk function* (taken from [91]) defined as

$$f(x) = A \cdot \exp \left\{ -0.5 \cdot \left(\frac{\ln^2(1 + \Lambda \cdot \tau \cdot (x - \mu))}{\tau^2} + \tau^2 \right) \right\} \quad (5.2.16)$$

$$\Lambda = \frac{\sinh(\tau \cdot \sqrt{\ln(4)})}{\sigma \cdot \tau \cdot \sqrt{\ln(4)}} \quad ,$$

which is a commonly used gaussian-like function with mean μ , width σ and a tail parameter τ accounting for low or high value tails of the fitted distribution. The corresponding fits for the four photon energies can be found in App. A.6. The resulting $\sqrt{s}_{\text{ISR}}(\text{Reco}) / \sqrt{s}_{\text{ISR}}(\text{MC})$ mean values for each radial distance bin have been drawn in a graph and fitted with a third order polynomial for each photon energy. This can be seen in Fig. 5.17, respective fit parameters are shown in Tab. 5.3. The functions obtained by these fits can be used to correct the reconstructed \sqrt{s}_{ISR} values. For radial distances up to 1.2 cm from the center the correction factors are more or less stable for each photon energy.

The resolution of \sqrt{s}_{ISR} , which is defined by σ/μ of the fits from App. A.6, has been plotted in the same way for the four photon energies (Fig. 5.18) and also fitted with a third order polynomial (see Tab. 5.4). As expected, the resolution of \sqrt{s}_{ISR} becomes worse with increasing radial distance to the detector's center, but is nevertheless significantly better than 10% for photon impacts with $x - x_0 \leq 1.2$ cm.

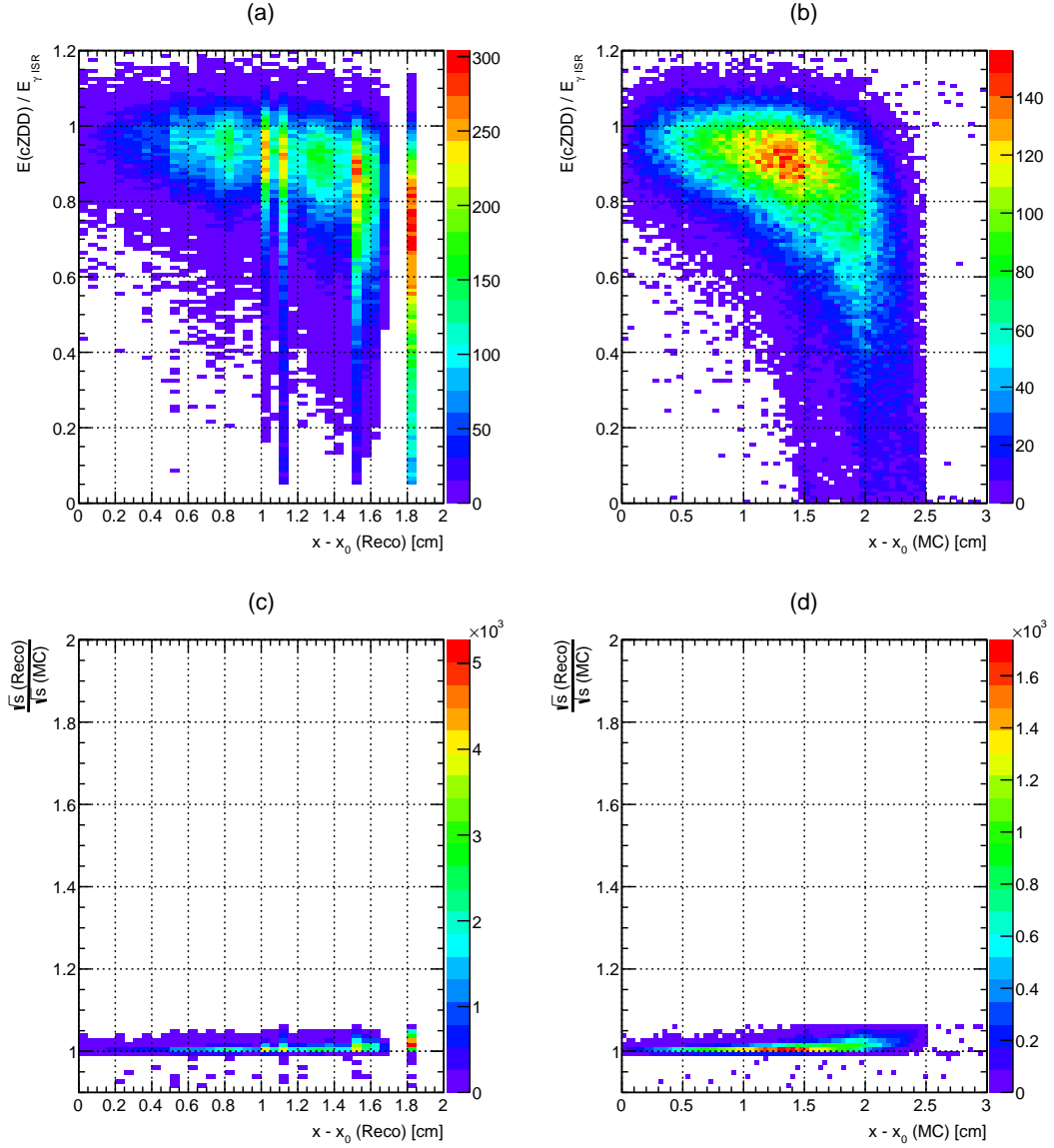


Fig. 5.13.: Scatter plots for 200 MeV ISR photons: (a) shows the reconstructed radial distance plotted against the ratio of measured photon energy to photon energy from MC-truth, the same plot using the radial distance from MC-truth is shown in (b). The reconstructed radial distance plotted against the ratio of the reconstructed \sqrt{s}_{ISR} to \sqrt{s}_{ISR} from MC-truth is plotted in (c). The same plot with the radial distance from MC-truth is displayed in (d). The hot spots in (a) are caused by the segmentation of the reconstructed impacts from Fig. 5.10. Although the energy measurement is rather poor, the determination of \sqrt{s}_{ISR} is quite good for 200 MeV photons.

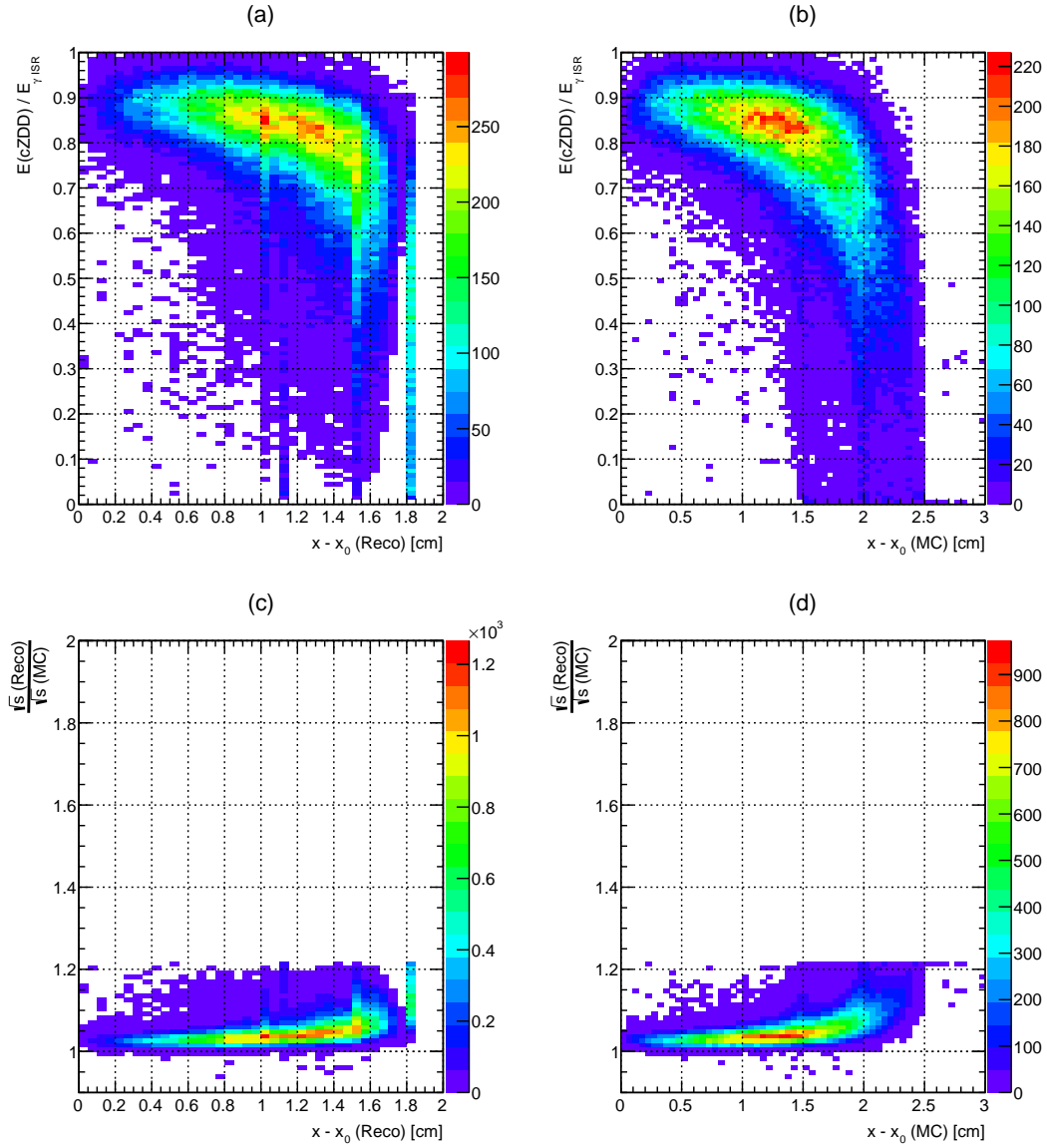


Fig. 5.14.: Scatter plots for 600 MeV ISR photons: **(a)** shows the reconstructed radial distance plotted against the ratio of measured photon energy to photon energy from MC-truth, the same plot using the radial distance from MC-truth is shown in **(b)**. The reconstructed radial distance plotted against the ratio of the reconstructed \sqrt{s}_{ISR} to \sqrt{s}_{ISR} from MC-truth is plotted in **(c)**. The same plot with the radial distance from MC-truth is displayed in **(d)**.

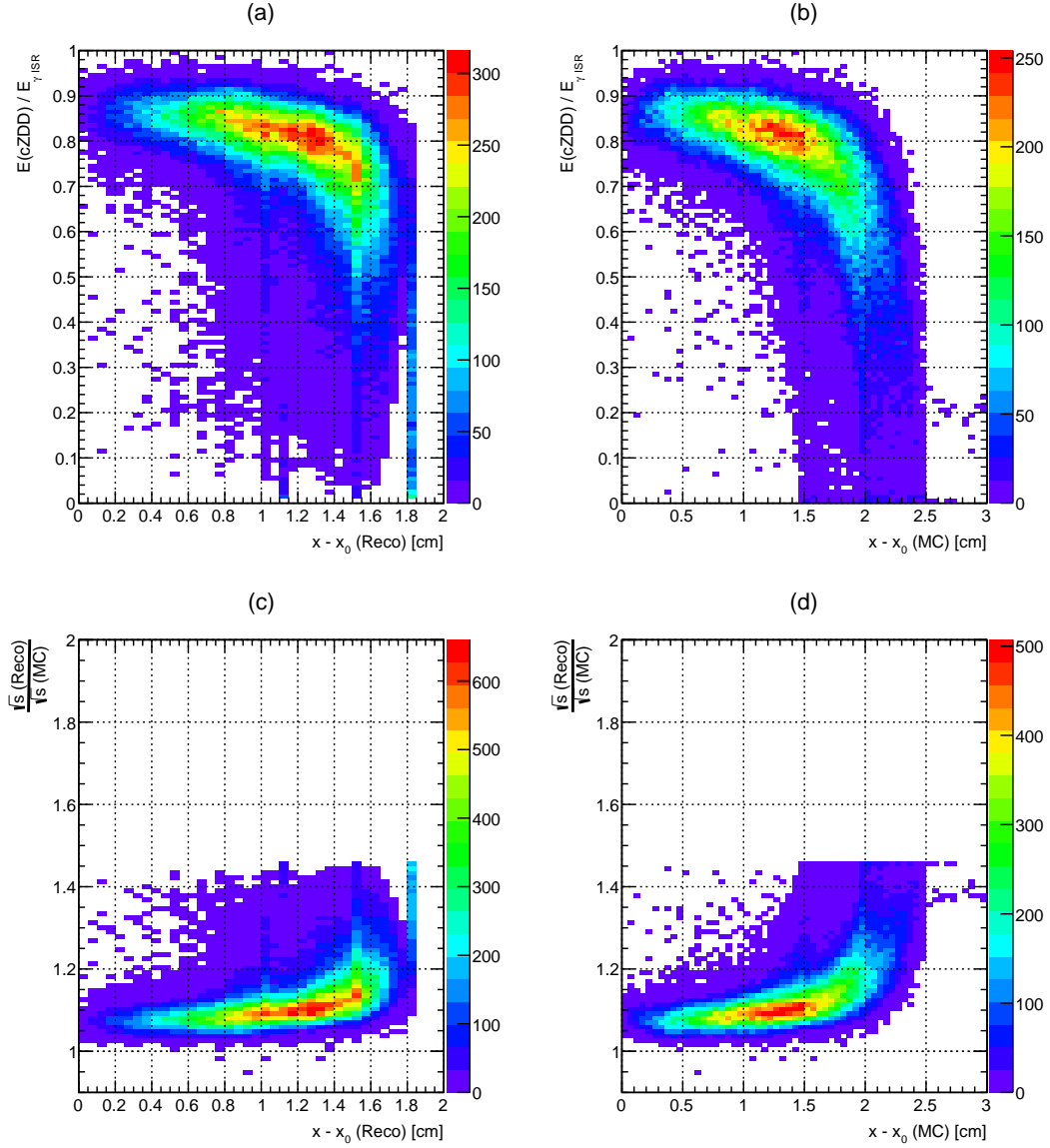


Fig. 5.15.: Scatter plots for 1000 MeV ISR photons: (a) shows the reconstructed radial distance plotted against the ratio of measured photon energy to photon energy from MC-truth, the same plot using the radial distance from MC-truth is shown in (b). The reconstructed radial distance plotted against the ratio of the reconstructed \sqrt{s}_{ISR} to \sqrt{s}_{ISR} from MC-truth is plotted in (c). The same plot with the radial distance from MC-truth is displayed in (d).

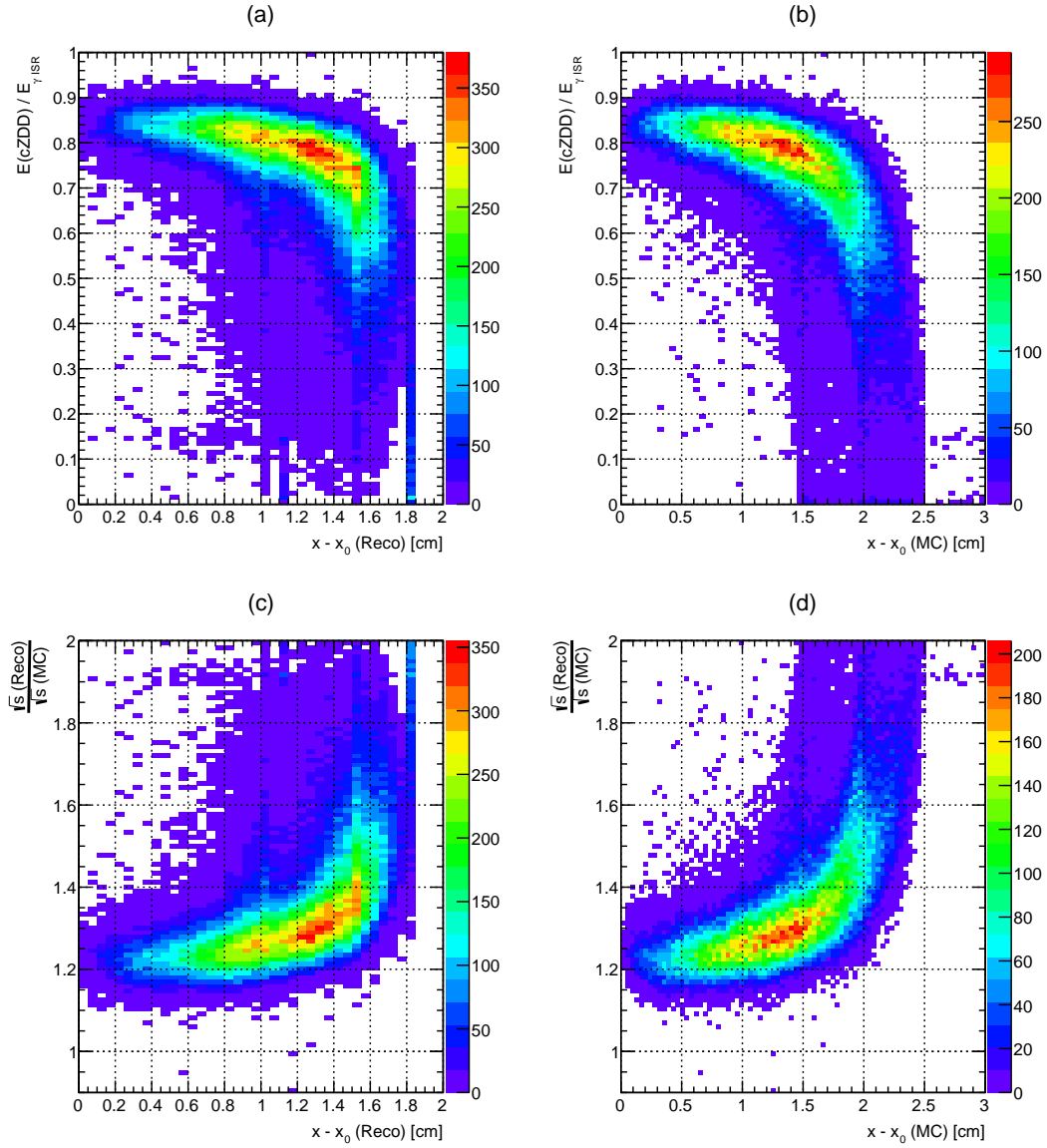


Fig. 5.16.: Scatter plots for 1400 MeV ISR photons: **(a)** shows the reconstructed radial distance plotted against the ratio of measured photon energy to photon energy from MC-truth, the same plot using the radial distance from MC-truth is shown in **(b)**. The reconstructed radial distance plotted against the ratio of the reconstructed \sqrt{s}_{ISR} to \sqrt{s}_{ISR} from MC-truth is plotted in **(c)**. The same plot with the radial distance from MC-truth is displayed in **(d)**.

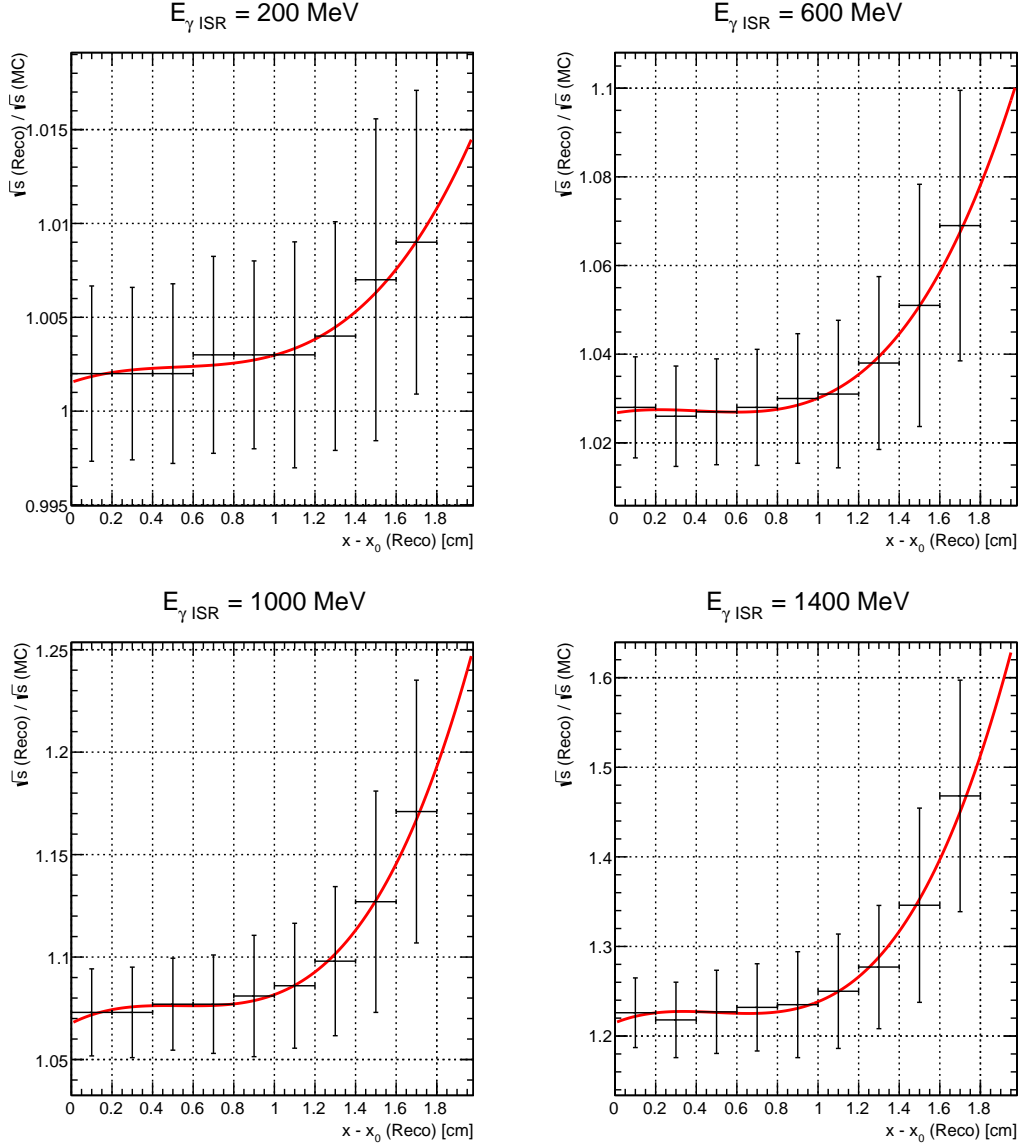


Fig. 5.17.: Fitted mean values for the ratio of reconstructed \sqrt{s}_{ISR} to \sqrt{s}_{ISR} from MC-truth for given radial distance bins for the four former photon energies. The error bars depict the σ of the obtained distribution. The fit function being used is a third order polynomial, the corresponding fit values can be found in Tab. 5.3.

parameter	$E_\gamma = 200$ MeV	$E_\gamma = 600$ MeV	$E_\gamma = 1000$ MeV	$E_\gamma = 1400$ MeV
p_0	1.0015	1.0267	1.0677	1.2149
p_1	$3.6602 \cdot 10^{-3}$	$7.8976 \cdot 10^{-3}$	$4.9601 \cdot 10^{-2}$	$9.0333 \cdot 10^{-2}$
p_2	$-6.0225 \cdot 10^{-3}$	$-2.4583 \cdot 10^{-2}$	$-9.4021 \cdot 10^{-2}$	$-2.0287 \cdot 10^{-1}$
p_3	$3.8043 \cdot 10^{-3}$	$2.0037 \cdot 10^{-2}$	$5.8377 \cdot 10^{-2}$	$1.3597 \cdot 10^{-1}$

Tab. 5.3.: Obtained fits parameters for Fig. 5.17.

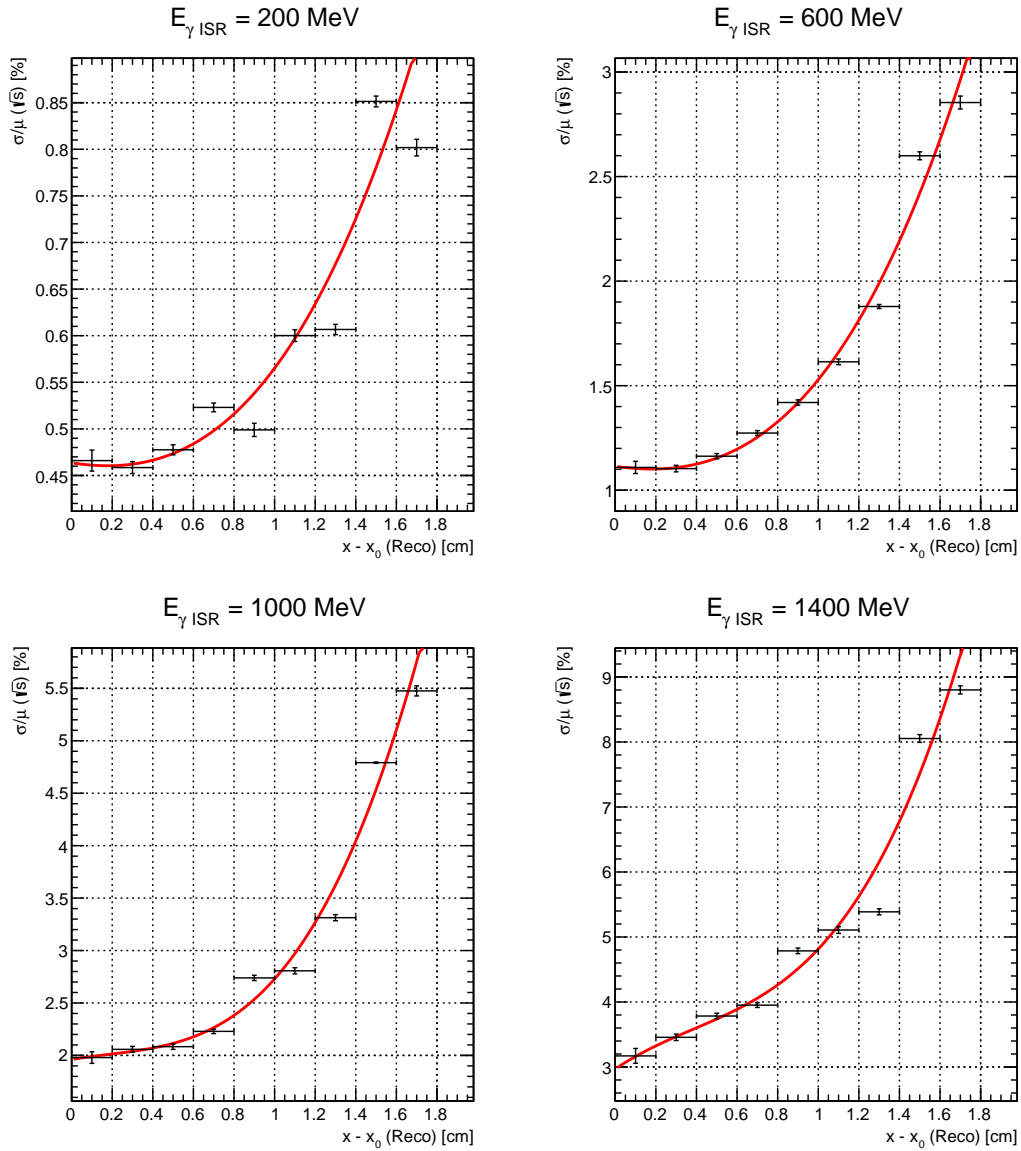


Fig. 5.18.: Resolution of the reconstructed \sqrt{s}_{ISR} in dependence of the radial distance to the detector's center $x - x_0$ for four photon energies. Tab. 5.4 contains the obtained fit parameters.

parameter	$E_\gamma = 200 \text{ MeV}$	$E_\gamma = 600 \text{ MeV}$	$E_\gamma = 1000 \text{ MeV}$	$E_\gamma = 1400 \text{ MeV}$
p_0	$4.6358 \cdot 10^{-1}$	1.1142	1.9607	2.96939
p_1	$-3.3363 \cdot 10^{-2}$	$-1.3405 \cdot 10^{-1}$	$3.3502 \cdot 10^{-1}$	2.1086
p_2	$7.8517 \cdot 10^{-2}$	$3.0612 \cdot 10^{-1}$	$-5.4125 \cdot 10^{-1}$	-2.01855
p_3	$5.6393 \cdot 10^{-2}$	$2.4260 \cdot 10^{-1}$	$9.7477 \cdot 10^{-1}$	1.7548

Tab. 5.4.: Obtained fits parameters for Fig. 5.18.

Now that the correction functions for \sqrt{s}_{ISR} are known, the obtained value from Eq. (3.1.1) can be corrected. Fig. 5.19 shows a plot of the obtained uncorrected \sqrt{s}_{ISR} values and the values after correction with the correction functions derived above. As can be seen, the distributions for the different energies are flatter in general and fit much better to the true \sqrt{s}_{ISR} . A distinction of different photon energies is possible, as both plots show. But we have to keep in mind that the spectrum from Fig. 5.19 (b) was obtained with knowing the appropriate correction factors for the input photon energy. In the experiment, this is of course not the case. Thus, additional information from the BESIII detectors about the Lorentz-boost of the center-of-mass system, which can be analyzed by the asymmetry of the event topology, and the total visible energy might be helpful for getting a first guess on the photon's energy. This could be used as a starting point of an iterative algorithm, where the assumptions made are being tested and tuned respectively until the algorithm has arrived at a photon energy which fits best to all obtained detector data.

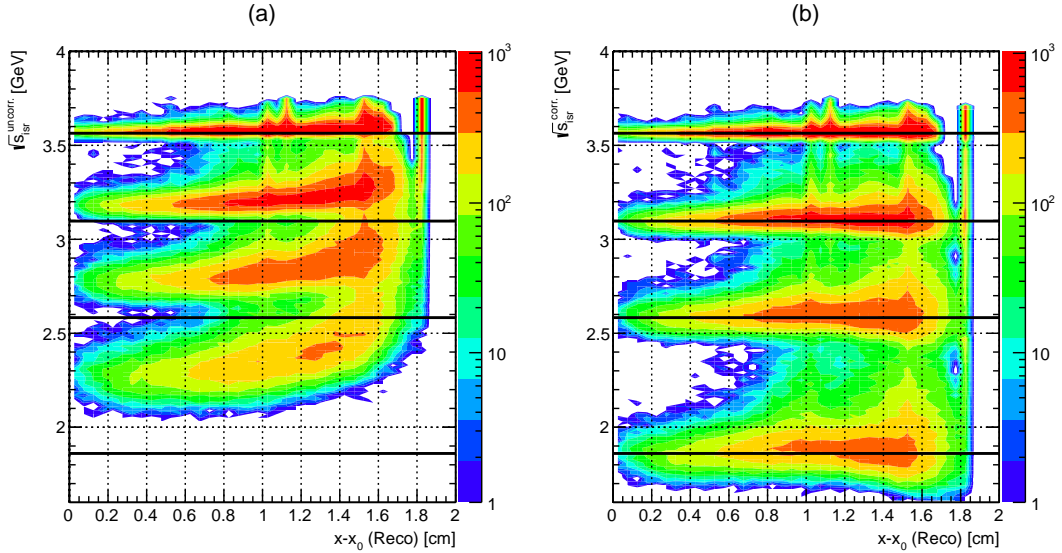


Fig. 5.19.: Obtained values for \sqrt{s}_{ISR} (a) before correction and (b) after correction. The horizontal black lines depict the true values of \sqrt{s}_{ISR} , which nicely fit in the corrected spectrum of (b).

5.3. Conclusion

A detailed Geant4-based simulation of the cZDD has been implemented into the BOSS framework and first results of the energy resolution and its capabilities to determine \sqrt{s}_{ISR} have been investigated. The determination of \sqrt{s}_{ISR} allows for R ratio measurements in energy regions from threshold up to initial \sqrt{s} . Based on [24], the main problem of ISR studies of the R measurement for the inclusive hadronic cross section, has been that the resolution deteriorates rapidly for low recoil masses, when the photon is not detected. Despite of its small size, the cZDD is able to detect ISR photons with a high angular acceptance, which is comparable to that of the whole BESIII detector [70], and thus obviates the need for demanding low recoil masses of the hadronic system.

Now that the capabilities of the cZDD have been explored, developments for its DAQ based on $\bar{\text{P}}\text{ANDA}$ prototype modules have been done, which are described in the next chapter.

RELATED DAQ DEVELOPMENTS

The $\bar{\text{P}}\text{ANDA}$ DAQ scheme as explained in chapter 2 is very complex: Many newly developed techniques have to be combined and need to collaborate in order to fulfill the requirements for a successful DAQ operation. This cannot be done without extensive testing, evaluation and debugging phases.

This chapter describes developments done for a prototype cZDD DAQ, in which modules designed for $\bar{\text{P}}\text{ANDA}$ are used and can be investigated in a realistic high rate environment. The prototype detector and DAQ consists of six main components (see Fig. 6.1):

1. A $\bar{\text{P}}\text{ANDA}$ type **PbWO₄ prototype mini crystal** similar to those foreseen for the final cZDD , will be read out by two
2. **Silicon Photomultipliers** (SiPMs) from Hamamatsu, which will pipeline their signal through a preamp into the
3. **MPPC Coincidence Board**, which was developed during this thesis for pre-filtering the MPPC data. The output of the MPPC coincidence board will be sent to a FPGA-based programmable prototype
4. **sampling ADC** (sADC) developed for the $\bar{\text{P}}\text{ANDA}$ EMC readout by the University of Uppsala and KIV Groningen. Via an optical interface the data is transmitted to a
5. **Compute Node** (CN) developed by IHEP (Beijing, China) and JLU Giessen. Here, the data will be processed and, depending on the event selection criteria, selectively transmitted to a
6. **PC**, where data analysis and storage can be done.

Additionally, four quadratic $\overline{\text{P}}\text{ANDA}$ endcap crystals surrounding the mini crystal, read out by standard PMTs and also digitized with the sADC, will provide a small crystal cluster, which can be used for testing event building algorithms. The whole detector can be seen in Fig. 7.8 in chapter 7.

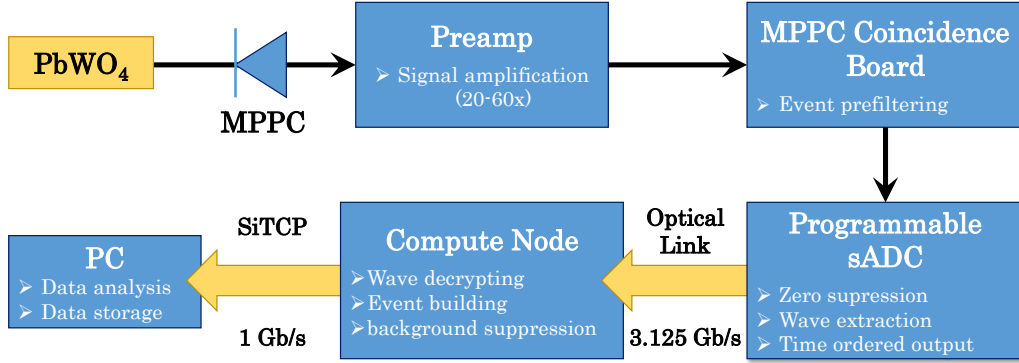


Fig. 6.1.: DAQ chain developed for the prototype cZDD setup.

The properties of the PbWO_4 crystal and the SiPMs have already been described in chapter 4. The next sections explain the single parts of the DAQ chain, starting with the MPPC coincidence board for pre-filtering the SiPMs signals.

6.1. MPPC Coincidence Board

Approximately 0.1 to 1% of all pixels in a MPPC are continuously in a state of recovery because of dark counts [77]. In order to filter out these thermally generated noise signals and to deliver a clean baseline for the sADC, a customized readout board was developed in collaboration with the electronics workshop of II. Physikalisches Institut, JLU Giessen. Since the crystal is read out by two MPPCs and the thermal noise signals of the MPPCs are stochastic and uncorrelated, a logical AND between two MPPC signals would filter out the majority of all thermally generated signals.

The principal logic for the circuit of the coincidence board can be seen in Fig. 6.2. First, each MPPC signal is split into two: one signal is sent into an analogue delay line (S_1), the other signal (S_2) is routed to a comparator with an adjustable threshold. If S_2 is above the threshold, the comparator's output will be a logical '1', otherwise it will be a logical '0' (TTL-logic).

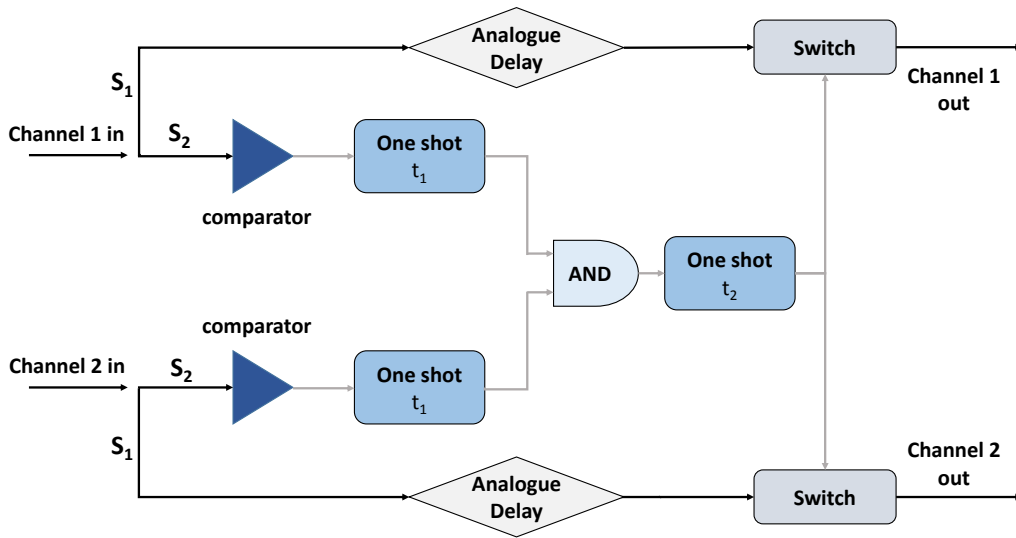


Fig. 6.2.: Principal logic of the MPPC coincidence board.

The output signal is routed to a so-called *one shot*: If the one shot sees a rising edge from the comparator's output, it will create a logical '1' for an adjustable amount of time t_1 before it returns to '0'. This output signal is one input of a 2-channel AND gate, the other input comes from the same logic of the second channel. Only if both one shots from channel 1 and channel 2 fire within t_1 , the output of the AND gate will be high. This output signal will trigger a second one shot with adjustable time constant t_2 . This one shot will drive a switch, which will open the gate for the delayed analogue signals S_1 from both channels and route them to the output.

With t_1 the coincidence window of both channels can be fixed: Only if both channels fire within this time, the signals will be routed to the output, otherwise the output will be zero, which is the baseline seen by the sADC. For real coincidences, t_1 should be as small as possible and comparable to the delay time of the scintillator material ($\sim 7 - 8$ ns). Due to technical limits of the used one shots, t_1 has been fixed to 80 ns. The second time constant t_2 adjusts the length of the gate. It has to be chosen in a way that the whole pulse can pass the gate. This value has been fixed to 350 ns, based on simulations explained earlier (see chapter 5). The analogue delays have a length of 30 ns, which is approximately the time the logic gates need for evaluation of the coincidence condition. Fig. 6.3 shows a picture of the produced 2-channel MPPC coincidence board. Due to the electronic design of the board, the negative SiPM pulses from the preamps are inverted, leaving a positive pulse to be digitized by the sADC explained in the next section.

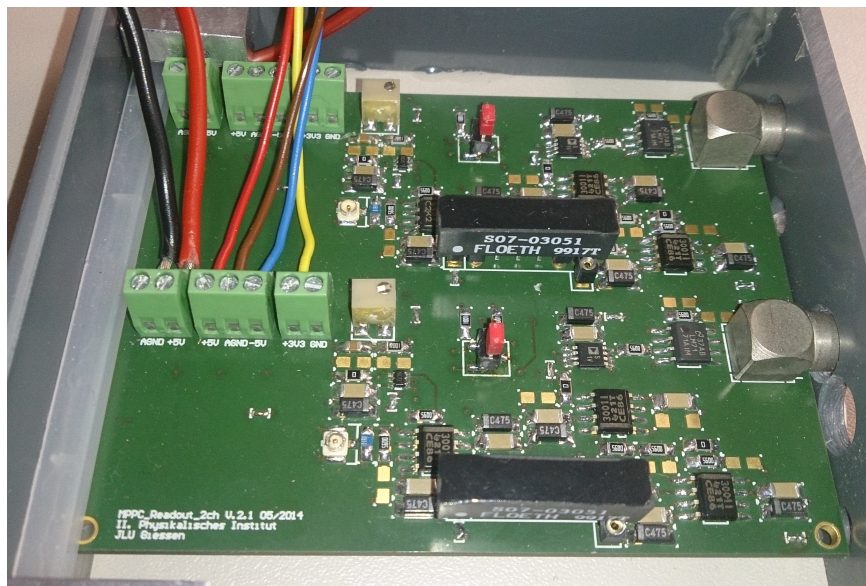


Fig. 6.3.: Picture of the produced 2-channel MPPC readout board, whose principal logic is shown in Fig. 6.2, the elongated black components are the analogue delays.

6.2. The sampling ADC (sADC) Prototype

The coincident signals from the MPPC readout board are digitized by sampling Analog-to-Digital Converters (sADCs), which take samples of the continuous analog signals and convert them into a sequence of digital values. This sampling principle allows dead-time free data acquisition at high rates as are expected at BESIII and \bar{P} ANDA. The prototype sADC [92] used in this thesis work was developed by Pawel Marciniwski from Uppsala university. Originally developed for testing different feature extraction algorithms and getting an idea of how much FPGA resources are required for the logic [93], by now an extensive firmware for a fully functional ADC including zero suppression, pulse detection, pileup recovery and feature extraction has been developed by Uppsala university and KVI Groningen. The prototype is a Virtex-5 based programmable 16-channel 14-bit, 62.5 Msps ADC with an optical output, which accepts input signals from 0 to ± 1 V [93], depending on firmware settings and board equipping. It is important to notice that the ADC can only deal with unipolar pulses, bipolar pulses will be cut off at the zero-crossing. The sADC uses pulse recognition and is self-triggering, the baseline of the pulse is determined by the extrapolation from ADC values before the pulse arrives. Therefore a clean baseline delivered by the MPPC coincidence board is advantageous.

The currently used firmware allows to use 8 channels at once and delivers a time-ordered output of the digitized signals. A picture of the sADC prototype is shown

in Fig. 6.4. For the use with photodetectors as foreseen for the $\bar{\text{PANDA}}$ EMC, the implemented feature extraction algorithm is able to extract the corresponding energy to the pulse and hence leads to a significant data reduction. Nevertheless, the original feature extraction algorithm is not applicable for signals from other photodetectors with different pulse shapes e.g. SiPMs. Therefore the ADC is operated in a pileup-mode: With the adjustment of certain parameters inside the firmware, the ADC treats every signal as a pileup and does not perform feature extraction, but sends out the complete waveform containing each sample of the wave (see Fig. 6.5, the data format is shown in the appendix B.1).

The sample height threshold, the minimum and maximum number of samples per wave can be adjusted inside the firmware. In order to communicate with the Compute Node (see section 6.3) an interface for the optical output using the AURORA protocol [94], which uses 8B/10B encoding and allowing for data transfer rates up to 3.125 Gb/s, was written.



Fig. 6.4.: A picture of the sADC prototype developed by Pawel Marciniewski.

6.2.1. ADC Linearity

The linearity of the ADC is of great importance for the performance of the DAQ setup. It was tested using a pulser with adjustable pulse form and pulse height. As can be seen in Fig. 6.6, the sADC responds quite linearly to the input pulses (black points mark the adc channel, the corresponding linear fit is drawn in red) and shows saturation effects for pulses with heights above 2000 mV, which is caused by analogue clipping. The effective differential nonlinearity of the sADC is drawn in blue.

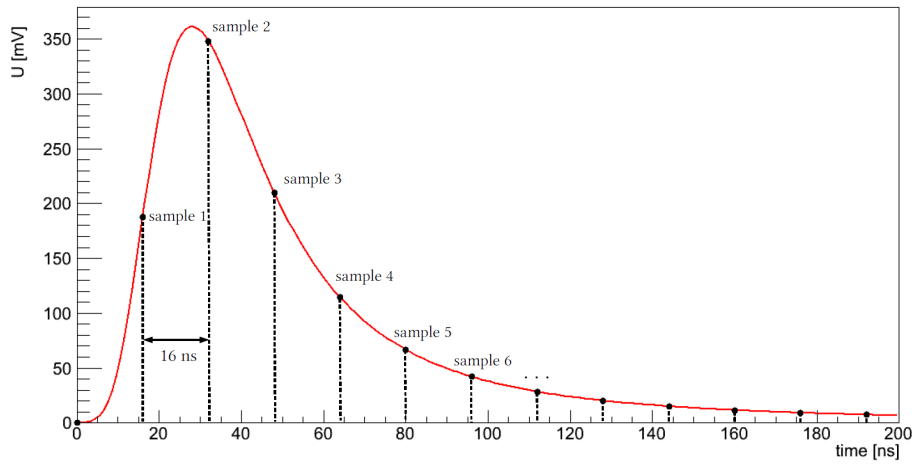


Fig. 6.5.: Example waveform with sampling points seen by the sADC. Every 16 ns a sample is taken, corresponding to 62.5 MHz sampling frequency.

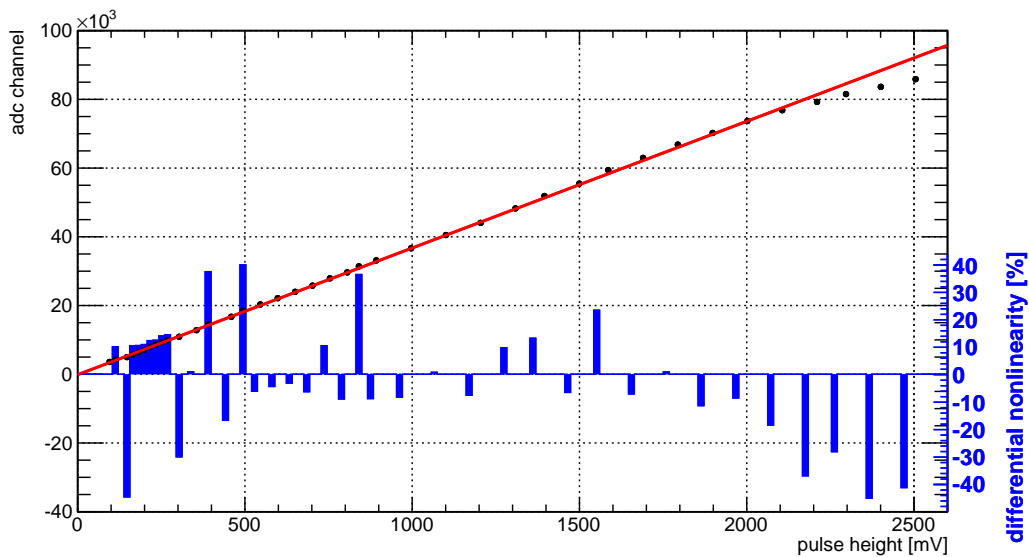


Fig. 6.6.: Histogram showing the linearity and the differential nonlinearity of the ADC: 39 input pulses with same shape, but different heights were chosen as input, the adc channel corresponds to the sum of all pulse samples recorded by the sADC. Pulses with sample heights above 2000 mV produce analog clipping: the sADC does not respond linearly anymore, but shows saturation effects.

Via an optical link and a speed of 3.125 Gb/s the data is then transferred to a Compute Node.

6.3. The Compute Node (CN)

The Compute Node (CN) is a multi-purpose FPGA-based hardware being collaboratively developed by IHEP, Beijing and II. Physikalisches Institut, JLU Giessen. The current version uses four AMC cards using xTCA standard, each holding one Virtex5 fx70T FPGA as well as a RAM slot supporting up to $2 \times 2\text{GB}$ DDR2 RAM, four SFP+ cages for e.g. optical links with up to 6.25 Gb/s and one RJ45 gigabit Ethernet connector. A carrier board holding the AMC cards is equipped with a Xilinx Virtex 4fx60 FPGA and provides the (inter-)connections between all AMC cards and the AdvancedTCA backplane. For the prototype setup, only one xTCA card is being used, for the whole cZDD detector as explained in chapter 4, more cards and a carrier board are needed to synchronize all DAQ modules. For convenience the AMC card used for the prototype DAQ is referred to as CN. A picture of an AMC card and a fully equipped carrier board is shown in Fig. 6.7.

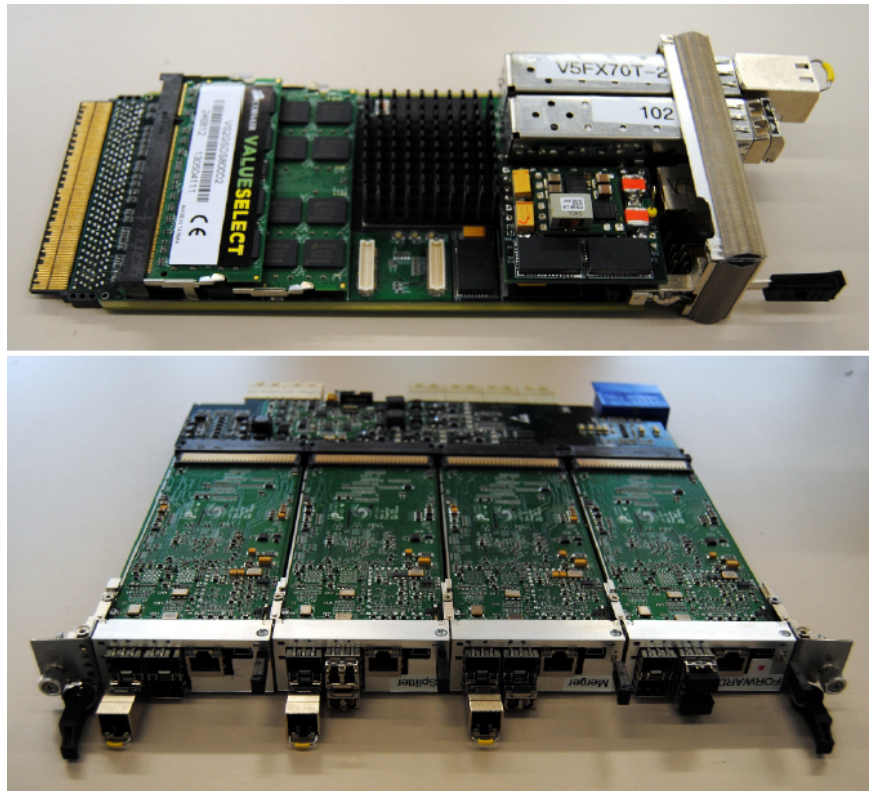


Fig. 6.7.: An AMC card equipped with $2 \times 2\text{GB}$ DDR2 RAM, one SFP+ optical transceiver and one SFP+ transceiver for RJ45 cables (upper picture). The lower picture shows a aTCA carrier board fully equipped with four AMC cards.

6.3.1. Workflow On The CN

The data coming from the sADC is being received by the AURORA module on the CN side. From there on, the 32 bit data is pipelined into a **data extractor**, which checks parity bits and CRC codes and puts out 36 bit words, where bits (36 ... 32) hold information on which part of the wave is contained in the word, the encoding can be found in Tab. B.1. These 36 bit words are then processed by an **event builder** module, which performs background suppression and event building based on programmable criteria explained in greater detail in section 6.3.2. All waves of one event are given an event number and the data is converted into 32 bit words, which are then buffered in the RAM via a memory controller and buffer management modules provided by T. Gessler and B. Spruck. The SiTCP Kernel collects the data from the buffer and sends it to the PC for storage as soon as a connection to a PC has been established. An overview of this procedure is given in Fig. 6.8

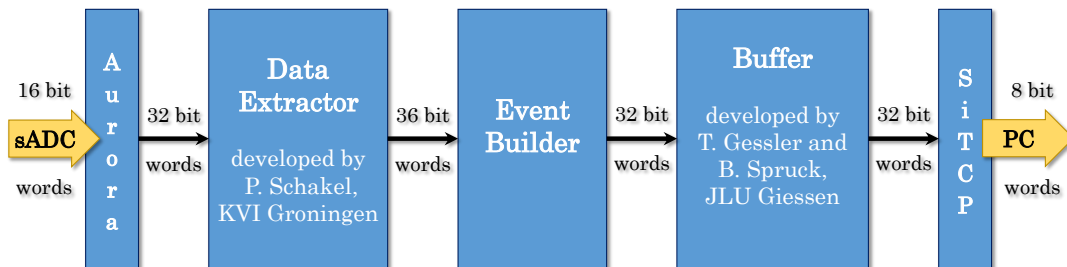


Fig. 6.8.: Schematic diagram depicting the workflow on the CN.

6.3.2. Event Builder

The event builder is the “heart” of the DAQ and decides which waves are to be kept and which ones are to be neglected. The event building algorithm works as follows: As soon as the first wave arrives, its time stamp is stored, an additional *new event candidate* flag is set to '1' and added to the 36 bit word. This 36+1bit word is buffered in a First-In-First-Out Memory (FIFO). The new event candidate flag is set to '0' and all subsequent words are written into the FIFO until the time stamp of the next wave arrives. This time stamp is then compared to the stored one and if it lies inside the coincidence window, it is marked as valid (= time stamp lies within coincidence window), whereupon event properties are updated and the wave is also stored in the FIFO. Furthermore it is checked whether all event conditions are fulfilled. If not then the next valid waves are also checked until all event conditions are fulfilled. After this has happened, a '1' is written into a second FIFO, which contains event valid or not valid information. If a wave with a non-valid time stamp (=time stamp not within allowed window) arrives during the process, the stored time stamp for comparison is

replaced by the current one, all event flags are resetted, a '0' is written into the second FIFO and the new event candidate flag is set to '1' again. And since every first word of a new event candidate is marked with the new event candidate flag, the relationship of contents from first FIFO and second FIFO can be used for precisely filtering out all waves containing background (=not all event conditions fulfilled) and keeping waves belonging to a real event. The latter events are buffered into another FIFO before the words are converted into 32 bit and stored in the RAM of the CN. The generics defining the event conditions are summarized in Tab. 6.1, the flow diagrams explaining the event building algorithm are shown in Fig. 6.9 and Fig. 6.10.

The event builder described in this section could be used as the sub-event builder for the cZDD DAQ described in Fig. 4.14: It could filter, gather and combine the data from the cZDD before correlation with BESIII trigger data is done on the CN. Depending on the final resources, which would be needed for the sADC logic, this step may already be done on the FPGA of the sADC.

Generic	TYPE	Function
OFFSET	natural	defines the time window, in which all time stamps of correlated waves must reside
COINC	std logic vector	Which channels <u>must</u> fire?
CHANNELS	natural	How many PMT channels <u>must</u> fire (at least)?
DOWNSCALER	natural	Keep only every DOWNSCALER'th <u>event</u>

Tab. 6.1.: Explanation of the event builder's generics, which define the criteria for event building.

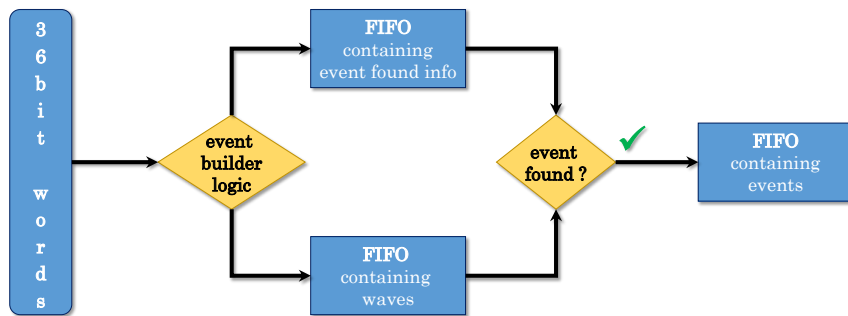


Fig. 6.9.: Flow diagram of the event builder program: The 36bit input words encoding the waveform are analyzed by an event builder logic, which sends all incoming words into a FIFO. Depending on the required event conditions it fills another FIFO with a TRUE/FALSE information whether the wave belongs to a valid event or not. The event builder logic is explained in Fig. 6.10. Event building can then be done by correlating entries from both FIFOs.

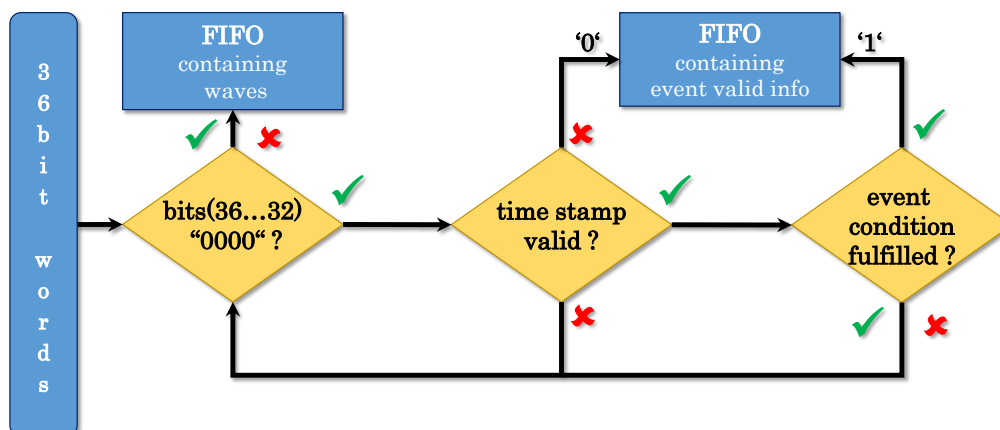


Fig. 6.10.: The event builder logic: If a new time stamp arrives (= bits(36...32)="0000"), it is compared to the stored one. If it lies within the allowed window, the event conditions are checked. If all event conditions have been fulfilled, an *event* has been found and a '1' is written into a FIFO. If the time stamp is not valid and/or not all conditions have been fulfilled, a '0' is stored in the FIFO, the stored time stamp is replaced by the current one and the procedure begins again.

6.4. PC-based Data Analysis

All accepted data is transmitted from the CN to a PC via SiTCP [95], which allows for data transfer rates up to 1 Gb/s. In order to guarantee the full bandwidth, the data is directly written onto disc in binary format. A data interpreter program then reads in and processes the serial data. The sADC's data format has been given in section 6.2. In order to correctly interpret the data, the architecture of the data interpreter is a *Mealy-state-machine*: its behaviour is depending on its actual state and the input. The flow diagram of the data interpreter is shown and explained in Fig. 6.11. Whenever an error occurs, all data from the actual waveform is neglected and the state machine is reset. If a valid waveform has been found, the time stamp, event number, adc channel, number of samples and the energy channel, which is the sum of all samples, are written into a ROOT file for further data analysis.

The functionality of the DAQ developments described in this chapter has been tested in several experiments using radioactive sources, cosmic rays and electrons delivered by an accelerator. The respective experimental setups and results are described in the next chapter.

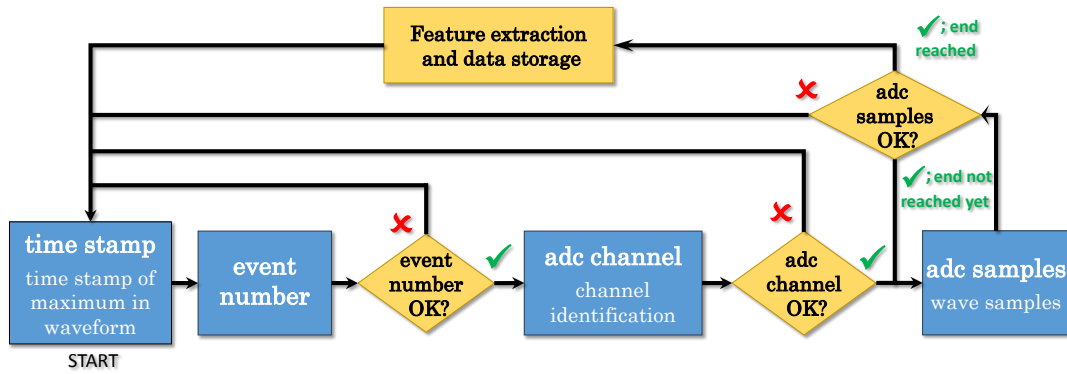


Fig. 6.11.: Flow diagram of the data-interpreter program : For valid data the waveform data has to begin with a time stamp and an event number. The ADC number and the data samples follow, which all have certain control bits to determine which part of the waveform is analyzed at the moment. Whenever there is an error word (see Tab. B.2) or any discrepancy between what is expected by the program and what actually is the input, an error message is printed out and the program is reset to the initial state, which is the time stamp state.

TEST EXPERIMENTS AND RESULTS

As already mentioned, this chapter is about test experiments done with the prototype detector and the DAQ explained above. The prototype detector does not have the same properties as the final cZDD, and the firmware for the sADC and the CN are first prototype test modules, which will be extended and refactored for the final version. Hence, the focus of the experiments does not lie on determining the specific capabilities of the prototype detector and the DAQ chain, but on their principal functionality.

7.1. Tests with Radioactive Sources

The most important property of the prototype detector is its capability to measure the energy deposition in a scintillator crystal, when the crystal is hit by an interacting particle (charged particles, photons). Radioactive sources (e.g. ^{22}Na , ^{60}Co , ^{137}Cs) can be used as “particle guns“, which deliver those interacting particles with typical energies from 100 keV up to 1.5 MeV.

Unfortunately, PbWO_4 crystals have a major drawback when measuring particles from radioactive sources: PbWO_4 has a very low light yield at room temperature (15 - 19 scintillation photons / MeV). Regarding the properties of the SiPMs and the effective readout area, this results in less than 10 photons per MeV, which are seen by the SiPMs. Practically, measurements of radioactive sources with PbWO_4 will not yield satisfactory results. For that reason, a different scintillator with much bigger light yield has been used for those tests. The whole DAQ chain including photodetectors and front end electronics remained the same, but the photodetectors were mounted on a LYSO scintillator, whose properties are summarized in the next section.

7.1.1. Properties of LYSO

The rare-earth scintillator lutetium-yttrium oxyorthosilicate ($\text{Lu}_{2(1-x)}\text{Y}_{2x}\text{SiO}_5$, short LYSO) is being used for tests with radioactive sources. The material's main properties are summarized in Tab. 7.1. Its density, radiation length and peak wavelength is similar to that of PbWO_4 , but its relative light yield is much higher (compare to Tab. 2.1), making it a suitable choice for replacing the PbWO_4 crystal in the test with radioactive sources.

density ρ	7.40 g/cm ³
radiation length X_0	1.14 cm
Molière radius R_M	2.07 cm
decay time τ	40 ns
wavelength (at peak) λ_{max}	420 nm
relative lightyield (compared to NaI)	85 %

Tab. 7.1.: Main properties of the LYSO crystal being used for tests with radioactive sources [96].

Unfortunately, lutetium naturally occurs in form of two isotopes: the stable ^{175}Lu isotope ($\sim 97.5\%$) and the radioactive ^{176}Lu isotope ($\sim 2.5\%$), which decays via β -decay with a half-life of $3.78 \cdot 10^{10}$ years. Thus, the LYSO crystal itself is radioactive and radiates with a rate of several $k\text{Bq}$. The decay scheme of ^{176}Lu can be found in Fig. 7.1: after the β -decay a cascade of three or four photons is emitted before the nucleus of ^{176}Hf populates the ground state.

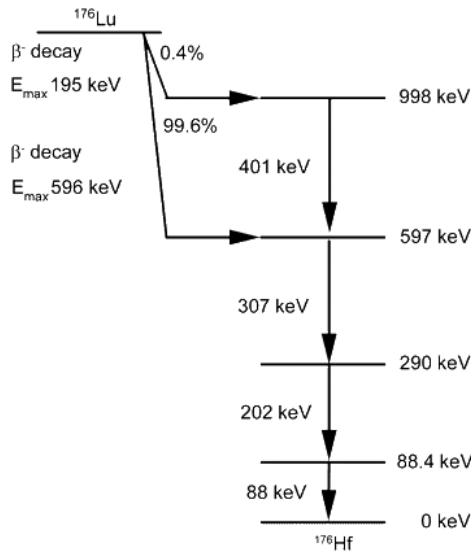


Fig. 7.1.: Decay scheme of ^{176}Lu

For the measurements this means we must deal with background coming from the LYSO self-activity.

7.1.2. Experimental Setup

In order to reduce the influence of ^{176}Lu background, a coincidence setup as depicted in Fig. 7.2 has been chosen: Beside the LYSO crystal, which is read out by two SiPMs, another BaF_2 scintillator is read out by a standard PMT. If a radioactive source creates a cascade of almost coincident particles (photons or positrons) (e.g. ^{22}Na and ^{60}Co sources), in some of the cases one particle deposits its energy in the LYSO crystal, whereas the other particle gets absorbed in the BaF_2 crystal. The event builder is then programmed in a way that it only accepts events when both SiPMs mounted on the LYSO and the PMT mounted on the BaF_2 have fired coincidentally. The signal from the PMT is not used for the further data analysis, but has the function of a VETO, when there is no signal in the BaF_2 . This setup will not filter out all photons coming from ^{176}Lu decays, since this decay also leads to a cascade of several photons, but it will significantly reduce the amount of those events in the spectra.

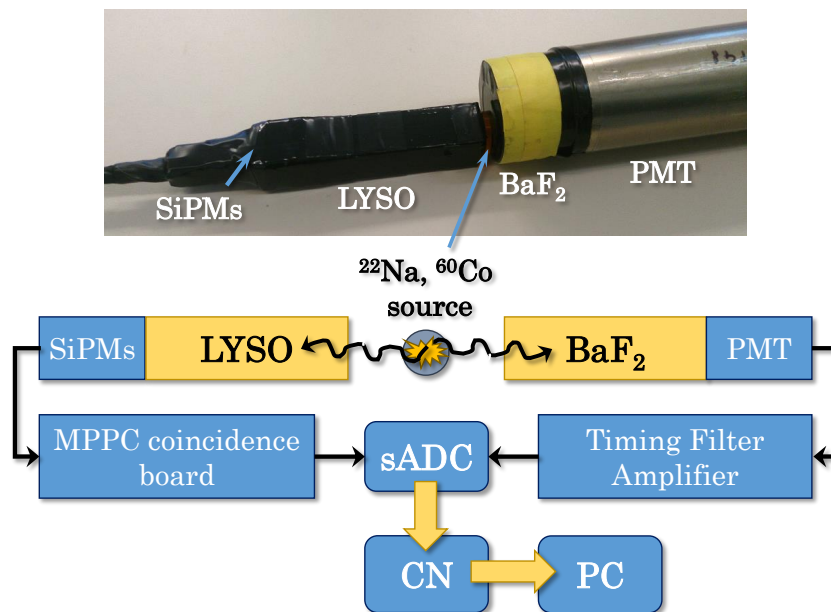


Fig. 7.2.: Experimental setup for the test with radioactive ^{22}Na and ^{60}Co sources. The timing filter amplifier shapes the signal of the PMT for better digitization results.

The LYSO crystal has a quadratic cross section of $2.5 \times 2.5 \text{ cm}^2$ and a total length of 13 cm ($\sim 11.4 X_0$). Using the SiPM setup from chapter 6 with a total photosensitive area of $2 \times 9 \text{ mm}^2$, only 2.88% of the end face is covered with SiPMs. Thus, we ex-

pect a rather bad energy resolution, because the photon sample we are collecting is so small. However, this test has been performed in order to verify the scintillator readout concept with SiPMs on a qualitative base. If we can see that the energy spectra from different sources look differently, we know the SiPMs are sensitive to the deposited energy in the scintillator.

Beside the measurement of ^{22}Na and ^{60}Co , the scintillation light output of LYSO was measured without an additional radioactive source, which corresponds to a measurement of the ^{176}Lu cascade. For this last case the PMT signal was not used. The respective parameter settings of the event builder used for these tests can be seen in Tab. 7.2. SiPM1 was operated with a bias voltage 73.2V and SiPM2 with a bias voltage of 73.3 V. The supply voltage of the preamp was set to 5 V, the MPPC board thresholds were set to 45.6 mV (ch1) and 46.7 mV (ch2). The PMT was operated at a voltage of -1950 V.

Generic	setting ^{22}Na , ^{60}Co	setting LYSO
OFFSET	10	10
COINC	"00000011"	"00000011"
CHANNELS	1	0
DOWNSCALER	1	1

Tab. 7.2.: Event builder settings for the tests with radioactive sources: The time stamps must lie in a window ± 10 around the base time stamp. This corresponds to a maximum time difference of $\pm 10 \cdot 16\text{ns} = \pm 160\text{ ns}$. Channels 1, 2 (= SiPM1, SiPM2) are demanded to fire, in the case of ^{22}Na and ^{60}Co one additional channel (=1 PMT) needs to fire coincidentally. The setting of the downscaler generic does not affect the setup here.

The decay schemes of ^{22}Na and ^{60}Co can be found in Fig. 7.3.

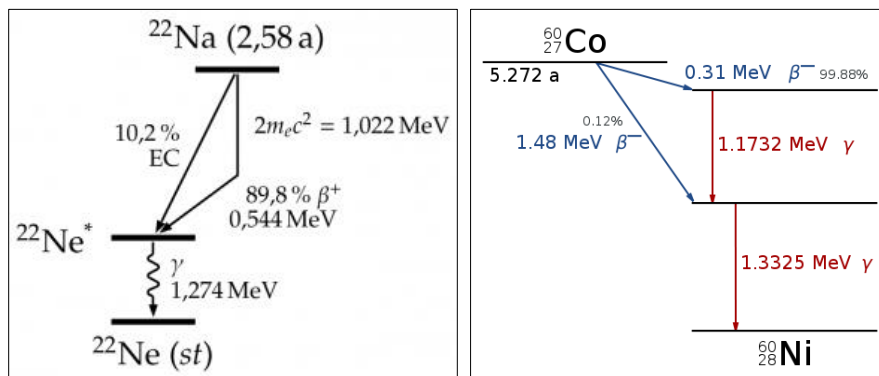


Fig. 7.3.: Decay schemes showing the transitions in ^{22}Na and ^{60}Co decays.

7.1.3. Energy Calibration with ^{22}Na

For the energy calibration of the adc channels, a sodium source has been used. Sodium is a β^+ -radiator and has a big annihilation peak at 0.511 MeV in the adc channel spectrum. Another peak comes from the relaxation transition of the excited neon nucleus, which emits a 1.274 MeV photon.

For the energy calibration, the peaks of the adc channel spectra have been fitted to the expected energies from the decay scheme. With the known energies of the sodium spectrum, a linear function can be constructed for the conversion into energy.

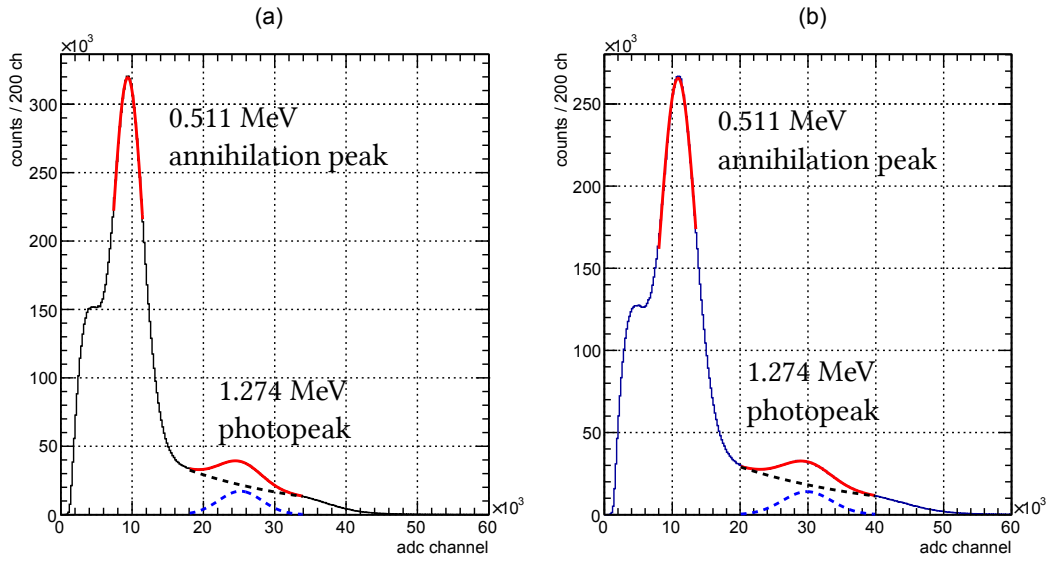


Fig. 7.4.: ADC channel spectra of ^{22}Na : the left plot is the spectrum of SiPM1, the plot on the right depicts the spectrum recorded by SiPM2.

The first peak has been fitted with a gaussian, the second peak with a gaussian and an exponentially falling background function. The adc channel spectrum of each SiPM and the fits are shown in Fig. 7.4, the corresponding energy spectra are depicted in Fig. 7.5, the fit functions and obtained parameters are summarized in App. C.1.1. The following linear fits for the adc channel (c) \leftrightarrow energy (E) correlation have been obtained:

SiPM1:

$$E_{\text{SiPM1}} = \frac{c + 1144.788257}{20659.25295}, \quad E_{\text{SiPM1}} \text{ in MeV}, \quad (7.1.1)$$

SiPM2:

$$E_{\text{SiPM2}} = \frac{c + 1865.859631}{24896.98558}, \quad E_{\text{SiPM2}} \text{ in MeV}, \quad (7.1.2)$$

After this energy calibration both spectra have the same scale and the energies of the single SiPMs can be added (see Fig. 7.5(c)). This final spectrum can then again be linearly fitted to the corresponding peak energies and one arrives at the

two channel sum: ($c = E_{\text{SiPM1}} + E_{\text{SiPM2}}$)

$$E = \frac{c - 0.02182486276}{1.993630406}, \quad E \text{ in MeV}, \quad (7.1.3)$$

which reflects the total scintillation light measured by both SiPMs. The resolution for the two channel sum will be better than the resolution of the single channels, since a larger sample of the scintillation light per event is considered. Since the calibration remained the same, equations 7.1.1, 7.1.2 and 7.1.3 can be used to obtain the energy spectra of ^{60}Co and ^{176}Lu .

7.1.4. Measurements of ^{60}Co and ^{176}Lu

For the measurement of ^{60}Co a thin aluminium plate (thickness < 1 mm) has been put between source and LYSO crystal in order to absorb the β electron, which would distort the spectrum. Fig. 7.6 shows the obtained energy spectra for ^{60}Co . The photopeak of the 1.173 MeV/1.333 MeV line was fitted with an exponentially falling background, as was used for ^{22}Na . The obtained fit results can be found in Tab. C.3. The two photopeaks from ^{60}Co cannot be resolved, which results in a single peak for the 1.173 MeV/1.333 MeV photons with a measured mean value of 1.297 MeV, which is in good agreement with what we would expect from the photon energies. The corresponding spectra of the LYSO self-activity is depicted in Fig. 7.7. Again, there are no separated peaks for the nucleus transitions (0.088 MeV, 0.202 MeV, 0.307 MeV, 0.401 MeV), but a single peak at ~ 0.936 MeV (see Tab. C.4), which corresponds to the energy deposited by three photons (in 99.6 % of all decays only three photons are emitted ($\sum_i E_i = 0.597$ MeV, see Fig. 7.1)) and the electron of the β -decay ($E(e)_{\text{max}} = 0.596$ MeV). Once more, the spectrum seems to be in accordance with the expected outcome of the LYSO self-activity.

Despite the bad energy resolution of the setup (as was expected), this experiment proved the SiPM's capability to measure a sample of the scintillation light produced by an incident particle/photon. All three sources create a different and source specific energy spectrum. This test also demonstrated the improvement of the energy resolution by using two instead of one SiPM for the readout (see App. C.1.1 for resolution results).

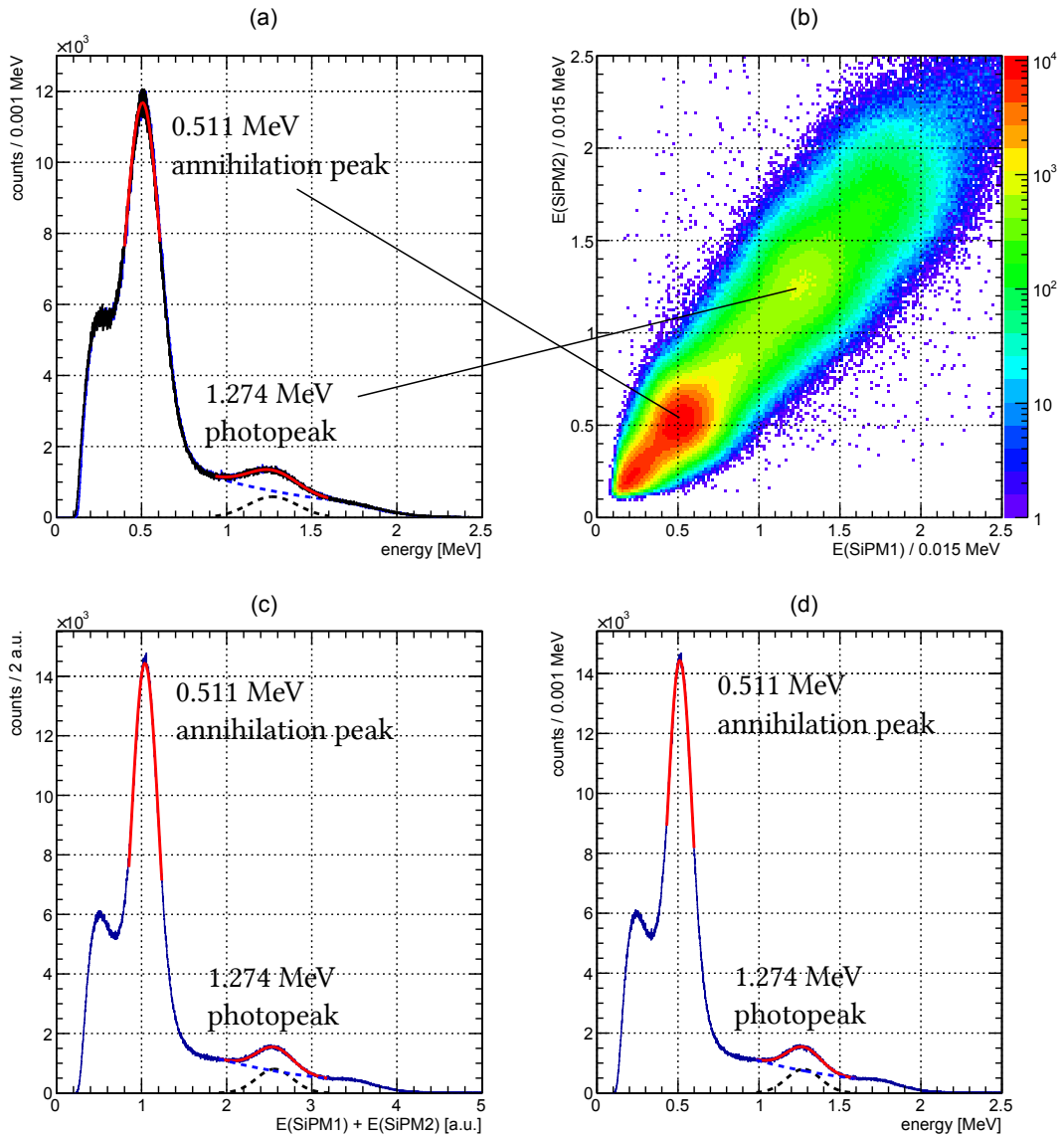


Fig. 7.5.: Measured energy spectra of ^{22}Na : (a) shows the single channel spectra of SiPM1 (black) and SiPM2 (blue), both channels look quite similar, (b) shows the corresponding scatter plot, where the correlation of both channels can be seen. After the single channel energy calibration, both spectra have the same scale and can be added (c). Another energy calibration fit for this spectrum yields the final two channel energy spectrum for ^{22}Na , which is depicted in (d).

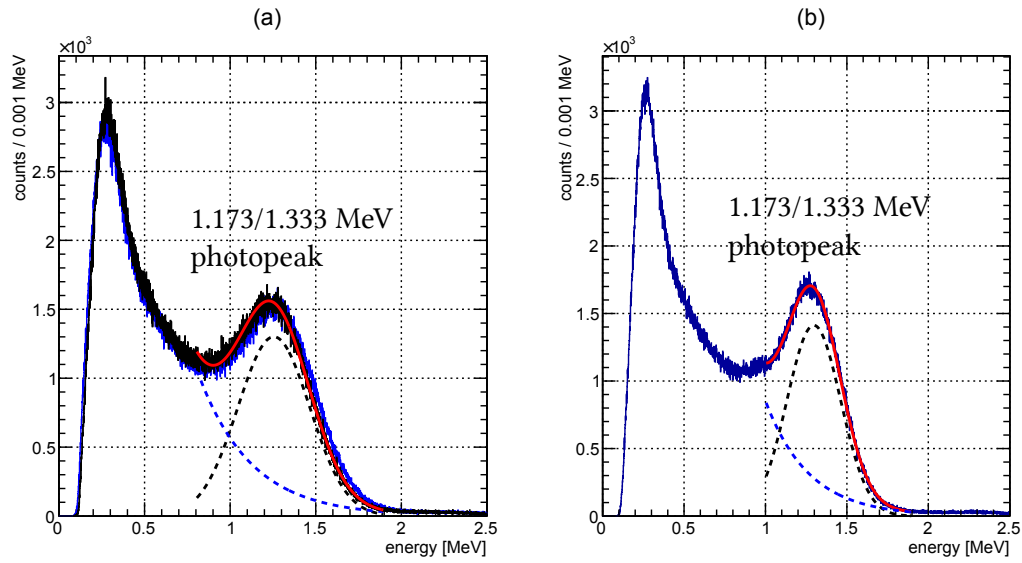


Fig. 7.6.: Energy spectra of ^{60}Co : (a) shows the single channel spectra of SiPM1 (black) and SiPM2 (blue), (b) shows the corresponding two channel sum spectrum of ^{60}Co .

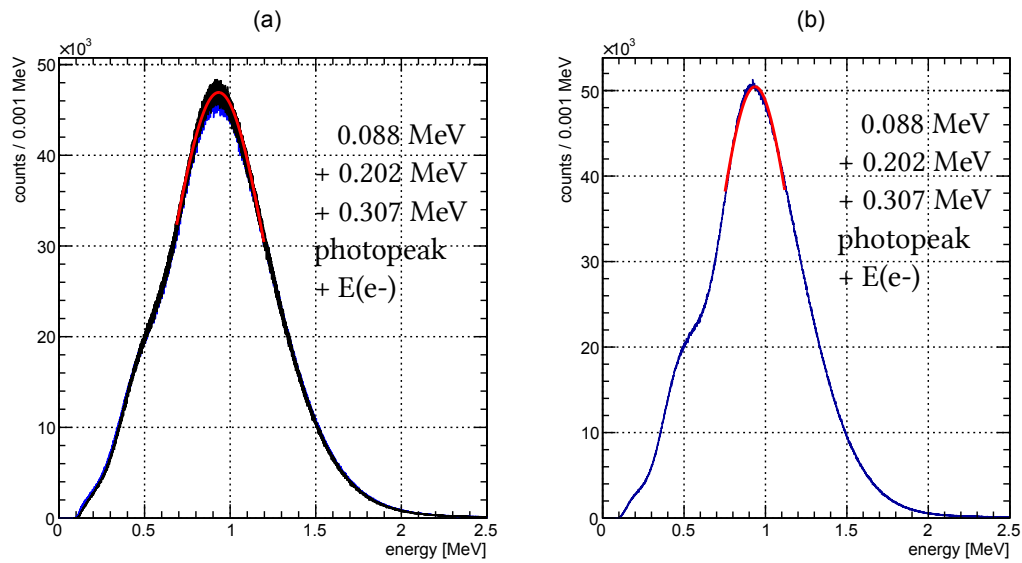


Fig. 7.7.: Energy spectra of ^{176}Lu : (a) shows the single channel spectra of SiPM1 (black) and SiPM2 (blue), (b) shows the corresponding two channel sum spectrum of ^{176}Lu .

After the basic functionality had been verified, the full prototype detector with PbWO_4 crystal, as described in chapter 6, was tested with a 210 MeV electron beam delivered by the Mainz Microtron (MAMI), located in Mainz, Germany.

7.2. Beamtest at MAMI

7.2.1. The Prototype Detector

The prototype detector for the beam test has already been introduced in chapter 6: a small PbWO_4 crystal of $1.5 \times 1.5 \text{ cm}^2$ end face is surrounded by four $\bar{\text{PANDA}}$ EMC endcap prototype crystals (dimensions: $2 \times 2 \times 15 \text{ cm}^3$), which are read out by standard PMTs. Since the properties of the small crystal are of primary interest, the surrounding crystals have been used for cosmic ray event building and for providing a more realistic environment, since they also have an influence on the energy deposition in the small crystal due to scattering secondary electrons and positrons. No further analysis concerning energy deposition or resolution of the surrounding crystals has been performed. The final prototype detector setup is shown in Fig. 7.8. In order to keep the detector structure as shown, wood blocks and shrinking tubes have been used for stabilisation.

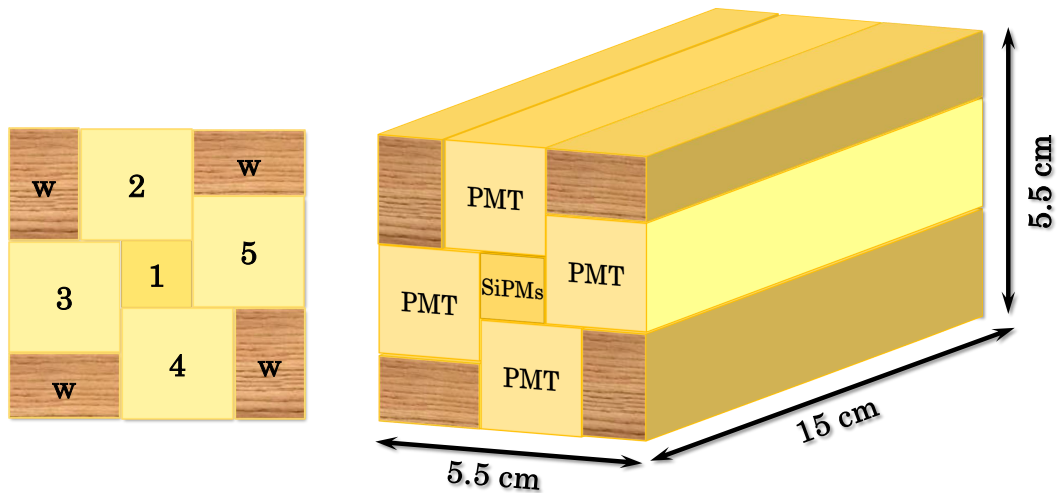


Fig. 7.8.: The structure of the prototype detector: The small crystal (1), read out by two SiPMs, is surrounded by four larger $\bar{\text{PANDA}}$ EMC endcap crystals (2-5), which will be read out by standard PMTs. In order to fix the crystals in their position, wood blocks (w) and shrinking tubes have been used.

7.2.2. The Mainz Microtron

The Mainz Microtron (MAMI), located at the campus of the Johannes Gutenberg university (JGU) in Mainz, Germany, is a particle accelerator for electrons and is operated by the institute for nuclear physics of the JGU. MAMI can deliver a continuous beam of (polarized) electrons with energies up to 1.5 GeV [97]. The accelerator consists of four stages, of which the first three are *racetrack microtrons*, and the fourth is a *harmonic double-sided microtron*.

The microtron principle works as follows: the electrons are accelerated by a linear accelerator with moderate gain. The flight path leads into two 180° bending magnets before the electrons get accelerated by the same linear accelerator again. Since the bending magnets provide a constant homogenous field, the bending radius of the electrons increases after each turn. Thus, each turn requires an extra beam line in order to guide the beam through the accelerator. The number of beam lines determines the maximum number of circulations and therefore the maximum energy of the electrons. At MAMI the e^- -beam can be extracted for experimentation after the third or the fourth stage. Several experiments use the electron beam or secondary photons from synchrotron radiation for investigating the structure of strongly interacting matter [97]. For our test, the detector was placed on a remote-controllable xy -table directly behind the third racetrack microtron (RTM3) (see Fig. 7.9).

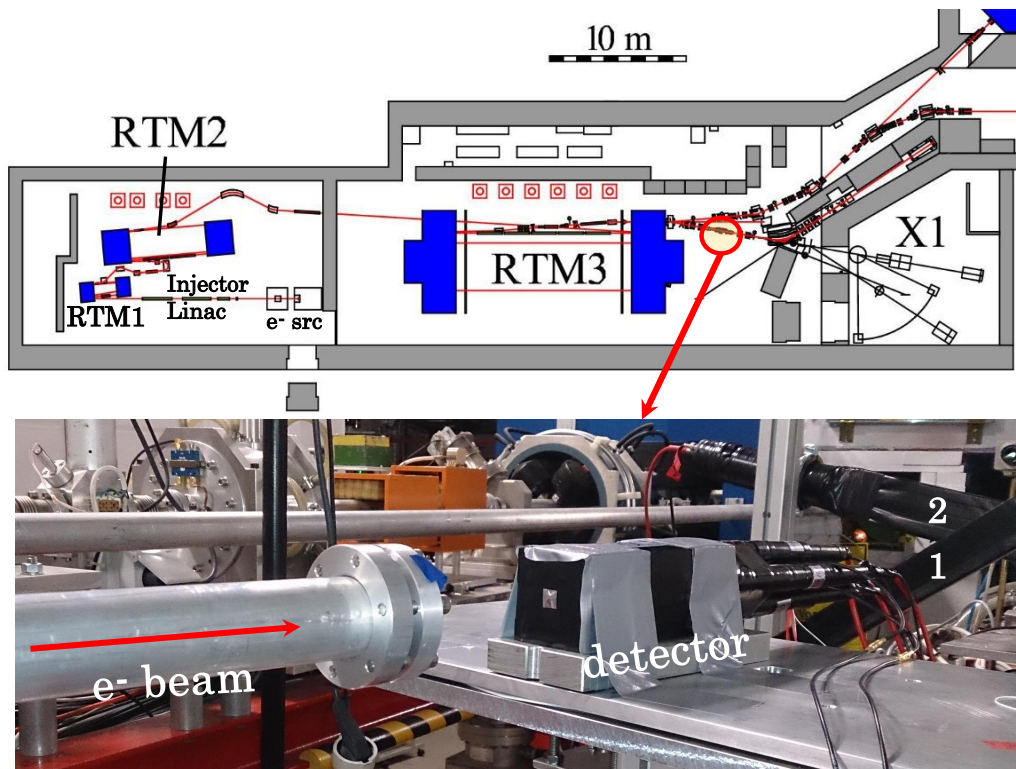


Fig. 7.9.: The detector is placed on a remote-controllable xy -table directly behind the third racetrack microtron (RTM3). The paddles 1 and 2 are plastic scintillator bars for rate determination, when the detector is moved out of the beam.

After the first two acceleration stages, the electron beam has an energy of 180 MeV. The beam then circulates four times in the RTM3 before it is extracted and the 210 MeV electrons are shot on the detector.

Unfortunately, during our short beam time at MAMI, which was approx. 10 hours in total, it was not possible to change the energy of the electrons. In order to extract information on the energy resolution of the small crystal, which needs at least two well-defined energy points, cosmic rays and the 210 MeV electrons were used for energy calibration.

Cosmic Rays

Cosmic rays are a constant source of high energy muons and can be used for energy calibration purposes almost everywhere (except for some experiments, which are located very deeply under the earth’s surface). Charged high energy particles (mostly protons, but also electrons and heavier nuclei [82]), which enter the earth’s atmosphere, produce hadronic/electromagnetic showers, which finally end up in neutrinos and electrons or muons, of which only the muons are able to travel through the atmosphere and reach the earth’s surface. Cosmic muons almost have a constant energy loss per cm when traveling through matter, leaving a peaked signal in the detector. If a cosmic muon hits the detector, coincident signals in three crystals of the detector can be seen, see Fig. 7.10.

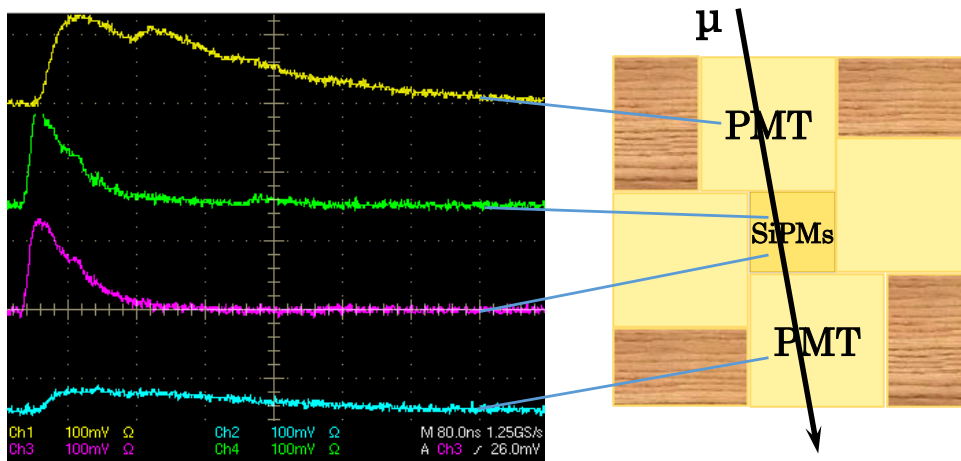


Fig. 7.10.: A cosmic muon has traveled through the detector: It leaves four coincident signals as marked in the figure.

7.2.3. Geant4 Simulations

In order to get an idea of how much energy a cosmic muon and the 210 MeV electrons will leave in the PbWO_4 crystal, Geant4 simulations have been performed. At the earth’s surface, the mean energy of cosmic muons is 4 GeV [82], but at MAMI, which is placed 10 - 15 m below the surface and surrounded by several meters of cement, it was assumed that the muons have an energy of 2 GeV ($\sigma = 500$ MeV). The Monte

Carlo (MC) truth results of the simulation are shown in Fig. 7.11. The signals were fitted with the Novosibirsk function, as already defined in Eq. (5.2.16).

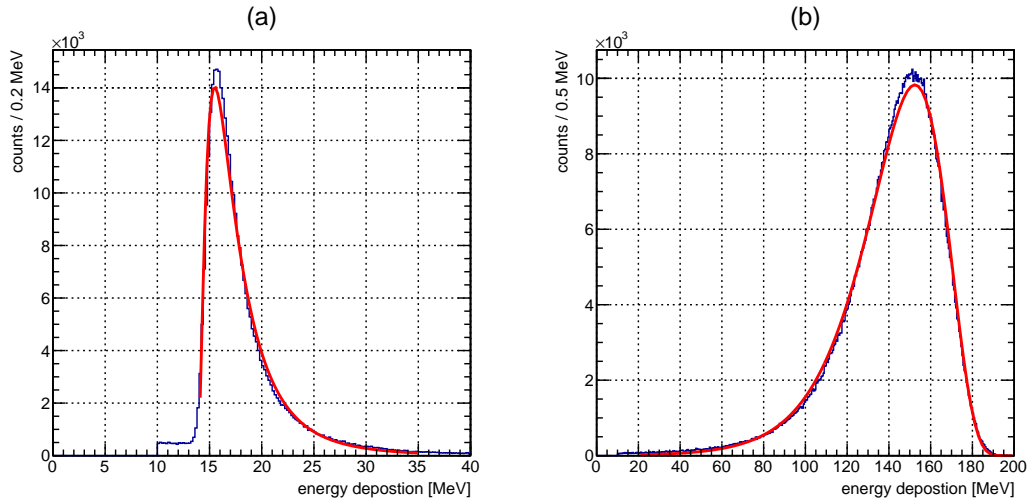


Fig. 7.11.: Energy deposited in the crystal by vertically traversing cosmic muons **(a)** and 210 MeV electrons horizontally shot onto the crystal center **(b)** (MC truth). The results are fitted with a Novosibirsk function (Eq. 5.2.16), the fit values can be found in App. C.2.1.

The results for μ and σ can then be used for extracting the conversion functions for the adc channel \leftrightarrow energy relation. Furthermore the relation σ/μ from MC-truth gives us the lower limit for the achievable resolution, which is solely determined by the detector's material and geometry. It has been estimated to be $(12.8 \pm 0.3) \%$ for 210 MeV electrons. The resolution of the prototype crystal including the whole digitization process as described in chapter 5 is plotted in Fig. 7.12 and determined to be $(17.5 \pm 0.7) \%$, the corresponding fit parameters can be found in App. C.2.1.

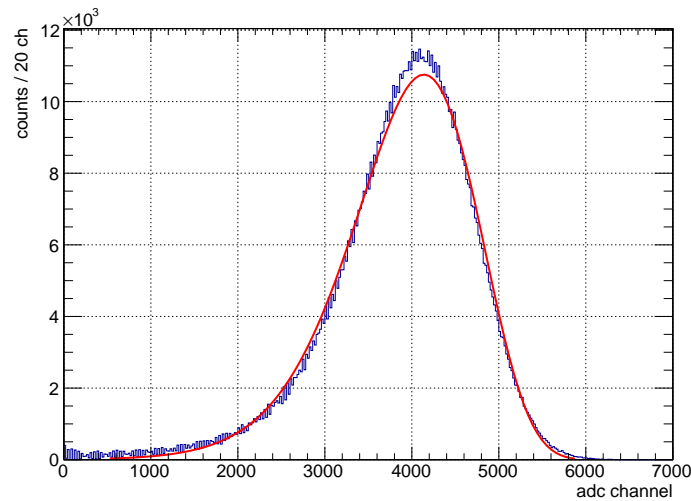


Fig. 7.12.: Obtained adc channel spectrum of the prototype crystal including the whole digitization process as described in chapter 5. The results are fitted with a Novosibirsk function (Eq. (5.2.16)), the fit values can be found in App. C.2.1.

7.2.4. Energy Resolution Measurements

The measurements at MAMI were performed with the following settings: The PMT voltages were set to -1350 V, the MPPC preamps were operated at 5V, the bias voltage of the SiPMs was set to 73 V and the comparator threshold settings of the MPPC coincidence board were set to 45.6 mV (SiPM1) and 46.7 mV (SiPM2). The sADC minimum number of samples was set to 10 and the maximum number of samples set to 70, the respective threshold was set to 50. Tab. 7.3 shows the event builder parameters used for the tests at MAMI. For the energy resolution measurements, the accelerator was running at a rate of approx. 3 kHz.

Generic	Cosmics setting	Electrons setting
OFFSET	10	10
COINC	"00000011"	"00000011"
CHANNELS	2	0
DOWNSCALER	1	1

Tab. 7.3.: Event builder settings for the measurement of cosmics/electrons: Two PMTs (CHANNELS = 2) have to fire beside the two SiPMs (COINC = "00000011") to form a valid cosmic event, whereas in the electron case only the SiPMs need to fire coincidentally.

Fig. 7.13 and Fig. 7.14 show the obtained adc channel spectra for cosmics and

electrons. The muon spectra were fitted using a standard gaussian, whereas for the electrons the Novosibirsk function was used. All corresponding fit values can be found in App. C.2.1.

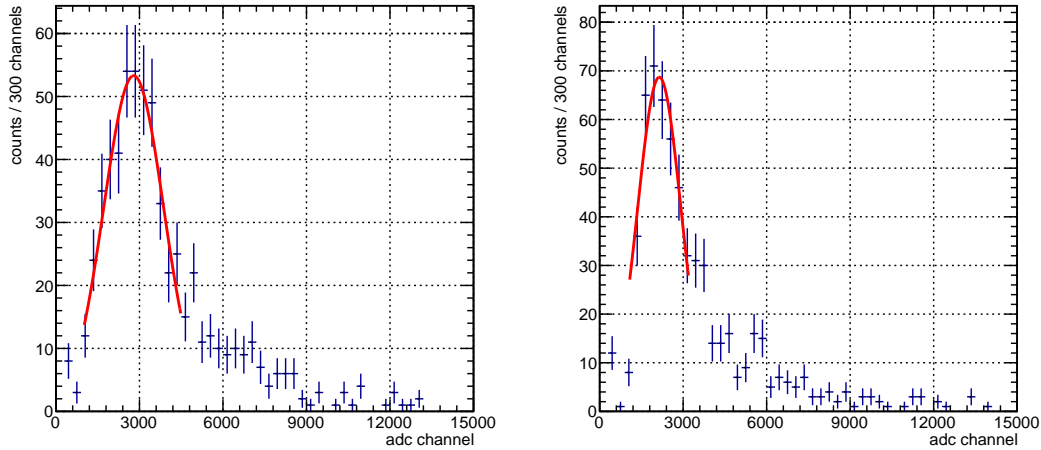


Fig. 7.13.: Obtained measurements for cosmics: (a) shows the spectrum measured by SiPM1, (b) the spectrum measured by SiPM2. The spectra are fitted with a standard Gaussian, the fit values can be found in App. C.2.1.

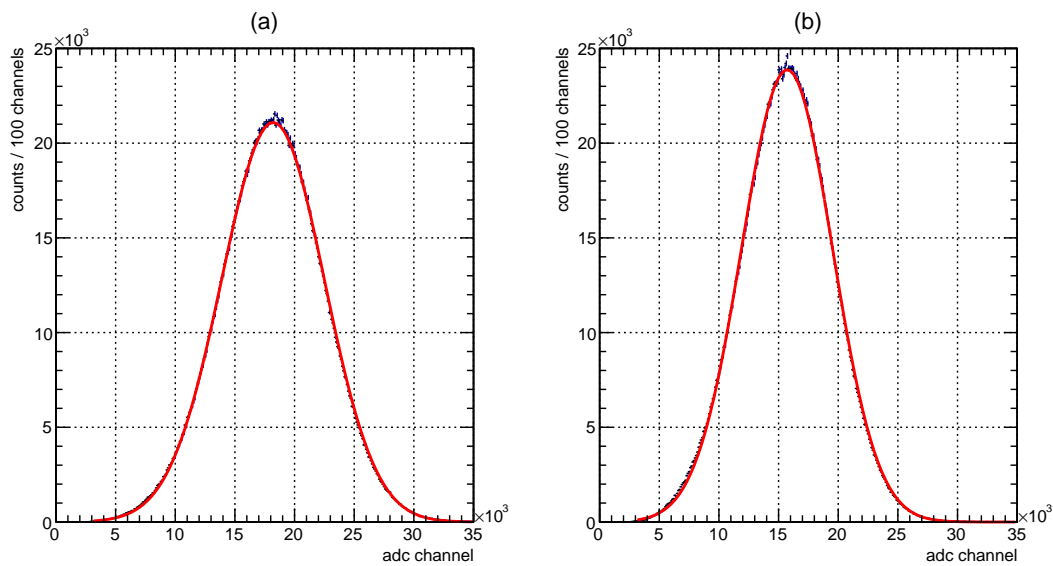


Fig. 7.14.: Obtained measurements for 210 MeV electrons: (a) shows the spectrum measured by SiPM1, (b) the spectrum measured by SiPM2. The results are fitted with a Novosibirsk function (Eq. (5.2.16)), the fit values can be found in App. C.2.1.

Now that we know the adc channels for the corresponding energies of the MC simulation (see Fig. 7.11), we can use a linear fit in order to get the conversion function for the adc channel \rightarrow energy calibration. The error bars were set to the sigma of the corresponding distribution. Additionally to the two measured points the 0-point was used for fitting. For that 0-point, the error bar Δx was set to 500 channels (10 samples times 50 (sample height) (minimum number of samples times adc value threshold), which corresponds to the minimum adc channel to be recognized by the ADC, Δy of 0 was set to 10 MeV, which approx. corresponds to the minimum measurable energy of the detector. The linear adc channel (c) \rightarrow energy (E) fits for SiPM1 and SiPM2 can be seen in Fig. 7.15, the resulting linear fits are

$$E(\text{SiPM1}) = 8.15660 \cdot 10^{-3} \cdot c - 4.08703, \quad E \text{ in MeV}, \quad (7.2.1)$$

$$E(\text{SiPM2}) = 9.52407 \cdot 10^{-3} \cdot c - 3.21196, \quad E \text{ in MeV}. \quad (7.2.2)$$

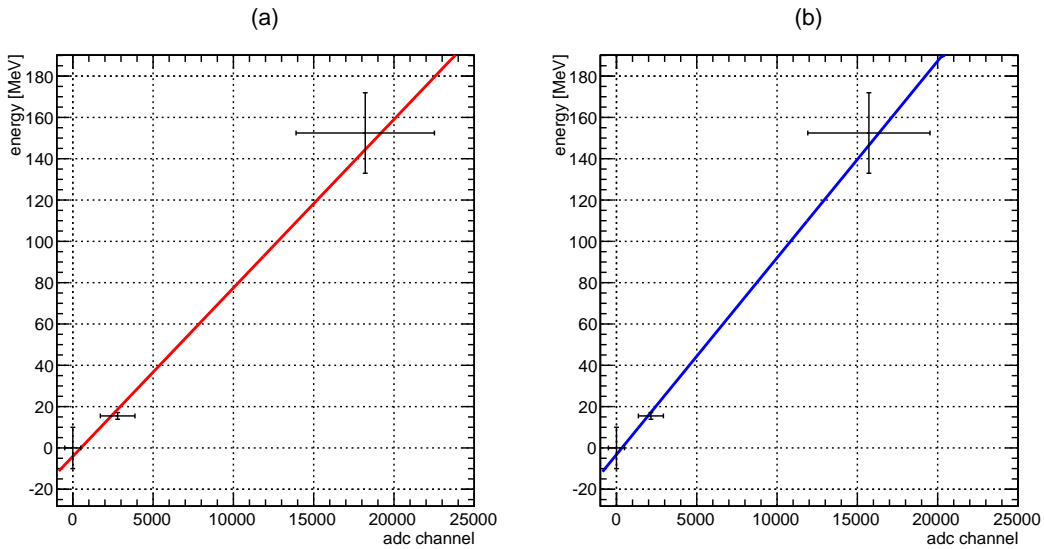


Fig. 7.15.: Linear energy calibration fits for SiPM1 (a) and SiPM2 (b).

After this first energy calibration, the obtained energy spectra for the single SiPMs can be added, fitted and calibrated with the MC data again (Fig. 7.16), the second linear energy calibration function reads as

$$E = 5.06856 \cdot 10^{-1} \cdot c - 2.80698 \quad (7.2.3)$$

$$c = E(\text{SiPM1}) + E(\text{SiPM2}) \quad .$$

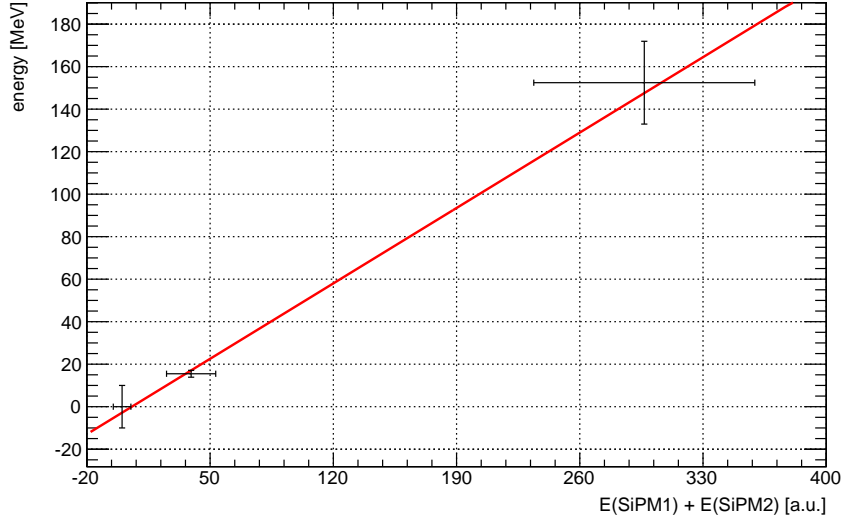


Fig. 7.16.: Linear fits for the two SiPM energy calibration.

The fit results for the two channel energy spectra can be found in Tab. 7.4, the single SiPM energy spectra, the SiPM sum spectra and the final two channel energy spectra can be found in Fig. 7.17 (cosmic muons) and Fig. 7.18 (210 MeV electrons).

Parameter	cosmic muons	210 MeV electrons
A	$4.881 \cdot 10^1$	$1.427 \cdot 10^4$
μ	$1.655 \cdot 10^1$	$1.476 \cdot 10^2$
σ	7.537	$3.185 \cdot 10^1$
τ	–	$- 6.915 \cdot 10^{-2}$
$\Delta\sigma$	$\pm 6.784 \cdot 10^{-1}$	$\pm 1.534 \cdot 10^{-2}$
$\Delta\mu$	$\pm 5.212 \cdot 10^{-1}$	$\pm 3.024 \cdot 10^{-2}$
σ/μ	$45.5 \pm 4.3 \%$	$21.6 \pm 0.01 \%$

Tab. 7.4.: Fit parameters obtained for the final two SiPM energy spectra for cosmic muons and 210 MeV electrons (Fig. 7.17 (d) and Fig. 7.18 (d)). Due to the bad statistics, the obtained total resolution for the cosmic muons is worse compared to those of the single SiPM spectra (see Tab. C.8). This can happen when the systematic errors introduced by the energy calibration procedure are bigger than the gain in statistics.

For comparison, data with an electron impact outside of the small crystal has also been collected. Fig. 7.19 shows the total measured energy when the impact position of the electrons is shifted 1 cm to the left (a) and when it is shifted 1 cm downwards (b). In comparison with Fig. 7.18 (d) we can see the detector’s sensitivity to impact position shifts of the beam and therefore its capabilities to measure energies.

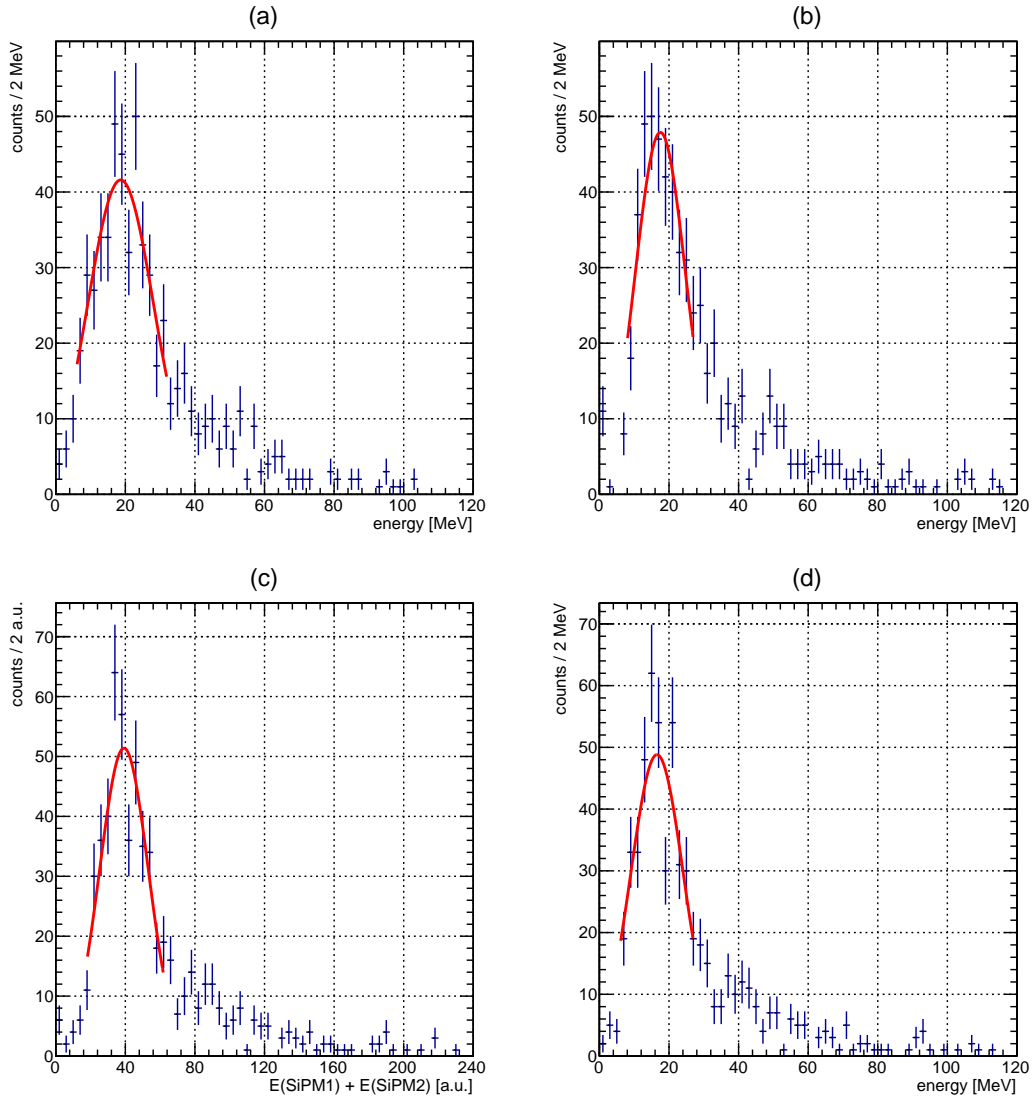


Fig. 7.17.: Fits of the cosmic muon energy spectra obtained by SiPM1 (a) and SiPM2 (b). (c) shows the sum of both distributions and (d) depicts the final two SiPM energy spectrum obtained for the cosmic muon measurements using the energy calibration from Eq. (7.2.3).

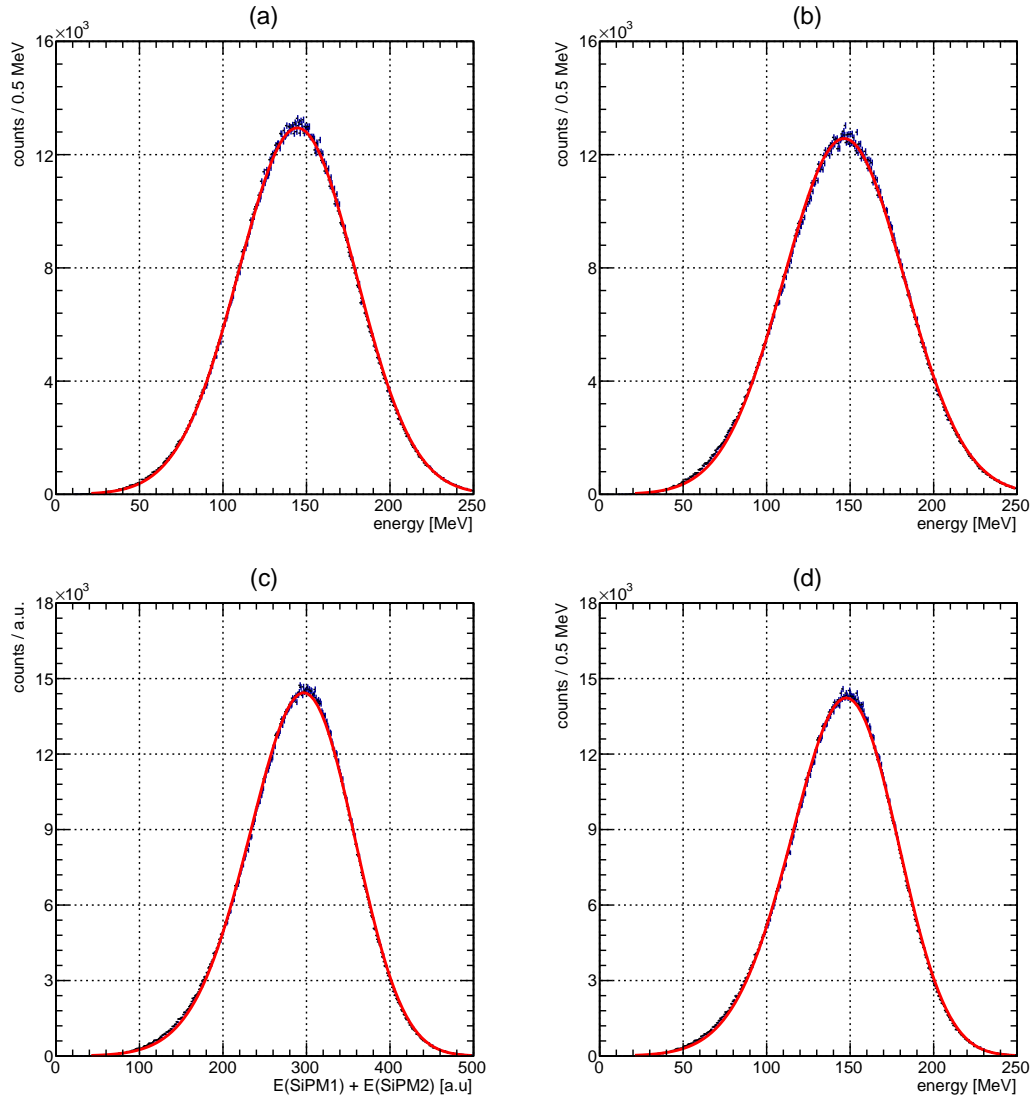


Fig. 7.18.: Fits of the 210 MeV electron energy spectra obtained by SiPM1 (a) and SiPM2 (b). (c) shows the sum of both distributions and (d) depicts the final two SiPM energy spectrum obtained for the 210 MeV electron measurements using the energy calibration from Eq. (7.2.3).

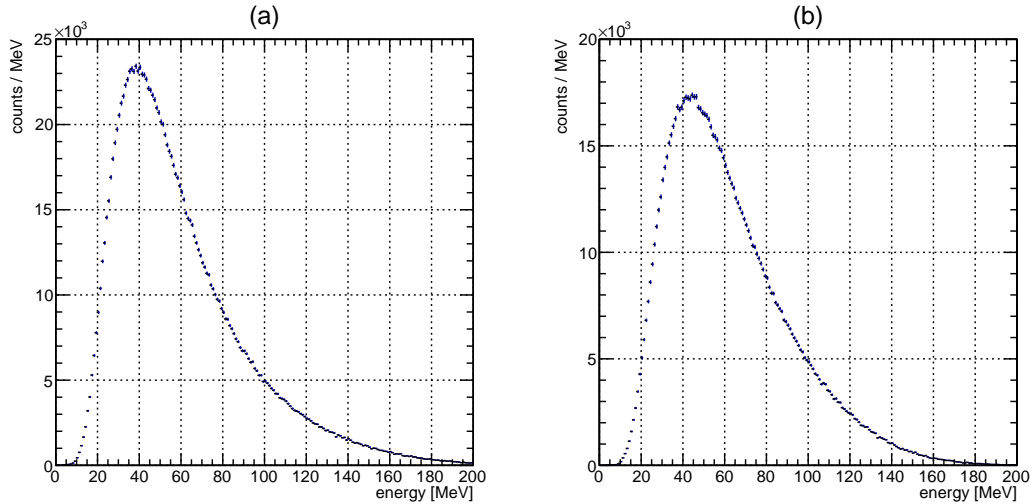


Fig. 7.19.: Measured energies, when the impact of the electron beam is shifted away from the crystal's center into another crystal: **(a)** shows the energy, when the beam is shifted 1 cm to the left and **(b)** when it is shifted 1 cm downwards. Comparison with Fig. 7.18 **(d)** shows the detector's sensitivity to impact position shifts of the beam.

The final resolution of the small crystal, when it is read out by two SiPMs, has been determined to be $(21.6 \pm 0.01)\%$ for 210 MeV electrons with a central impact. At this point we have to keep in mind that this number was determined by considering only the signals from the SiPMs mounted to the prototype crystal. If all the signals from all the crystals of the prototype detector had been analyzed, the overall resolution would have been better, since a bigger part of the shower would have been measured. In this analysis this was not possible, because an energy calibration for the surrounding crystals could not be done with the existing data.

The obtained resolution (21.6 %) slightly differs from the simulated result from section 7.2.3 (17.5 %). But remembering that many of the simulation parameters have been chosen by estimation with no detailed experimental data of the hardware, the result is quite satisfying. The measured resolution should also be handled with care, since an energy calibration with only two measured points and zero is not ideal. For an adjustment of the simulation parameters, more experimental data at several energies is needed.

7.2.5. Measurements at Different Rates

Beside the determination of the energy resolution, the DAQ was tested at different rates. Since we shared the beam time at MAMI with a group from Mainz, the beam time was used alternately. After our energy calibration runs, our detector was removed and replaced by the detector from the Mainz group. This had the advantage that we could analyze the data and find possible problems before the next runs. But that also meant that the energy calibration might not be valid anymore. It actually turned out that the energy calibration is not valid anymore at different rates anyway.

The rate of the incoming electrons can be changed by changing the current in the accelerator. This has to be done by consulting the accelerator operating staff. The plastic scintillator bars shown in Fig. 7.9 were used for the determination of the rate, for that purpose the detector has to be removed from its position, which has been done by using the remote-controllable xy table mentioned above.

Fig. 7.20 shows the resulting signals for SiPM1 at a rate of 8 kHz, 103 kHz, 1050 kHz and 2000 kHz. At higher rates the peaks become narrower and shift towards lower adc channels. A second smaller peak coming from pileup is visible at 1050 kHz and 2000 kHz rate. Investigations about the reason of this narrowing and the adc channel shift lead to the preamps, which are directly connected to the SiPMs: At its output it has a shaping capacity, which determines the output pulse length. For the beamtest it has been chosen in a way, that the sADC, which takes sampling points every 16 ns, can see a pulse, which is long enough (≥ 10 samples = 160 ns) for pulse recognition. Since this capacity needs a characteristic time to charge/discharge, signals come to close after each other at high rates, so that the capacity is not fully charged/discharged before the next signal arrives. In consequence the signal heights become smaller and the adc channel spectrum shifts towards smaller values at high rates. This problem can be diminished by using a smaller capacity, which may lead to pulse recognition problems of the sADC due to shorter pulse length, or by using a higher supply voltage for the preamp, which has been tested using a pulser (see Fig. 7.21). This introduces another problem: the supply voltage of the preamp also determines the amplification of the signal. If the preamp is constantly running at maximum supply voltage, the pulse heights at higher energies may exceed the operation range of the ADC chips on the sADC (see section 6.2). This could be handled by additional attenuators on the MPPC coincidence board. Additional rate insensitive shapers increasing the pulse length would also be useful.

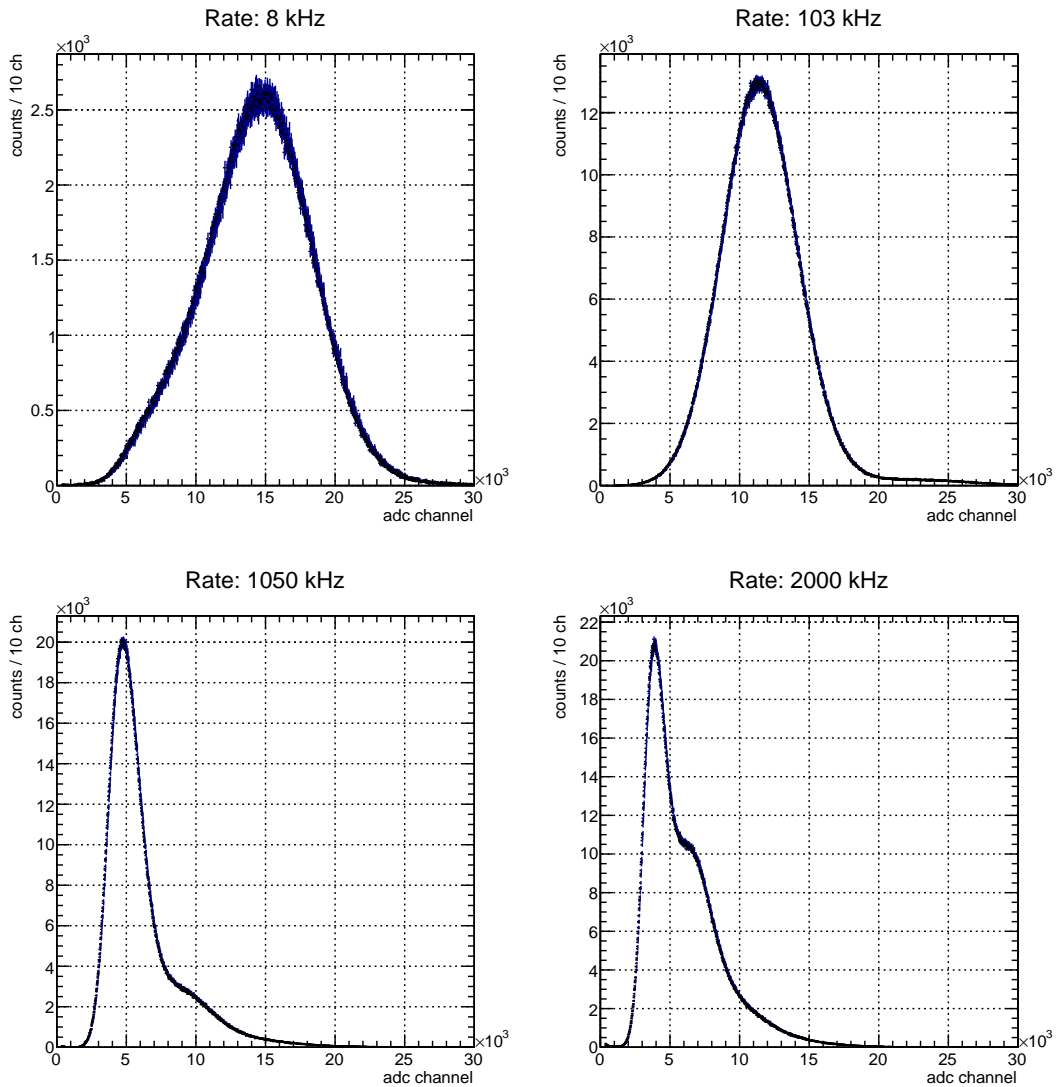


Fig. 7.20.: Signals from 210 MeV electrons obtained with SiPM1 measured at different rates: With increasing rate the peak becomes narrower and shifts towards smaller adc channels. Additionally, at rates above 103 kHz a second peak coming from pileup appears.

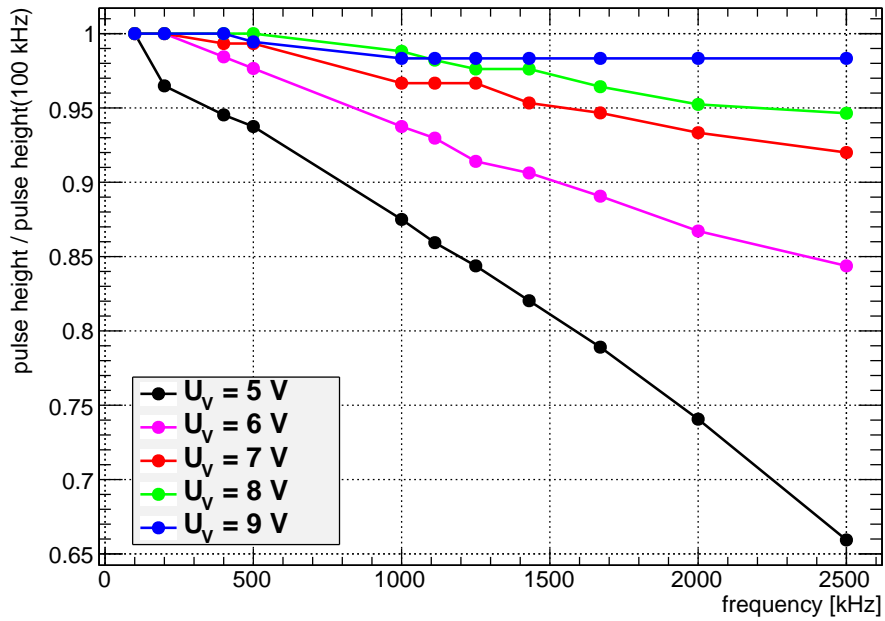


Fig. 7.21.: Relative pulse heights measured with different preamp supply voltages: The pulse height is more stable at higher rates when the supply voltage is higher.

7.3. Conclusion

The experiments explained in this chapter proved the functionality of both the detector and the DAQ: In all experiments the DAQ ran stable and the achieved results are in good agreement with what one would expect. Concerning the for our purpose important high rate stability of the detector signals, additional developments for the MPPC coincidence board are needed. Also, the firmware of the sADC could be further developed: Relating to [98], the ADC chips on the sADC can run at 125 MHz, which would double the number of sampling points per pulse. This would allow to use a smaller shaping capacity on the preamps which would further diminish the high rate problems mentioned above. The actual sADC firmware does not run stably with a 125 MHz sampling clock. Furthermore, feature extraction for the SiPM pulses and subevent-building (which is the same as the event building now being done on the CN) could be implemented on the sADC, which would be helpful for the cZDD DAQ (see section 4.3.3).

SUMMARY, DISCUSSION AND PERSPECTIVES

This thesis focuses on simulations and DAQ developments for a crystal zero degree detector for the measurement of photons from the initial state at BESIII. The cZDD needs a fast and powerful DAQ, which is capable of correlating events from the cZDD with events measured by the other detectors of BESIII in real time. This provides a unique and realistic high rate environment for tests of PANDA DAQ modules, which are being developed for similar purposes and foreseen to be used as parts of the cZDD's DAQ.

The angular distribution of ISR photons is very much peaked in the forward/backward region at around $\theta = 0^\circ$. Therefore, even a small calorimeter being placed in that region has an angular acceptance comparable to that of the whole BESIII detector [70]. Since the forward/backward region at BESIII is covered with beampipes, magnets and other supporting structures, the available space for the cZDD at BESIII is very small. This constrains the detector's dimensions and thus its capabilities.

In order to get an idea of the capabilities of the foreseen cZDD, a detailed Geant4-based simulation has been implemented in the BESIII Offline Software System. Because of lack of experimental data on specific properties of the detector crystals, the simulation has been done using properties given by educated guess. ISR events have been studied using the Phokhara event generator and the overall energy resolution of the cZDD has been estimated to be $\sigma/\mu = 0.06 \oplus 0.025/\sqrt{E[\text{GeV}]}$, which is comparable to that of the currently installed ZDD [70]. The cZDD's radiation hardness and the possibility to heal possible radiation damages during operation [73] makes it a powerful upgrade for the currently installed ZDD.

The influence of the reconstructed photon impact on the cZDD for the determination of \sqrt{s}_{ISR} has been studied. For this purpose a logarithmic energy weighted impact

position reconstruction algorithm has been used, which yields better results than an algorithm with linear energy weighting. The resolution of \sqrt{s}_{ISR} for central impacts (=radial distance of reconstructed photon impact to the detector's center ≤ 1.2 cm) is significantly better than 10 %. Using appropriate photon impact dependent correction factors, the correct \sqrt{s}_{ISR} can be estimated and used for e.g. R measurements. In the experiment, the determination of the appropriate correction factors is crucial since the energy of the ISR photon is not known. An iterative algorithm using data from the cZDD and the other BESIII detectors could be used for the estimation of the photon energies and could be working as follows: The asymmetry of the event topology in the BESIII detector reflects the Lorentz-boost of the center-of-mass frame, which is caused by the emission of the ISR photon. Together with the data on the total visible energy measured by the BESIII detector, a first approximation on the photon energy can be extracted. This can be compared to measurements from the cZDD and this first approximation can be adjusted accordingly. The new approximation can then again be compared to the data from all BESIII detectors and accordingly adjusted, et cetera. The use of artificial neural networks, which have all relevant detector data as an input, may help to determine the correct photon energy and to correctly extract \sqrt{s}_{ISR} .

The readout of the cZDD is based on two silicium photomultipliers, which detect the scintillation light of each crystal. After being preamplified the signals are prefiltered by a MPPC coincidence board, which has been developed in collaboration with the electronics workshop of II. Physikalisches Institut during this thesis. This board filters out thermally generated noise and passes the signals on to a programmable FPGA-based sampling Analog-Digital-Converter prototype developed for $\bar{\text{P}}\text{ANDA}$. The firmware of the sADC has been programmed in a way that it sends out the digitized waveform of each pulse to a Compute Node via an optical link. This optical link has a data transfer rate of 3.125 Gb/s and uses the AURORA protocol, which is based on 8B/10B encoding. The CN is FPGA-based and also currently developed for $\bar{\text{P}}\text{ANDA}$ and allows for complex logic operations on the incoming data. An event builder algorithm has been developed, which interprets the sADC data, is able to suppress background and to cluster signals based on adjustable criteria. After event building the data is buffered in the CN's RAM before it is forwarded via SiTCP to a PC for storage and data analysis.

In order to test the functionality of the DAQ chain, a prototype setup using the latter DAQ modules and a prototype PbWO_4 crystal similar to those foreseen for the final cZDD has been built.

For tests with radioactive sources the PbWO_4 needed to be exchanged by a LYSO crystal, which has similar properties as PbWO_4 , but a much larger scintillation light yield. In order to suppress signals from decays of the radioactive ^{176}Lu isotope (~ 2.5 % of naturally occurring Lu, $\tau_{1/2} = 3.8 \cdot 10^{10}$ years) from the crystal itself, a coincidence

setup with an additional BaF_2 crystal read out by a standard PMT, whose signal is additionally fed into the sADC, has been used. If a radioactive source decays via a cascade of coincident photons/particles, in some cases one photon/particle enters the LYSO crystal, whereas the other enters the BaF_2 crystal. The event builder has been programmed in a way that it only accepts events where coincident signals of LYSO and BaF_2 have been detected. Using a radioactive ^{22}Na source with a peak at 0.511 MeV and at 1.274 MeV in the resulting spectrum, an energy calibration of the setup has been performed. This calibration has then been used to measure the spectra of ^{60}Co . The spectrum of ^{176}Lu from the LYSO self-activity has also been measured, but without the additional BaF_2 coincidence condition. Both obtained energy spectra agree with what we would expect from the decay schemes, which demonstrates the functionality of the photodetectors, the DAQ chain and the event builder algorithm.

Using the original PbWO_4 crystal and the full prototype detector described in chapter 7 and the DAQ chain from chapter 6, a beamtest with 210 MeV electrons at the Mainz Microtron has been performed. Additional measurements of cosmic muons allowed for an energy calibration of the setup. The energy resolution of the prototype PbWO_4 crystal has been determined to be 21.6 ± 0.01 % for 210 MeV electrons. The results for a corresponding simulation of the detector yielded an energy resolution of 17.5 ± 0.7 %, which is satisfactory given the circumstances of the parameter settings in the simulation. In order to tune the parameters, additional experimental data on the properties of the crystals at different energies is needed. The generation of the SiPM output pulses also needs revision with more experimental data on the SiPM signals, when reading out the PbWO_4 crystals at different incident photon/electron energies. The influence of bias voltage changes on the height and form of the SiPM output signals also has to be studied and implemented into the simulation. Meanwhile, newer versions of the used SiPMs with improved properties are available from Hamamatsu [99], which should be used for a full detector assembly.

The prototype detector was also tested at different rates (8 kHz up to 2 MHz). This test revealed significant high-rate problems of the preamp, which preamplifies the signals of the SiPMs, before they are transferred to the MPPC coincidence board. This can be solved by increasing the supply voltage of the preamp and by diminishing the shaping capacity at its output. The more the shaping capacity is diminished, the shorter the resulting output pulse will be and digitization on the sADC will not work properly anymore, because the pulses have to be long enough for proper digitization. This can be solved by increasing the sADC's sampling frequency to 125 MHz, but this demands bigger changes in the sADC's firmware, which did not work properly at 125 MHz sampling frequency with the current firmware.

The capabilities of the cZDD have been investigated and developments for the cZDD DAQ using prototype DAQ modules being developed for \bar{P} ANDA have been done, but further work is necessary. The DAQ of the cZDD has to be joined with the existing BESIII DAQ and an event building algorithm combining data from cZDD and the rest of the BESIII detectors in real time has to be developed for proper event correlation, which is crucial for ISR studies with the cZDD. The development of the event correlation algorithm demands a deeper look at the BESIII DAQ and Trigger schemes. The most important questions to be answered are what information are needed for event correlation and what information can be delivered by the BESIII Trigger System. Hopefully, both answers have a large overlap. \bar{P} ANDA will benefit from the experience with such real time event correlation algorithms, which are needed on an even larger scale for a successful operation of the \bar{P} ANDA DAQ.

DEUTSCHE ZUSAMMENFASSUNG

Die vorliegende Arbeit befasst sich mit Simulationen für einen aus Bleiwolframat Kristallen aufgebauten Null-Grad-Detektor (cZDD) zur Messung von Photonen aus dem Anfangszustand (ISR) an BESIII. Außerdem werden Entwicklungen für ein entsprechendes Datenaufnahmesystem (DAQ) des Detektors dargestellt. Der cZDD braucht ein schnelles und leistungsfähiges Datenaufnahmesystem, welches in der Lage ist Daten aus dem cZDD mit Daten der übrigen BESIII-Detektoren in Echtzeit zu korrelieren. Die geplante DAQ basiert auf Prototypen von PANDA DAQ Modulen, die zu einem ähnlichen Zweck entwickelt werden. Das hier dargestellte Experiment bietet daher eine gute Möglichkeit Echtzeitdatenkorrelationen in einem realistischen Experiment unter hohen Raten zu testen.

Die Winkelverteilung von ISR Photonen besitzt ein ausgeprägtes Maximum im Bereich um $\theta = 0^\circ$. Aus diesem Grund hat sogar ein kleines Kalorimeter, welches in diesem Bereich platziert ist, eine Winkelakzeptanz, die vergleichbar mit der des gesamten BESIII-Detektors ist. Bei BESIII befinden sich im Bereich um $\theta = 0^\circ$ Strahlrohre, Magnete und weitere Elemente, die den Platz für den cZDD deutlich einschränken und daher auch seine Leistungsfähigkeit begrenzen.

Um die Leistungsfähigkeit des cZDD abschätzen zu können, wurde eine detaillierte Geant4-basierte Simulationssoftware für den Detektor entwickelt und in das BESIII Offline Software System (BOSS) implementiert. Da es keine experimentellen Daten für die Eigenschaften der vorgesehenen Detektorkristalle gibt, wurden die entsprechenden Simulationsparameter abgeschätzt. ISR Ereignisse wurden mithilfe des Phokhara Monte Carlo Generators simuliert und ausgewertet, dabei ergab sich eine zu erwartende Auflösung von $\sigma/\mu = 0.06 \oplus 0.025/\sqrt{E} [\text{GeV}]$. Dies ist vergleichbar mit der Auflösung eines aktuell an BESIII installierten ISR Detektors (ZDD). Aufgrund seiner Strahlungshärte und der Möglichkeit auftretende Strahlungsschäden bei laufendem Betrieb ausheilen zu können, stellt der cZDD ein leistungsfähiges Upgrade des ZDD dar.

Mithilfe der Simulation wurde auch der Einfluss des Photonen-Einstoßpunktes am cZDD auf die Bestimmung der verfügbaren Schwerpunktsenergie \sqrt{s}_{ISR} untersucht. Zur Bestimmung desselben wurde ein logarithmisch energiegewichteter Algorithmus verwendet, der bessere und realistischere Resultate als ein Algorithmus mit linear Energiegewichtung produziert. Es ergab sich, dass \sqrt{s}_{ISR} für zentrale Einstoßpunkte (= radialer Abstand von Photonen-Einstoßpunkt und Detektorzentrum ≤ 1.2 cm) mit einer Auflösung deutlich besser als 10% bestimmt werden kann. Werden entsprechende Photonenenergie- und Einstoßpunkt-abhängige Korrekturfaktoren für die im cZDD gemessenen Energiewerte verwendet, kann der korrekte Wert für \sqrt{s}_{ISR} ermittelt und z.B. für R -Wert Messungen verwendet werden. Im Experiment ist die Bestimmung der jeweiligen Korrekturfaktoren für jedes Ereignis entscheidend, da die Energie des ISR Photons nicht bekannt ist. Ein iterativer Algorithmus, der sowohl Daten der BESIII Detektoren als auch Daten des cZDD berücksichtigt und auswertet, könnte bei der Bestimmung der korrekten Photonenenergie und damit der richtigen Korrekturfaktoren zur Bestimmung von \sqrt{s}_{ISR} helfen. Künstliche neuronale Netze, die alle relevanten Detektorinformationen verarbeiten, könnten ebenfalls hilfreich sein.

Die Auslese des cZDD basiert auf zwei Siliziumphotomultipliern (SiPMs), die das Szintillationslicht eines jeden Kristalls detektieren. Nachdem die Signale vorverstärkt werden, werden sie weiter durch das MPPC Koinzidenz Board, welches im Laufe der Arbeit in Zusammenarbeit mit der elektronischen Werkstatt des II. Physikalischen Instituts entwickelt wurde, gefiltert. Dabei werden unkorrelierte Signale der SiPMs, verursacht durch thermisches Rauschen, herausgefiltert und nur koinzidente Signale weitergeleitet, bei denen beide SiPMs ein phasengleiches Signal liefern. Die Signale werden dann in einem FPGA-basierten, für $\bar{\text{P}}\text{ANDA}$ entwickelten 62.5 MHz sampling ADC (sADC) digitalisiert. Von dem sADC werden die digitalisierten Signale mit ihrer kompletten Pulsform über einen optischen Link mit einer Datenrate von 3.125 Gb/s an einen FPGA-basierten Compute Node (CN) übertragen. Dieser Compute Node erlaubt die Ausführung von komplexen Logikoperationen. In unserem Fall interpretiert der CN die Daten des sADCs, unterdrückt Untergrund und clustert zusammengehörige Signale zu einem Event zusammen (Event Builder). Die dabei zugrundeliegenden Parameter können je nach Anwendung angepasst werden. Nach dem Eventclustering werden die Events im RAM des CN gepuffert, bevor sie über Ethernet an einen PC zur Speicherung und weiteren Datenanalyse gesendet werden.

Um DAQ-Tests mit radioaktiven Quellen machen zu können, wurde der Bleiwolframat-Prototypkristall wegen mangelnder Lichtausbeute (15 - 19 Photonen pro MeV deponierter Energie), wie im Falle von radioaktiver Strahlung, ausgetauscht durch einen LYSO (Lutetium-Yttrium-oxyorthosilikat) Kristall mit ähnlichen Eigenschaften, aber deutlich besserer Lichtausbeute. Dieser Szintillator weist aber aufgrund des radioaktiven ^{176}Lu Isotops (2.5 % des natürlich vorkommenden Lu, $\tau_{1/2} = 3.8 \cdot 10^{10}$ Jahre) eine Eigenaktivität von einigen $k\text{Bq}$ aus. Um derartigen Untergrund zu verringern,

wurde ein Koinzidenzsetup mit einem weiteren BaF₂-Szintillator, der von einem Photomultiplier ausgelesen wird und dessen Signal ebenfalls in den sADC eingespeist wird, verwendet. Werden mit dem Aufbau nun radioaktive Isotope, die beim Zerfall eine Kaskade von koinzidenten Photonen/Teilchen emittieren, gemessen, passiert es manchmal, dass ein Photon/Teilchen im LYSO detektiert wird, und das andere im BaF₂. Der Event Builder ist nun derart programmiert, dass er nur Ereignisse akzeptiert, in denen sowohl Signale aus dem LYSO Kristall als auch Signale aus dem BaF₂ Kristall registriert werden. Mit diesem Aufbau wurden nun ²²Na und ⁶⁰Co Spektren vermessen. Das Spektrum von ²²Na Quelle mit Linien bei 0.511 MeV und 1.274 MeV wurde dann zur Energiekalibration verwendet. Mithilfe dieser Kalibration konnte dann das Energiespektrum von ⁶⁰Co ermittelt werden. Weiterhin wurde die Selbstaktivität des LYSO gemessen, allerdings ohne die zusätzliche BaF₂ Koinzidenzbedingung. Beide erhaltenen Energiespektren stimmen mit dem überein, was man aus den Zerfallsschemata von ⁶⁰Co und ¹⁷⁶Lu erwarten würde. Mit diesen Tests konnte die Funktionalität der DAQ und des Event Builders verifiziert werden.

Mit dem Prototyp-Detektor aus Kapitel 7 und der oben beschriebenen DAQ wurde ein Beamttest mit 210 MeV am Mainzer Mikrotron (MAMI) durchgeführt. Durch die zusätzliche Messung kosmischer Myonen konnte die Energieauflösung des PbWO₄ Prototypkristalls zu $21.6 \pm 0.01\%$ für 210 MeV bestimmt werden. Simulationen mit diesem Detektorsetup ergaben eine entsprechende Auflösung von $17.5 \pm 0.7\%$, was in Anbetracht der Tatsache, dass die Simulationsparameter abgeschätzt wurden, ein zufriedenstellendes Ergebnis ist. Um die Simulationsparameter zu verbessern, sind weitere Tests bei unterschiedlichen Elektronen-/Photonenenergien notwendig. Auch die Generierung der SiPM Signale in der Simulation bedürfen der Überarbeitung und dem Vergleich mit experimentell gewonnenen Daten. Der Einfluss der Bias-Spannung auf die resultierende Pulsform der SiPMs bei unterschiedlichen Elektronen-/Photonenenergien bedarf ebenfalls der genaueren Untersuchung und Implementierung in der Simulation. Mittlerweile gibt es eine neue verbesserte Version der verwendeten SiPMs. Für die Bestückung des vollen Detektors sollten jene verbesserten SiPMs verwendet werden.

Weiterhin wurde der Prototyp-Detektor bei unterschiedlichen Raten (8 kHz - 2 MHz) getestet. Dabei kam es bei hohen Raten zu signifikanten Problemen des Vorverstärkers, der die SiPMs mit Spannung versorgt und die Signale verstärkt, bevor sie dann weiter zu dem MPPC Koinzidenz Board geleitet werden. Die gemessenen Pulsamplituden nahmen mit zunehmender Rate stark ab. Neben einer Vergrößerung der Versorgungsspannung des Vorverstärkers bietet eine Verkleinerung der pulsförmigen Kapazität am Ausgang des Vorverstärkers eine Möglichkeit das Verhalten bei hohen Raten stabil zu halten. Eine Verkleinerung dieser Kapazität führt zu einer Verkürzung der Pulslänge, dies aber wiederum führt dann zu Problemen beim Digitalisieren der Signale mit dem sADC, der eine bestimmte Mindestpulslänge zur Detektion eines Pulses braucht.

Dieses Problem kann durch Vergrößerung der Samplingfrequenz auf 125 MHz gelöst werden, dies verlangt jedoch größere Änderungen in der Firmware des sADC, der mit der aktuellen Firmware bei 125 MHz nicht stabil läuft.

In dieser Arbeit wurden die Leistungsfähigkeit des cZDD untersucht und viel Entwicklungsarbeit für dessen DAQ geleistet, aber viele Schritte bis zum Einbau des Detektors an BESIII sind noch nötig. Die DAQ des cZDD muss mit der bestehenden BESIII DAQ verbunden werden. Die wichtigsten zu lösenden Fragen betreffen die Ereignis-Korrelation: Welche Informationen werden zur Ereignis-Korrelation benötigt und welche Information können tatsächlich vom BESIII Trigger System geliefert werden? Eine große Schnittmenge beider Antworten ist Voraussetzung für eine erfolgreiche Ereignis-Korrelation. \bar{P} ANDA wird aus den Erfahrungen mit solchen Echtzeit-Ereignis-Korrelations-Algorithmen an BESIII wertvolle Erfahrungen und Rückschlüsse für sein eigenes DAQ-System machen können, bevor \bar{P} ANDA seine Datenaufnahme beginnen wird.

APPENDIX - SIMULATION

A.1. Crystal Numbering Scheme

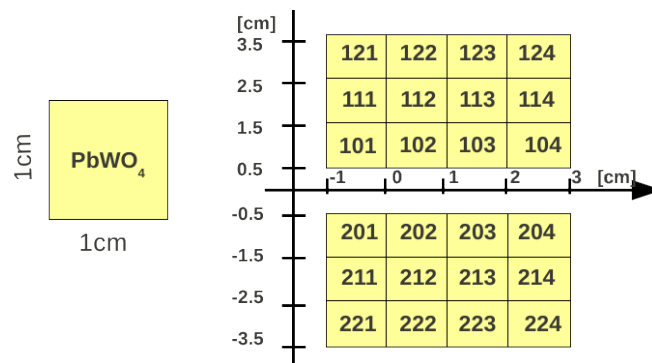


Fig. A.1.: This picture shows a schematic view of the cZDD design with the numbering scheme used in the simulation.

A.2. BesZddHits

Geant4 is a simulation toolkit developed by CERN, which provides information on particle interactions with matter. Geant4 is a step machine, which calculates all relevant interactions step by step. After each step, the user has access to all physically relevant information from `preStepPoint` and `PostStepPoint`. Which information is stored in a `BesZddHit` is decided by the user.

The following simulation information is stored in a cZDD-Hit (MC-Truth), see `BesZddHit.hh` and `BesZddHit.cc`:

- **prePos:** $G_4ThreeVector$: position of the traversing track before step; important for digitization (see section 5.2.2)

- **postPos:** *G4ThreeVector*: position of the traversing track after step; important for digitization (see section 5.2.2)
- **preCrystalNo:** *G4int*: crystal identification number corresponding to prePosition, negative numbers correspond to left (=east) detector part
- **postCrystalNo:** *G4int*: crystal identification number corresponding to postPosition, negative numbers correspond to left (=east) detector part
- **preTime:** *G4double*: time corresponding to prePos
- **postTime:** *G4double*: time corresponding to postPos
- **EDep:** *G4double*: energy deposited during step (between prePos and postPos)

A.3. BesZddDigis

In a *BesZddDigi* the following information is stored:

- **part ID:**
= 1 if east detector is hit, =2 if west detector is hit (viewpoint from BesIII control room onto the BesIII detector defines the south direction.)
- **detector ID:**
= 1 if upper crystals are hit, =2 if lower crystals are hits
- **crystal number:**
crystal identification number, see crystal numbering scheme above.
- **charge channel:**
charge channel number of ADC output, which corresponds to the energy deposit in the crystal
- **time channel:**
time channel number, which corresponds to the time difference to the start signal; not correctly implemented yet.

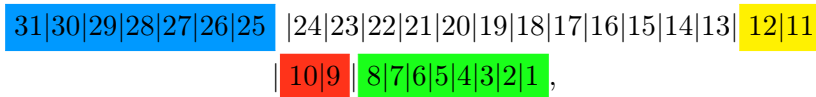
The simulated digi collections of the detectors are stored in a **.rtraw* root file. Since the reconstruction procedure for MC-simulation should be the same as for real data, where the detector output is a digitized electric signal, the information stored in the *BesZddDigis* need to be converted into binary code, which happens in the *DetectorDescription/Identifier* module of BOSS.

A.4. cZDD Identifier

The charge channel and time channel information of the *BesZddDigi* is just one number, which can easily be converted into a binary code. The information, which detector element had this particular time- and charge-channel, is not a single number and needs to be converted into a binary code.

In a *BesZddDigi*, 3 numbers for the identification of the detector element are stored: **partID** (1-2), **detectorID** (1-2) and **crystalNo** (101 - 224). In order to minimize the necessary disk space, all three numbers are encoded into one unsigned integer variable called identifier, where certain bits present the binary code of the identification numbers of the detector elements.

The bitcode of a 31-bit unsigned integer variable is



bits **25-31** are reserved for the detector identifier - which detector of BESIII does this identifier belong to, see Tab. A.1. Although 7 bits (25-31) are reserved, only 3 bits (29 - 31) are in use at the moment. Bits **11-12** are used to store part ID information (1,2), bits **9-10** are used to store detector ID information (1,2) and bits **1-8** are used to store crystal number information (101 - 224). At the moment bits 13-24 are not in use.

ID code	module
0 0 1	MDC ID
0 1 0	TOF ID
0 1 1	EMC ID
1 0 0	MUC ID
1 0 1	HLT ID
1 1 0	cZDD ID
1 1 1	MRPC ID

Tab. A.1.: Identification numbers of the BESIII detectors, which correspond to bits 29-31 in the identifier unsigned integer.

The identifier module works in both ways: it can convert given detector information (partID, detectorID and crystalNo) into unsigned integers and vice versa. The internal identifier functions work with bitshift operators \ll , \gg and bitwise *OR* ($|$) and *AND* ($\&$) statements.

A.5. Fits and Parameters

A.5.1. Single Pixel Signals

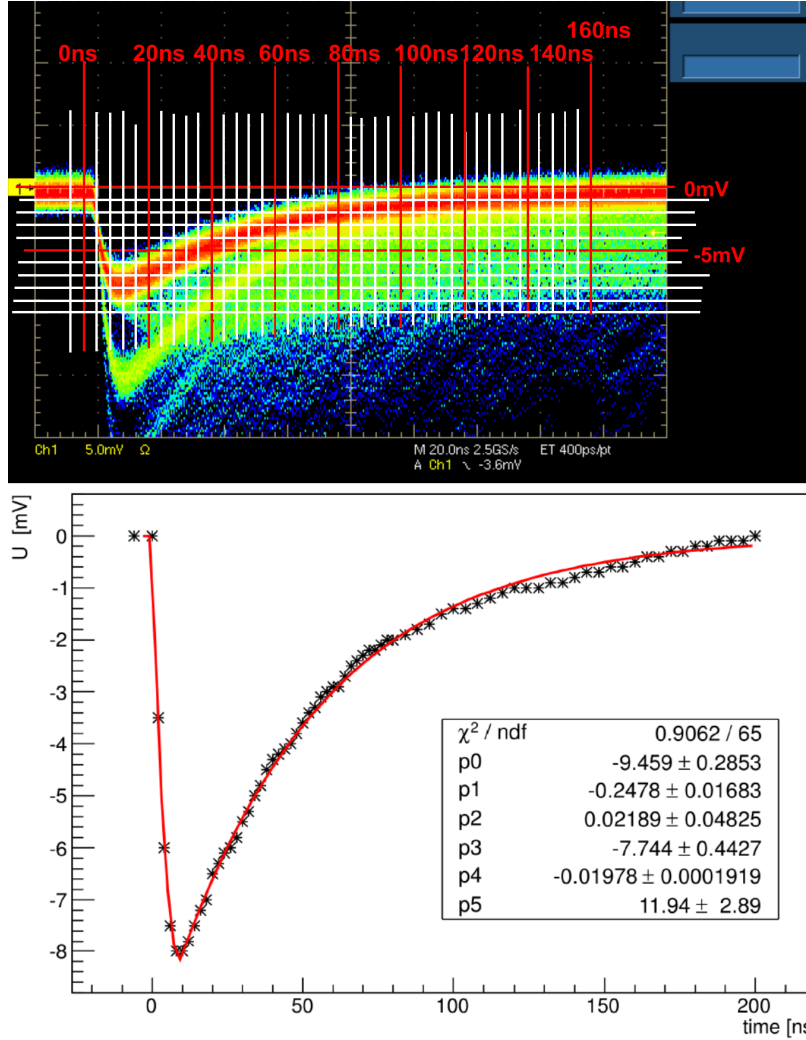


Fig. A.2.: Upper plot: Screenshot of a single pixel signal of the used SiPM. The C5 capacity of the preamp has been modified to 23 nF, the bias voltage was set to 72.5 V, the supply voltage was set to 5V. The lower plot shows the corresponding data points fitted with exponential functions (see Eq. (A.5.1)).

$$f(x) = \begin{cases} 0 & \text{if } x < 0 \\ p_0 \cdot \exp\{p_1 \cdot (x - p_2)\} & \text{if } x < 9 \\ p_3 \cdot \exp\{p_4 \cdot (x - p_5)\} & \text{if } x \geq 9 \text{ and } x < 250 \\ 0 & \text{else} \end{cases} \quad (\text{A.5.1})$$

A.5.2. Correlation of Charge Channel and Energy Deposition

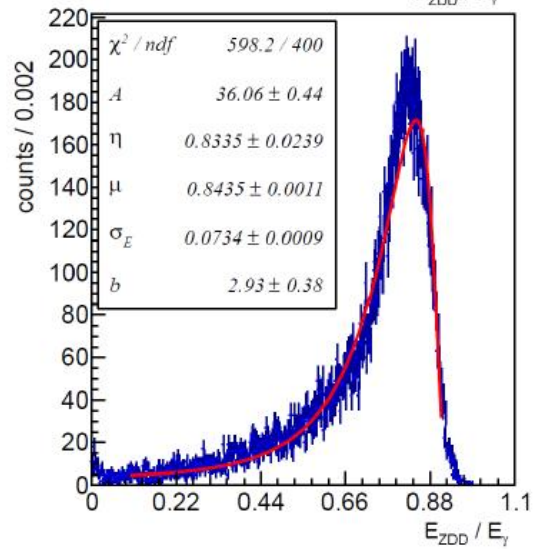
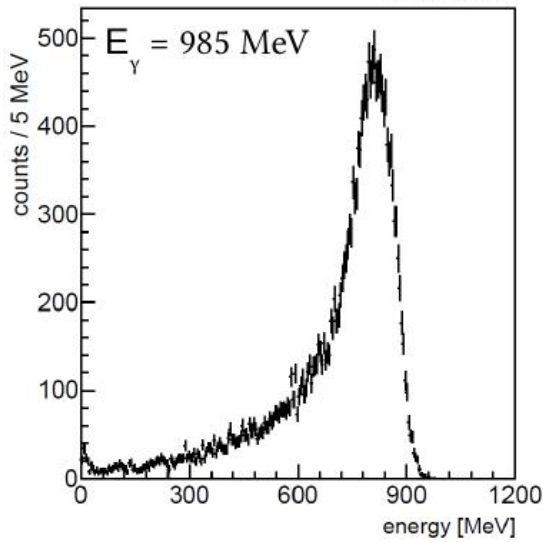
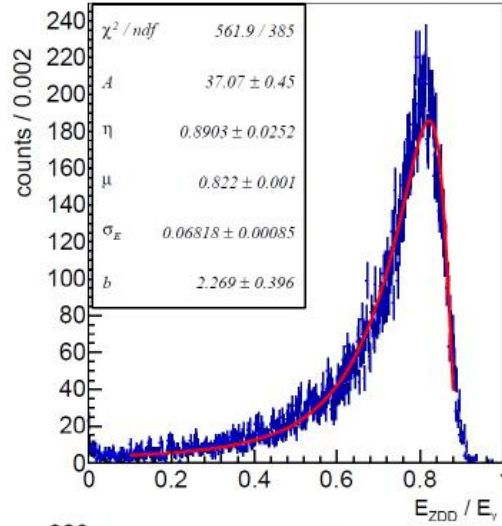
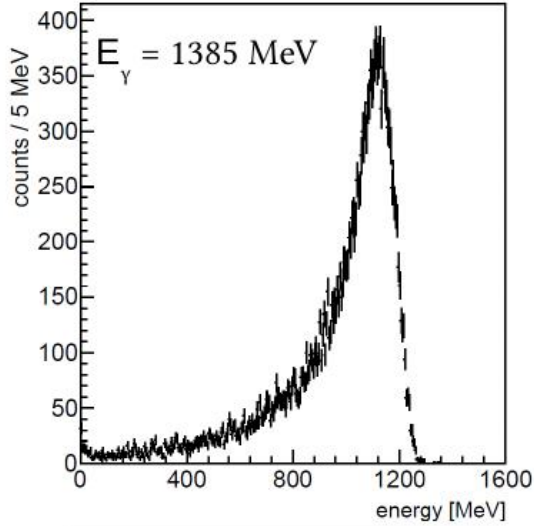
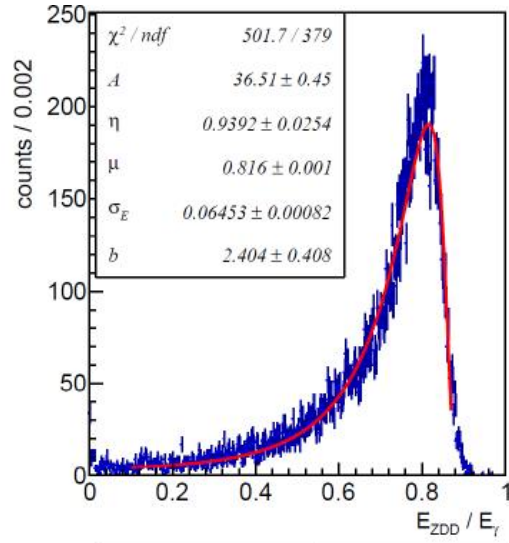
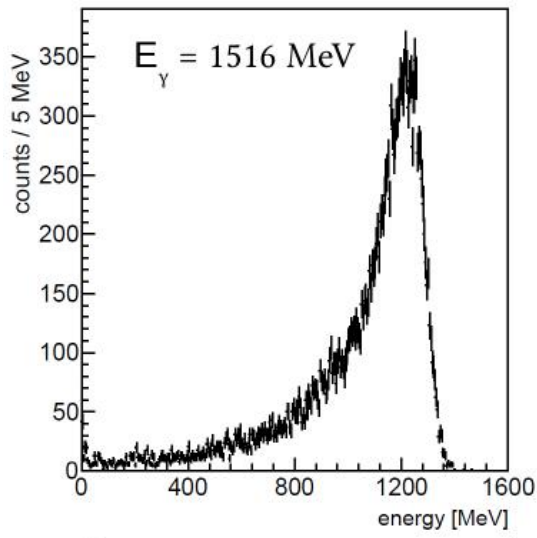
Correlation of charge channel and energy deposition, after Fig. 5.7.

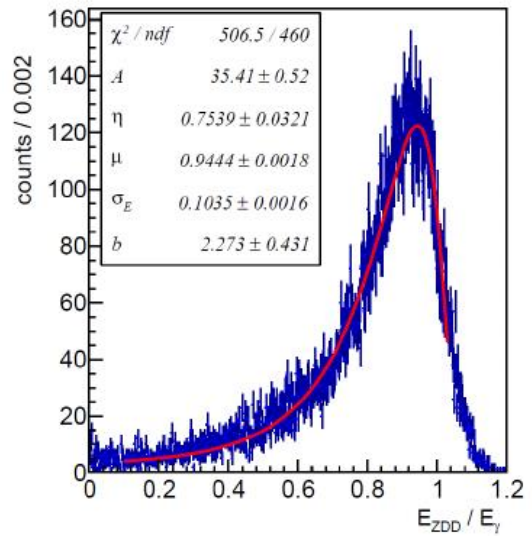
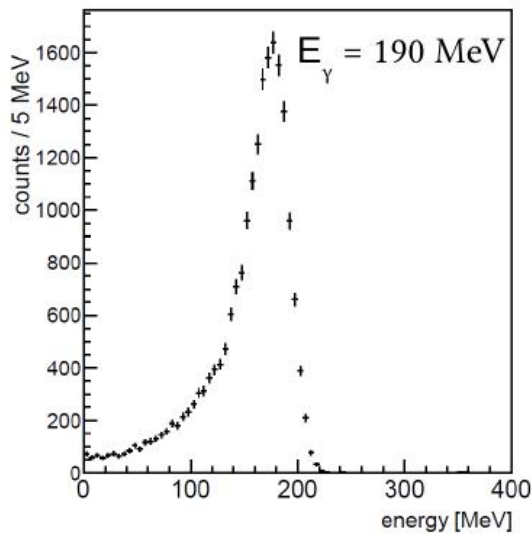
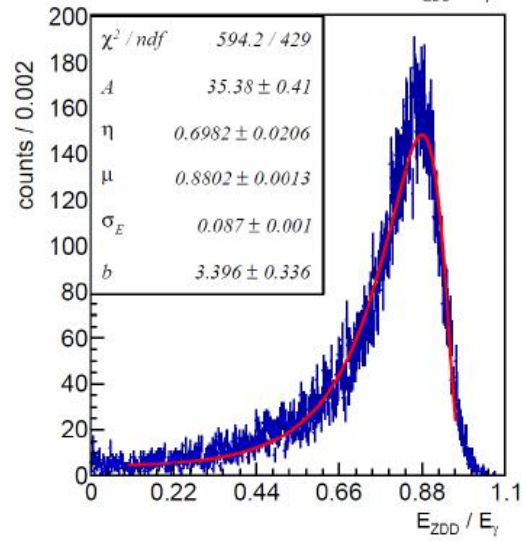
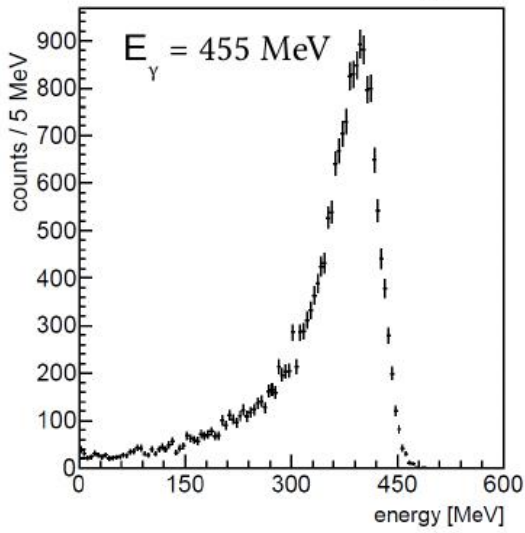
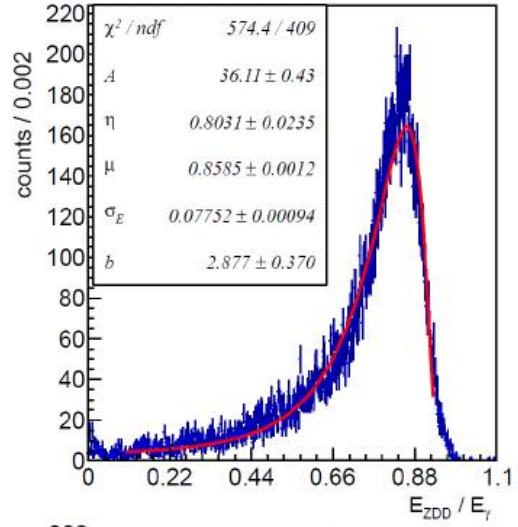
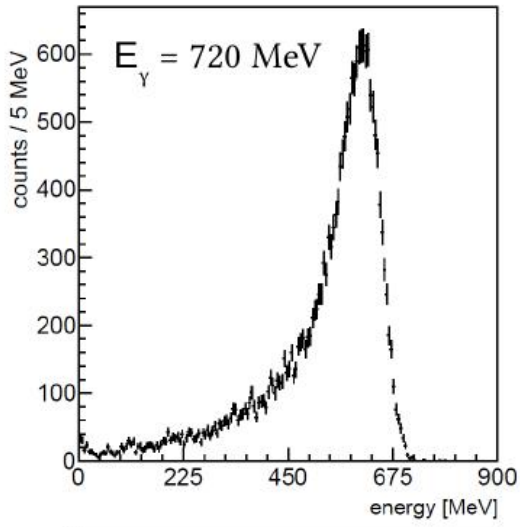
$$f(x) = p_0 + p_1 \cdot x + p_2 \cdot x^2 + p_3 \cdot x^3 + p_4 \cdot x^4 + p_5 \cdot x^5 \quad (\text{A.5.2})$$

Parameter	value
p_0	$3.89193 \cdot 10^{-1}$
p_1	$6.04002 \cdot 10^{-2}$
p_2	$-3.36707 \cdot 10^{-6}$
p_3	$5.30877 \cdot 10^{-10}$
p_4	$-3.26692 \cdot 10^{-14}$
p_5	$7.02335 \cdot 10^{-19}$

Tab. A.2.: Fit parameters of the charge channel \mapsto energy deposition correlation.

A.5.3. cZDD Resolution Fits





A.6. \sqrt{s}_{ISR} Determination

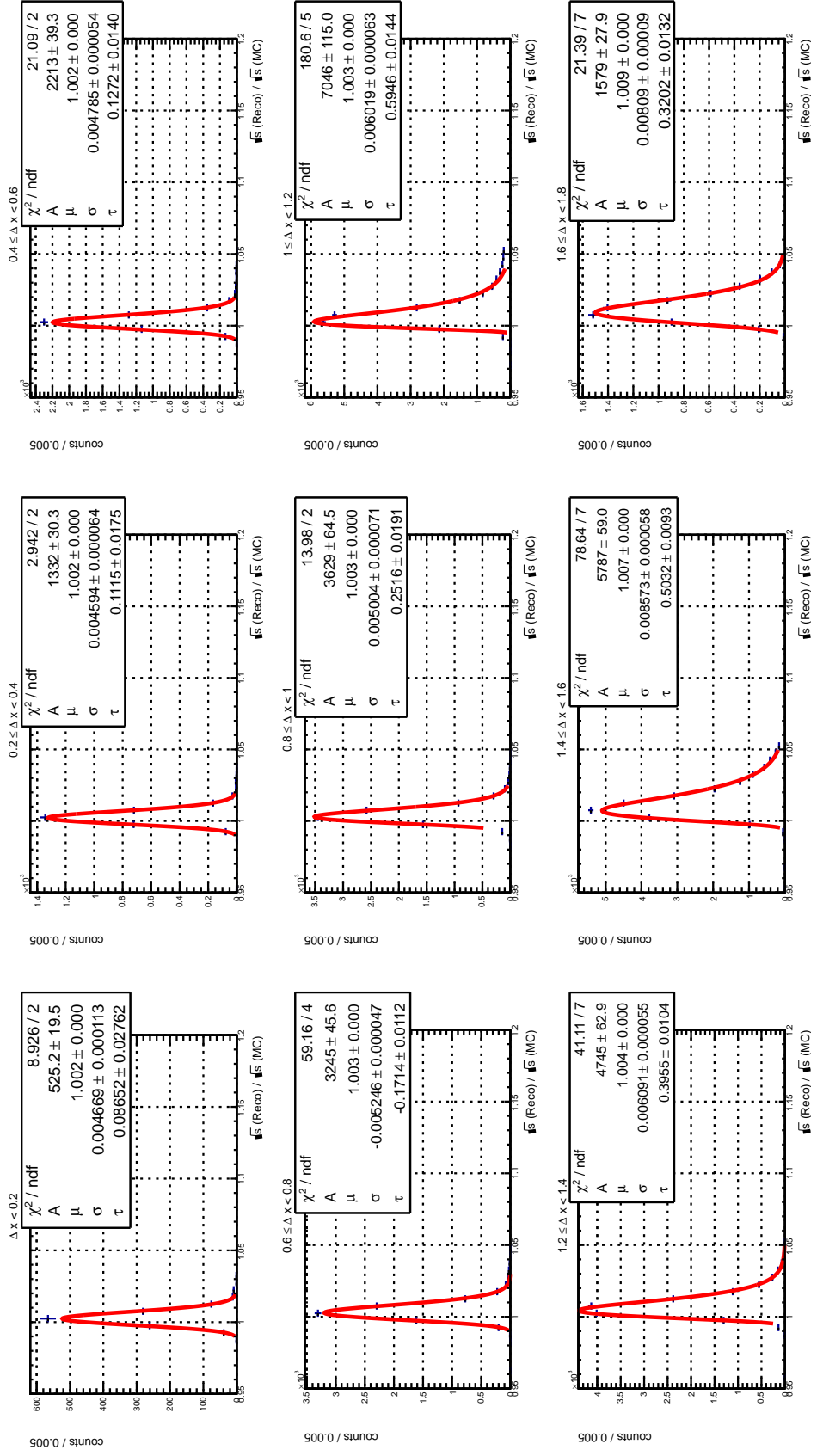


Fig. A.3.: Fits for 200 MeV ISR photons in dependence of the reconstructed photon impact on the cZDD.

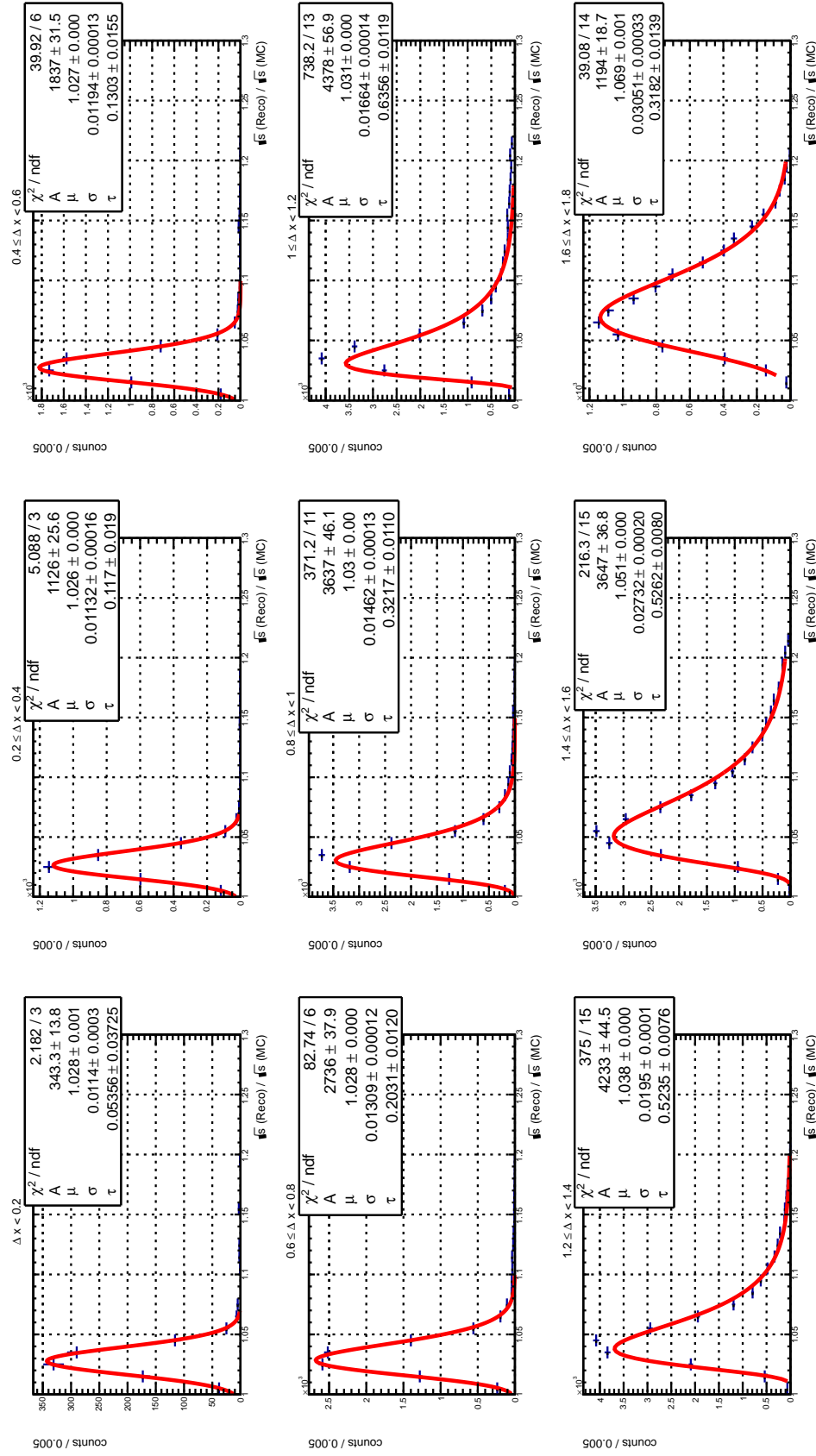


Fig. A.4.: Fits for 600 MeV ISR photons in dependence of the reconstructed photon impact on the cZDD.

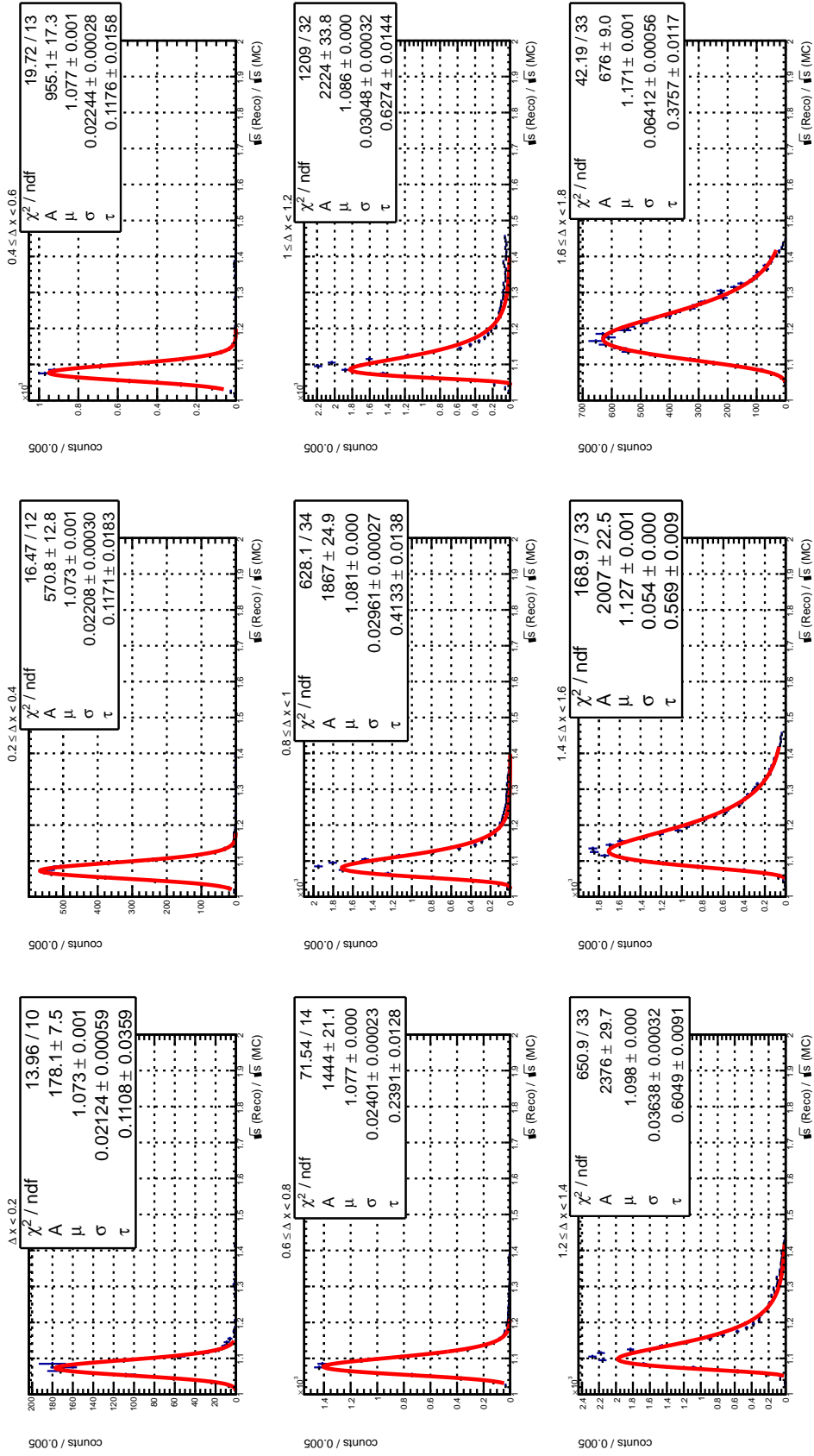


Fig. A.5.: Fits for 1000 MeV ISR photons in dependence of the reconstructed photon impact on the cZDD.

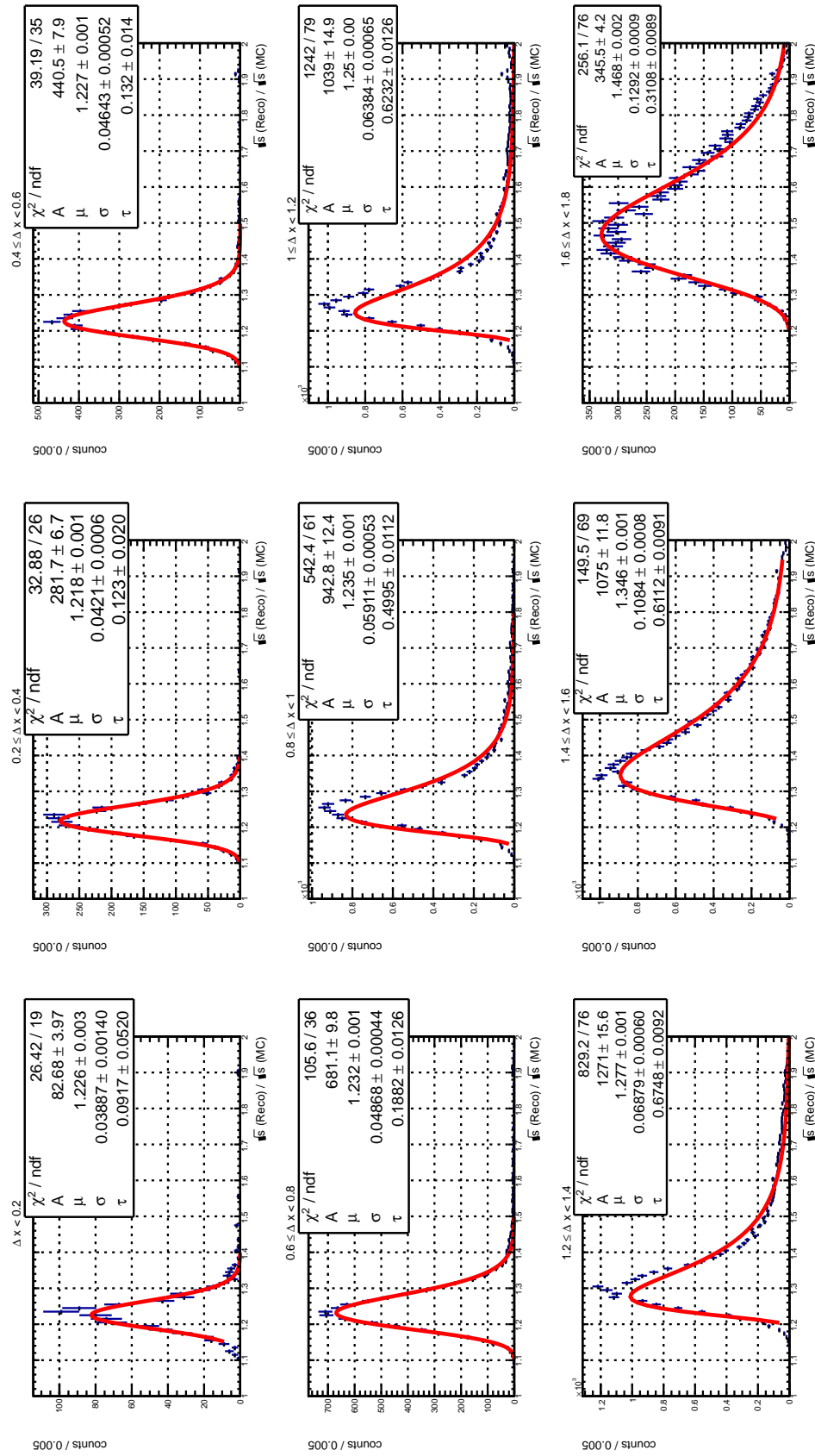


Fig. A.6.: Fits for 1400 MeV ISR photons in dependence of the reconstructed photon impact on the cZDD.

APPENDIX - DAQ

B.1. Data Format

Before the data is transformed to 32bit for transmission via SiTCP, the data consists of 36bit words, with the first four bits (36..32) being the marker for the wave part, which is contained in the word (Tab. B.1).

wave part	bits (36...32)
timestamp	0000
eventnumber	0001
adc channel	0010
data samples	0011
last two adc samples	0100
last adc sample + 0	0101
error	1111

Tab. B.1.: Bits 36 - 32 of the wave encoding used for data processing on the CN.

The 32-bit data sent from Compute Node to PC is coded in the following data format:

word	bits	content
1	31...0	time stamp of maximum value in waveform
2	31...24 23...0	0x0 event number
3	31...24 23...16 15...0	statusbyte (bit6 = overflow) 0x0 adc number (channel identification)
4	31...16 15...0	'0' & adc sample 1 '0' & adc sample 2
5	31...16 15...0	'0' & adc sample 3 '0' & adc sample 4
⋮	⋮	⋮
N	31...16 15...0	'0' & adc sample n-1 '1' & adc sample n
N	31...16 15...0	'1' & adc sample n '0' & 0x0
ERROR	31...0	0x80008000

Tab. B.2.: Data format used, where the whole waveform is encoded. This encoding corresponds to a waveform consisting of n adc samples transmitted via N 32-bit words. The number of adc samples can be even or odd. In order to distinguish between those cases, the last word's encoding is different. The maximum number of adc samples is 255.

APPENDIX - EXPERIMENTS

C.1. Radioactive Sources

C.1.1. Fit Functions and Parameters

^{22}Na energy calibration fits

Fit functions used:

0.511 MeV Peak: (gaussian)

$$f(x) = A_1 \cdot \exp \left\{ -\frac{1}{2} \left(\frac{x - \mu_1}{\sigma_1} \right)^2 \right\} \quad (\text{C.1.1})$$

1.274 MeV Peak: (gaussian + exponential background)

$$f(x) = A_2 \cdot \exp \left\{ -\frac{1}{2} \left(\frac{x - \mu_2}{\sigma_2} \right)^2 \right\} + B \cdot \exp \{C + D \cdot x\} \quad (\text{C.1.2})$$

Parameter	adc channel spectrum (SiPM1)	adc channel spectrum (SiPM2)	two channel spectrum (SiPM1 + SiPM2)
A_1	$3.196 \cdot 10^5$	$2.657 \cdot 10^5$	$1.443 \cdot 10^4$
μ_1	$9.412 \cdot 10^3$	$1.086 \cdot 10^4$	1.041
σ_1	$3.302 \cdot 10^3$	$4.017 \cdot 10^3$	$1.664 \cdot 10^{-1}$
A_2	$1.715 \cdot 10^4$	$1.402 \cdot 10^4$	$8.032 \cdot 10^2$
μ_2	$2.518 \cdot 10^4$	$2.985 \cdot 10^4$	2.562
σ_2	$4.275 \cdot 10^3$	$5.128 \cdot 10^3$	$2.129 \cdot 10^{-1}$
B	$5.002 \cdot 10^{-1}$	$4.601 \cdot 10^{-1}$	$3.143 \cdot 10^{-3}$
C	$1.210 \cdot 10^1$	$1.200 \cdot 10^1$	$1.409 \cdot 10^1$
D	$-5.637 \cdot 10^{-5}$	$-4.732 \cdot 10^{-5}$	$-6.712 \cdot 10^{-1}$

Tab. C.1.: Fit parameters for the ^{22}Na energy calibration

Parameter	single channel energy spectrum (SiPM1)	two channel energy spectrum
A_1	$1.168 \cdot 10^4$	$1.443 \cdot 10^4$
μ_1	$5.060 \cdot 10^{-1}$	$5.115 \cdot 10^{-1}$
σ_1	$1.139 \cdot 10^{-1}$	$8.222 \cdot 10^{-2}$
σ_1/μ_1	22.5 %	16.1 %
A_2	$5.869 \cdot 10^2$	$7.958 \cdot 10^2$
μ_2	1.269	1.275
σ_2	$1.460 \cdot 10^{-1}$	$1.055 \cdot 10^{-1}$
B	$4.184 \cdot 10^{-3}$	$4.213 \cdot 10^{-2}$
C	$1.363 \cdot 10^1$	$1.150 \cdot 10^1$
D	-1.207	-1.352
σ_2/μ_2	11.5 %	8.3 %

Tab. C.2.: Fit parameters obtained for the ^{22}Na energy fits.

^{60}Co Fit Functions and Parameters

Fit function used:

1.173 MeV / 1.333 MeV Peak: (gaussian + exp. background)

$$f(x) = A \cdot \exp \left\{ -\frac{1}{2} \left(\frac{x - \mu}{\sigma} \right)^2 \right\} + B \cdot \exp \{ C + D \cdot x \} \quad (\text{C.1.3})$$

Parameter	single channel energy spectrum (SiPM1)	two channel energy spectrum
A	$1.301 \cdot 10^3$	$1.413 \cdot 10^3$
μ	1.255	1.297
σ	$2.101 \cdot 10^{-1}$	$1.651 \cdot 10^{-1}$
B	$1.293 \cdot 10^{-1}$	$2.906 \cdot 10^{-1}$
C	$1.162 \cdot 10^1$	$1.172 \cdot 10^1$
D	-3.232	-3.736
σ/μ	16.7 %	12.7 %

Tab. C.3.: Fit parameters obtained for the ^{60}Co energy fits.

^{176}Lu Fit Functions and Parameters

Fit function used:

0.088 MeV + 0.202 MeV + 0.307 MeV + E(e⁻) peak: (gaussian)

$$f(x) = A \cdot \exp \left\{ -\frac{1}{2} \left(\frac{x - \mu}{\sigma} \right)^2 \right\} \quad (\text{C.1.4})$$

Parameter	single channel energy spectrum (SiPM1)	two channel energy spectrum
A	$4.693 \cdot 10^4$	$5.045 \cdot 10^4$
μ	$9.329 \cdot 10^{-1}$	$9.358 \cdot 10^{-1}$
σ	$2.842 \cdot 10^{-1}$	$2.465 \cdot 10^{-1}$
σ/μ	30.5 %	26.3 %

Tab. C.4.: Fit parameters obtained for the ^{176}Lu energy fits coming from the LYSO self-activity.

C.2. Beamtest**C.2.1. Fit Parameters****MC Truth**

Parameter	cosmic muons	210 MeV electrons
A	$1.915 \cdot 10^4$	$1.050 \cdot 10^4$
μ	$1.550 \cdot 10^1$	$1.524 \cdot 10^2$
σ	1.616	$1.948 \cdot 10^1$
τ	$7.892 \cdot 10^{-1}$	$-3.631 \cdot 10^{-1}$
σ/μ	10.4 %	12.8 %

Tab. C.5.: Fit parameters obtained for the MC energy deposition fits from the Geant4 simulation (Fig. 7.11).

Digitized ADC Channel Spectrum From Simulation

Parameter	210 MeV electrons
A	$1.1011 \cdot 10^4$
μ	$4.1288 \cdot 10^3$
σ	$7.2429 \cdot 10^2$
τ	$-2.1695 \cdot 10^{-1}$
σ/μ	$(17.5 \pm 0.7) \%$

Tab. C.6.: Fit parameters obtained for the simulated adc channel spectrum (Fig. 7.12).

Cosmic Muons

Parameter	SiPM1	SiPM2
A	$5.331 \cdot 10^1$	$6.871 \cdot 10^1$
μ	$2.792 \cdot 10^3$	$2.144 \cdot 10^3$
σ	$1.077 \cdot 10^3$	$7.793 \cdot 10^2$

Tab. C.7.: Fit parameters obtained for the adc channel spectrum of the cosmic muon measurement at MAMI (Fig. 7.13).

Parameter	SiPM1	SiPM2	SiPM1 + SiPM2
A	$4.160 \cdot 10^1$	$4.789 \cdot 10^1$	$5.139 \cdot 10^1$
μ	$1.865 \cdot 10^1$	$1.752 \cdot 10^1$	$3.922 \cdot 10^1$
σ	9.428	7.273	$1.397 \cdot 10^1$
σ/μ	44.8 %	36.6 %	–

Tab. C.8.: Fit parameters obtained for the energy spectrum of the cosmic muon measurement at MAMI. The SiPM1 + SiPM2 column presents the fit results of the sum spectrum, which is scaled in arbitrary units and used for the final energy calibration (Fig. 7.17).

210 MeV Electrons

Parameter	SiPM1	SiPM2
A	$2.109 \cdot 10^4$	$2.388 \cdot 10^4$
μ	$1.821 \cdot 10^4$	$1.572 \cdot 10^4$
σ	$4.308 \cdot 10^3$	$3.805 \cdot 10^3$
τ	$-8.862 \cdot 10^{-3}$	$-4.892 \cdot 10^{-3}$

Tab. C.9.: Fit parameters obtained for the adc channel spectrum of the 210 MeV electron measurements at MAMI (Fig. 7.14).

Parameter	SiPM1	SiPM2	SiPM1 + SiPM2
A	$1.295 \cdot 10^4$	$1.257 \cdot 10^4$	$1.447 \cdot 10^4$
μ	$1.446 \cdot 10^2$	$1.464 \cdot 10^2$	$2.966 \cdot 10^2$
σ	$3.508 \cdot 10^1$	$3.609 \cdot 10^1$	$6.278 \cdot 10^1$
τ	$-1.161 \cdot 10^{-2}$	$-2.118 \cdot 10^{-3}$	$-6.683 \cdot 10^{-2}$
σ/μ	24.3 %	24.7 %	–

Tab. C.10.: Fit parameters obtained for the energy spectrum of the 210 MeV electrons measurements at MAMI. The SiPM1 + SiPM2 column presents the fit results of the sum spectrum, which is scaled in arbitrary units and used for the final energy calibration (Fig. 7.18).

BIBLIOGRAPHY

- [1] G. Aad et al. (ATLAS Collaboration), Phys.Lett. **B716**, 1 (2012), 1207.7214.
- [2] S. Chatrchyan et al. (CMS Collaboration), Phys.Lett. **B716**, 30 (2012), 1207.7235.
- [3] Cern Press Office, *New results indicate that particle discovered at CERN is a Higgs boson* (4th of March 2013), URL <http://press.web.cern.ch/press-releases/2013/03/new-results-indicate-particle-discovered-cern-higgs-boson>.
- [4] URL <https://news.slac.stanford.edu/sites/default/files/images/image/120704115008-large.jpg>.
- [5] P. Higgs, Physics Letters **12**, 132 (1964), ISSN 0031-9163.
- [6] P. W. Higgs, Phys. Rev. Lett. **13**, 508 (1964).
- [7] F. Englert and R. Brout, Phys. Rev. Lett. **13**, 321 (1964).
- [8] M. Shifman, Int.J.Mod.Phys. **A25**, 4015 (2010), 1007.0531.
- [9] S.-K. Choi, S. L. Olsen, K. Abe, T. Abe, I. Adachi, B. S. Ahn, H. Aihara, K. Akai, M. Akatsu, M. Akemoto, et al. (Belle Collaboration), Phys. Rev. Lett. **91**, 262001 (2003).
- [10] R. Aaij, C. Abellan Beteta, B. Adeva, M. Adinolfi, C. Adrover, A. Affolder, Z. Ajaltouni, J. Albrecht, F. Alessio, M. Alexander, et al. (LHCb Collaboration), Phys. Rev. Lett. **110**, 222001 (2013).
- [11] M. Lutz et al. (PANDA Collaboration), *Physics Performance Report for PANDA: Strong Interaction Studies with Antiprotons* (2009), 0903.3905.

- [12] W. Erni et al. (PANDA Collaboration), *Technical Design Report for the PANDA Solenoid and Dipole Spectrometer Magnets* (2009), 0907.0169.
- [13] W. Erni et al. (PANDA Collaboration), *Technical Design Report for PANDA Electromagnetic Calorimeter (EMC)* (2008), 0810.1216.
- [14] D. Bettoni, *Journal Of Physics: Conference Series* **9**, 309 (2005).
- [15] M. Kotulla et al. (PANDA Collaboration), *Strong interaction studies with antiprotons. Letter of intent for PANDA (Antiproton Annihilations at Darmstadt)* (2004).
- [16] W. Erni et al. (PANDA Collaboration), *Technical Design Report for the: PANDA Straw Tube Tracker* (2012).
- [17] K. Korcyl, I. Konorov, W. Kühn, and L. Schmitt, *Journal of Physics: Conference Series* **396**, 012027 (2012), URL <http://stacks.iop.org/1742-6596/396/i=1/a=012027>.
- [18] M. Ye and Z. Zheng, *Int. J. Mod. Phys.* **A02**, 1707 (1987).
- [19] M. e. a. Ablikim, *Nuclear Instruments and Methods in Physics Research, Section A: Accelerators, Spectrometers, Detectors and Associated Equipment* **614**, 345 (2010).
- [20] BESIII website, *BESIII Datasets* (August 2014), URL <http://bes3.ihep.ac.cn/datasets/datasets.htm>.
- [21] M. Ablikim et al. (BESIII Collaboration), *Nucl.Instrum.Meth.* **A614**, 345 (2010), 0911.4960.
- [22] M. G. Ullrich, *Measurement of $\sigma(\psi(3770) \rightarrow p\bar{p}\pi^0)$ and Determination of $\sigma(p\bar{p} \rightarrow \psi(3770)\pi^0)$ for the $\bar{P}ANDA$ Experiment* (Ph.D. Thesis, II. Physikalisches Institut, JLU Gießen, 2013).
- [23] C. Zhao, S.-S. Sun, C. Li, X.-J. Zhang, K.-L. He, et al., *Chin.Phys.* **C35**, 72 (2011).
- [24] D. Asner, T. Barnes, J. Bian, I. Bigi, N. Brambilla, et al., *Int.J.Mod.Phys.* **A24**, S1 (2009), 0809.1869.
- [25] J. Messchendorp (PANDA Collaboration), *eConf* **C070910**, 123 (2007), 0711.1598.
- [26] E. Eichten, K. Gottfried, T. Kinoshita, K. D. Lane, and T. M. Yan, *Phys. Rev. D* **17**, 3090 (1978).

- [27] J. Eiglsperger, *Quarkonium Spectroscopy: Beyond One-Gluon Exchange* (2007), 0707.1269.
- [28] R. Partridge, C. Peck, F. Porter, W. Kollmann, M. Richardson, K. Strauch, K. Wacker, D. Aschman, T. Burnett, M. Cavalli-Sforza, et al., *Phys. Rev. Lett.* **45**, 1150 (1980).
- [29] T. M. Himel, G. H. Trilling, G. S. Abrams, M. S. Alam, C. A. Blocker, A. P. Blondel, A. M. Boyarski, M. Breidenbach, D. L. Burke, W. C. Carithers, et al., *Phys. Rev. Lett.* **45**, 1146 (1980).
- [30] R. M. Baltrusaitis, D. Coffman, J. Hauser, D. G. Hitlin, J. D. Richman, J. J. Russell, and R. H. Schindler, *Phys. Rev. D* **33**, 629 (1986).
- [31] D. Bisello, G. Busetto, A. Castro, S. Limentani, M. Nigro, M. Penzo, L. Pescara, M. Posocco, P. Sartori, L. Stanco, et al., *Physics Letters B* **179**, 289 (1986), ISSN 0370-2693.
- [32] J. Z. Bai, Y. Ban, J. G. Bian, I. Blum, A. D. Chen, G. P. Chen, H. F. Chen, H. S. Chen, J. Chen, J. C. Chen, et al. ((BES Collaboration)), *Phys. Rev. D* **62**, 072001 (2000).
- [33] M. Ablikim, M. N. Achasov, X. C. Ai, O. Albayrak, D. J. Ambrose, F. F. An, Q. An, J. Z. Bai, R. Baldini Ferroli, Y. Ban, et al. (BESIII Collaboration), *Phys. Rev. Lett.* **110**, 252001 (2013).
- [34] M. Ablikim et al. (BESIII Collaboration), *Observation of a charged charmonium-like structure $Z_c(4020)$ and search for the $Z_c(3900)$ in e^+e^- to $\pi^+\pi^-h_c$* (2013), 1309.1896.
- [35] R. Mizuk et al. (Belle Collaboration), *Phys.Rev.* **D78**, 072004 (2008), 0806.4098.
- [36] C. P. Shen, C. Z. Yuan, H. Aihara, K. Arinstein, T. Aushev, A. M. Bakich, V. Balagura, E. Barberio, A. Bay, K. Belous, et al. (The Belle Collaboration), *Phys. Rev. Lett.* **104**, 112004 (2010).
- [37] B. Aubert, R. Barate, M. Bona, D. Boutigny, F. Couderc, Y. Karyotakis, J. P. Lees, V. Poireau, V. Tisserand, A. Zghiche, et al. (BABAR Collaboration), *Phys. Rev. Lett.* **98**, 212001 (2007).
- [38] R. Mizuk et al. (BELLE Collaboration), *Phys.Rev.* **D80**, 031104 (2009), 0905.2869.
- [39] M. A. et al, *Chinese Phys. C* **34**, 421 (2010).

- [40] J. Z. Bai, Y. Ban, J. G. Bian, X. Cai, J. F. Chang, H. F. Chen, H. S. Chen, J. Chen, J. Chen, J. C. Chen, et al. (BES Collaboration), Phys. Rev. Lett. **91**, 022001 (2003).
- [41] B. Aubert, R. Barate, D. Boutigny, F. Couderc, Y. Karyotakis, J. P. Lees, V. Poireau, V. Tisserand, A. Zghiche, E. Grauges, et al. (BABAR Collaboration), Phys. Rev. D **72**, 051101 (2005).
- [42] B. Aubert, R. Barate, M. Bona, D. Boutigny, F. Couderc, Y. Karyotakis, J. P. Lees, V. Poireau, V. Tisserand, A. Zghiche, et al., Phys. Rev. D **74**, 051101 (2006).
- [43] K. Suzuki, M. Fujita, H. Geissel, H. Gilg, A. Gillitzer, R. S. Hayano, S. Hirezaki, K. Itahashi, M. Iwasaki, P. Kienle, et al., Phys. Rev. Lett. **92**, 072302 (2004).
- [44] R. Barth, P. Senger, W. Ahner, P. Beckerle, C. Bormann, D. Brill, M. Cieřlak, M. Dębowski, E. Grosse, P. Koczoń, et al. ((KaoS Collaboration)), Phys. Rev. Lett. **78**, 4007 (1997).
- [45] F. Laue, C. Sturm, I. Böttcher, M. Dębowski, A. Förster, E. Grosse, P. Koczoń, B. Kohlmeyer, M. Mang, L. Naumann, et al. ((KaoS Collaboration)), Phys. Rev. Lett. **82**, 1640 (1999).
- [46] D. Trnka, G. Anton, J. C. S. Bacelar, O. Bartholomy, D. Bayadilov, Y. A. Beloglazov, R. Bogendörfer, R. Castelijns, V. Crede, H. Dutz, et al. (CBELSA/TAPS Collaboration), Phys. Rev. Lett. **94**, 192303 (2005).
- [47] M. Danysz and J. Pniewski, Philosophical Magazine Series 7 **44**, 348 (1953).
- [48] M. Danysz, K. Garbowska, J. Pniewski, T. Pniewski, J. Zakrzewski, et al., Nucl.Phys. **49**, 121 (1963).
- [49] K. Szymanska, *Production of Double Hypernuclei with antiprotons at PANDA* (2008).
- [50] J. B. et al. (Particle Data Group), Phys. Rev. D **86** p. 010001 (2012).
- [51] V. Baier and V. A. Khoze, Sov.Phys.JETP **21**, 1145 (1965).
- [52] G. Bonneau and F. Martin, Nucl.Phys. **B27**, 381 (1971).
- [53] V. P. Druzhinin, S. I. Eidelman, S. I. Serednyakov, and E. P. Solodov, Rev. Mod. Phys. **83**, 1545 (2011).
- [54] W. Kluge, Nuclear Physics B - Proceedings Supplement **181-182**, 280 (2008).
- [55] B. Aubert et al. (BaBar Collaboration), Phys.Rev.Lett. **95**, 142001 (2005), hep-ex/0506081.

- [56] S. J. Brodsky, C. E. Carlson, J. R. Hiller, and D. S. Hwang, Phys.Rev. **D69**, 054022 (2004), [hep-ph/0310277](#).
- [57] R. Baldini, E. Pasqualucci, S. Dubnicka, P. Gauzzi, S. Pacetti, et al., eConf **C010430**, T20 (2001), [hep-ph/0106006](#).
- [58] F. Iachello, eConf **C0309101**, FRWP003 (2003), [nucl-th/0312074](#).
- [59] S. B. Athar, P. Avery, L. Brevina-Newell, R. Patel, V. Potlia, H. Stoeck, J. Yelton, P. Rubin, C. Cawfield, B. I. Eisenstein, et al. (CLEO Collaboration), Phys. Rev. D **73**, 032001 (2006).
- [60] M. Ablikim, J. Bai, Y. Ban, X. Cai, H. Chen, H. Chen, H. Chen, J. Chen, J. Chen, Y. Chen, et al., The European Physical Journal C **53**, 15 (2008), ISSN 1434-6044.
- [61] M. Ablikim, J. Z. Bai, Y. Ban, X. Cai, H. F. Chen, H. S. Chen, H. X. Chen, J. C. Chen, J. Chen, Y. B. Chen, et al. (BES Collaboration), Phys. Rev. Lett. **99**, 011802 (2007).
- [62] A. Sibirtsev, J. Haidenbauer, S. Krewald, U.-G. Meissner, and A. W. Thomas, Phys.Rev. **D71**, 054010 (2005), [hep-ph/0411386](#).
- [63] G. Chen, H. Dong, and J. Ma, Phys.Lett. **B692**, 136 (2010), 1004.5174.
- [64] X. Liu, X.-Q. Zeng, Y.-B. Ding, X.-Q. Li, H. Shen, et al. (2004), [hep-ph/0406118](#).
- [65] G.-J. Ding and M.-L. Yan, Phys.Rev. **C72**, 015208 (2005), [hep-ph/0502127](#).
- [66] G.-J. Ding, J.-l. Ping, and M.-L. Yan, Phys.Rev. **D74**, 014029 (2006), [hep-ph/0510013](#).
- [67] N. Kochelev and D.-P. Min, Phys.Lett. **B633**, 283 (2006), [hep-ph/0508288](#).
- [68] B. Aubert et al. (BaBar Collaboration), Phys.Rev. **D80**, 052002 (2009), 0905.4778.
- [69] R. Baldini and A. Zallo (ZDD Collaboration Meeting Giessen and Frascati), *ZDD at BESIII* (Dezember 2010).
- [70] M. Anelli, R. Baldini Ferroli, M. Bertani, A. Calcaterra, F. Cocchetti, et al., Nucl.Instrum.Meth. **A718**, 118 (2013).
- [71] V. Baier, V. S. Fadin, and V. A. Khoze, Sov.Phys.JETP **24**, 760 (1966).
- [72] *ZDD status report*, A. Calcaterra for the ZDD Group (BESIII Collaboration Meeting, June 2014).

- [73] V. Dormenev, T. Kuske, R. Novotny, A. Borisevich, A. Fedorov, M. Korjik, V. Mechinski, O. Missevitch, and S. Lugert, *Nuclear Instruments and Methods in Physics Research Section A: Accelerators, Spectrometers, Detectors and Associated Equipment* **623**, 1082 (2010), ISSN 0168-9002, URL <http://www.sciencedirect.com/science/article/pii/S0168900210018747>.
- [74] D. Renker, *Nucl.Instrum.Meth.* **A567**, 48 (2006).
- [75] Z. Sadygov, *Patent No. RU 2102820* (1998).
- [76] Hamamatsu, *MPPC, MPPC modules - Technical Information* (2013), URL http://www.hamamatsu.com/resources/pdf/ssd/mppc_techinfo_e.pdf.
- [77] N. Otte, eConf **C0604032**, 0018 (2006).
- [78] SPAD lab, *Crosstalk in SPAD devices* (2014), URL <http://www.everyphotoncounts.com/device-crosstalk.php>.
- [79] B. Dolgoshein, *Talk given at Light06-Large-Area Photon Detectors Workshop* (2006).
- [80] Hamamatsu, *MPPC (multi-pixel photon Counter), S10931 series datasheet* (2014), URL <http://www.electronicdatasheets.com/download/114923.pdf?format=pdf&part=Hamamatsu+-+S10931-050P>.
- [81] W. Leo, *Techniques for Nuclear and Particle Physics Experiments* (Springer Verlag, 1994).
- [82] K. Olive et al. (Particle Data Group), *Chin.Phys.* **C38**, 090001 (2014).
- [83] Y.-J. M. Wei-Dong and Y.-F. Wang, *Int. J. Mod. Phys.* **A24**, 9 (2009).
- [84] G. Barrand, I. Belyaev, P. Binko, M. Cattaneo, R. Chytracsek, et al., *Comput.Phys.Commun.* **140**, 45 (2001).
- [85] S. Agostinelli et al. (GEANT4), *Nucl.Instrum.Meth.* **A506**, 250 (2003).
- [86] J. Nam et al. (Belle Collaboration), *Nucl.Instrum.Meth.* **A491**, 54 (2002), [hep-ex/0204030](http://arxiv.org/abs/hep-ex/0204030).
- [87] P. Website (2015), URL <http://ific.uv.es/~rodrigo/phokhara/>.
- [88] G. Akopdzhanov, A. Inyakin, V. Kachanov, R. Krasnokutsky, A. Lednev, et al., *Nucl.Instrum.Meth.* **140**, 441 (1977).
- [89] T. Awes, F. Obenshain, F. Plasil, S. Saini, S. Sorensen, et al., *Nucl.Instrum.Meth.* **A311**, 130 (1992).

- [90] D. A. Bremer, *Measurements and Simulations on Position Dependencies in the Response of Single PWO Crystals and a Prototype for the PANDA EMC* (Ph.D. Thesis, II. Physikalisches Institut, JLU Gießen, 2013).
- [91] C. Adloff et al. (CALICE), *JINST* **9**, P01004 (2014), 1311.3505.
- [92] M. Kavatsyuk et al. (PANDA), *IEEE NSS/MIC* pp. 43–47 (2011).
- [93] P. Marciniewski (Uppsala university), *Private communication* (2012).
- [94] Xilinx, *Logicore ip aurora 8b/10b v5.3*, URL http://www.xilinx.com/support/documentation/ip_documentation/aurora_8b10b/v5_3/aurora_8b10b_ds637.pdf.
- [95] T. Uchida, *IEEE Trans.Nucl.Sci* **55**, 1631 (2008).
- [96] R.-Y. Zhu, *Status of LSO/LYSO Crystals for HEP Experiments* (March 2010), URL http://www.hep.caltech.edu/~zhu/talks/ryz_100318_SLHC.pdf.
- [97] Institute for Nuclear Physics, Mainz, *Website*, URL <http://www.kph.uni-mainz.de/mami.php>.
- [98] P. Schakel (KVI Groningen), *Private communication* (2012 - 2014).
- [99] Hamamatsu, *MPPC (multi-pixel photon Counter), S12572 series datasheet* (2015), URL http://www.hamamatsu.com/resources/pdf/ssd/s12572-025_etc_kapd1043e.pdf.

DANKSAGUNGEN

Gelobt sei der Herr täglich.
Gott legt uns eine Last auf,
aber er hilft uns auch.

Psalm 68, 20

Vor allem anderen möchte ich meinen Dank an Gott aussprechen - Deine Liebe trägt mich und hat mir in dieser intensiven Zeit jeden Tag Halt und Kraft gegeben.

Eine wissenschaftliche Arbeit ist nur möglich mit der Unterstützung vieler Menschen, von denen ich jedem Einzelnen dankbar bin.

Zunächst möchte ich Prof. Dr. Wolfgang Kühn für die Möglichkeit danken in seiner Arbeitsgruppe promovieren zu können.

Besonderer Dank gebührt Priv.-Doz. Dr. Sören Lange und Dr. Yutie Liang, die durch ihr Fachwissen und ihre Hilfsbereitschaft zum Gelingen dieser Arbeit beigetragen haben.

Mein Dank gilt auch Prof. Dr. Concettina Sfienti und Sebastian Baunack vom Mainzer Institut für Kernphysik, die es ermöglichten einen sehr kurzfristigen Termin für meinen Beamtest am MAMI zu bekommen.

Nicht unerwähnt lassen möchte ich Peter Schakel (KVI Groningen) und Dr. Pawel Marciniewski (University of Uppsala), die mir bei meinen vielen Fragen zur sADC Firmwareentwicklung weitergeholfen haben.

Ohne Thomas Gessler würde ich noch heute über dem VHDL-Buch und der Xilinx-Software verzweifeln - DANKE, für deine unermüdliche Hilfe beim Einarbeiten in VHDL und bei der Firmwareentwicklung für den CN. Vielen Dank auch dafür, dass Du mir zusammen mit Milan Wagner eine große Hilfe bei dem Beamtest am MAMI warst.

Dankbar bin ich auch für die Zeit mit meinen Bürokollegen Dr. Matthias Ullrich und Svende Braun - DANKE für eure Freundschaft und die oft witzigen Unterhaltungen, aber auch für die vielen tiefgründigen Gespräche, die wir führen konnten.

Auch dem Rest der Arbeitsgruppe gebührt Dank: Christa und Thomas K. (DANKE für alle administrativen und technischen Aufgaben, die ihr für uns erledigt), Björn, David, Klemens, Martin, Sören F., Simon, Dennis und Christopher.

Die Zusammenarbeit mit Ulrich Thöring und Marcel Straube bei der Entwicklung des MPPC Koinzidenz Boards hat mir viel Spaß gemacht - vielen Dank für eure Geduld mit mir, wenn ich mal wieder etwas nicht richtig verstanden habe.

Außerdem möchte ich Dr. Rainer Novotny, Rene Schubert und Stefan Diehl danken, die stets ein offenes Ohr für meine technischen Probleme hatten und mir mit fachkundigem Rat zur Seite standen.

Es hat mir gut getan mich mit Freunden unterhalten zu können, die sich in einer ähnlichen Situation wie ich befinden - DANKE Gunna Lampe und Walter Heupel für die aufbauenden Gespräche und die gegenseitigen Durchhalteparolen.

Meinem Freund und ehemaligen Mathematik- und Physiklehrer Gebhard Häußer gilt ein besonderer Dank - Du hast mich für Mathematik und Physik begeistert und mir einen authentischen und lebendigen Glauben vorgelebt - und bist wahrscheinlich der Mensch, der mich nach meinen Eltern am meisten geprägt hat.

Meinem Bruder Julian Werner möchte ich für das sorgfältige Korrekturlesen meiner Arbeit danken - DANKE, dass Du dich durch so viele Seiten unverständlichen Inhalts durchgekämpft hast!

Ganz besonderer Dank gilt meinen Eltern, die mich immer unterstützt und an mich geglaubt haben - DANKE für eure Liebe und dass ihr mir meine Ausbildung ermöglicht habt.

Nicht zuletzt danke ich meiner Frau Stefanie und meinem Sohn Lukas - ihr hattet es in den vergangenen Jahren oft nicht leicht mit mir und ohne eure ausdauernde Unterstützung hätte ich es nicht schaffen können, aber gemeinsam haben wir diesen Lebensabschnitt gemeistert! An jedem einzelnen Tag habe ich mich darauf gefreut, euch am Abend wieder in meine Arme schließen zu können!

EIDESSTATTLICHE VERSICHERUNG

Ich erkläre: Ich habe die vorgelegte Dissertation selbstständig und ohne unerlaubte fremde Hilfe und nur mit den Hilfen angefertigt, die ich in der Dissertation angegeben habe. Alle Textstellen, die wörtlich oder sinngemäß aus veröffentlichten Schriften entnommen sind, und alle Angaben die auf mündlichen Auskünften beruhen, sind als solche kenntlich gemacht. Bei den von mir durchgeführten und in der Dissertation erwähnten Untersuchungen habe ich die Grundsätze guter wissenschaftlicher Praxis, wie sie in der *“Satzung der Justus-Liebig-Universität zur Sicherung guter wissenschaftlicher Praxis”* niedergelegt sind, eingehalten.

Gießen, den 18. Mai 2015

Marcel Werner